

AD-A245 940



② *ur*

# NAVAL POSTGRADUATE SCHOOL

## Monterey, California



**DTIC**  
**ELECTE**  
**S D D**  
**FEB 14 1992**

## THESIS

FLOW VISUALIZATION STUDIES OF  
A SIDESLIPPING, CANARD-CONFIGURED  
X-31A-LIKE FIGHTER AIRCRAFT MODEL

by

KIM, CHANG HO

December 1991

Thesis Advisor:  
Co-Advisor:

S. K. Hebbar  
M.F. Platzer

Approved for public release; distribution is unlimited

92-03542



92 2 10 021

UNCLASSIFIED

SECURITY CLASSIFICATION OF THIS PAGE

REPORT DOCUMENTATION PAGE				
1a. REPORT SECURITY CLASSIFICATION Unclassified			1b. RESTRICTIVE MARKINGS	
2a. SECURITY CLASSIFICATION AUTHORITY			3. DISTRIBUTION/AVAILABILITY OF REPORT Approved for public release; distribution is unlimited.	
2b. DECLASSIFICATION/DOWNGRADING SCHEDULE				
4. PERFORMING ORGANIZATION REPORT NUMBER(S)			5. MONITORING ORGANIZATION REPORT NUMBER(S)	
6a. NAME OF PERFORMING ORGANIZATION Naval Postgraduate School		6b. OFFICE SYMBOL (If applicable) AA	7a. NAME OF MONITORING ORGANIZATION Naval Postgraduate School	
6c. ADDRESS (City, State, and ZIP Code) Monterey, CA 93943-5000			7b. ADDRESS (City, State, and ZIP Code) Monterey, CA 93943-5000	
8a. NAME OF FUNDING/SPONSORING ORGANIZATION		8b. OFFICE SYMBOL (If applicable)	9. PROCUREMENT INSTRUMENT IDENTIFICATION NUMBER	
8c. ADDRESS (City, State, and ZIP Code)			10. SOURCE OF FUNDING NUMBERS	
			Program Element No	Project No
			Task No	Work Unit Accession Number
11. TITLE (Include Security Classification) Flow Visualization Studies of a Sideslipping, Canard-Configured X-31A-Like Fighter Aircraft Model, (Unclassified)				
12. PERSONAL AUTHOR(S) Kim, Chang Ho				
13a. TYPE OF REPORT Master's Thesis		13b. TIME COVERED From To		14. DATE OF REPORT (year, month, day) December 1991
15. PAGE COUNT 125				
16. SUPPLEMENTARY NOTATION The views expressed in this thesis are those of the author and do not reflect the official policy or position of the Department of Defense or the U.S. Government.				
17. COSATI CODES			18. SUBJECT TERMS (continue on reverse if necessary and identify by block number)	
FIELD	GROUP	SUBGROUP		
			High angle of attack aerodynamics, effect of static AOA, sideslip (yaw) and sideslipping motion, vortex development and bursting, flow visualization by dye injection, water tunnel studies, X-31A fighter aircraft	
19. ABSTRACT (continue on reverse if necessary and identify by block number)				
<p>A water tunnel flow visualization investigation was performed to study the vortex development and bursting phenomena on a 2.3% scale model of a X-31A-Like fighter aircraft. The main focus of this study was two-fold: First, to study the effects of angle of attack and static sideslip on the model vortical flow field. Secondly, to study the effects of dynamic sideslip motion at two reduced yaw rates. Results indicate that the wing root vortex bursting locations move upstream as the AOA increases; and at constant angle of attack (AOA &lt; 30 degrees) the leeward side vortex bursting location moves backward and outboard with sideslip inputs while the windward side vortex bursting location moves forward and inboard. The vortex asymmetry switches sides at higher angle of attack (AOA &gt; 30 degrees). The dynamic lag effects, which cause the leeward side vortex to burst earlier than in the static case during the positive sideslipping motion and later than in the static case during the negative sideslipping motion, increase with the magnitude of the sideslipping motion.</p>				
20. DISTRIBUTION/AVAILABILITY OF ABSTRACT <input checked="" type="checkbox"/> UNCLASSIFIED/UNLIMITED <input type="checkbox"/> SAME AS REPORT <input type="checkbox"/> DTIC USERS			21. ABSTRACT SECURITY CLASSIFICATION Unclassified	
22a. NAME OF RESPONSIBLE INDIVIDUAL S.K. Hebbar			22b. TELEPHONE (Include Area code) (408) 646-2997	22c. OFFICE SYMBOL AA/Hb

DD FORM 1473, 84 MAR

83 APR edition may be used until exhausted  
All other editions are obsoleteSECURITY CLASSIFICATION OF THIS PAGE  
UNCLASSIFIED

Approved for public release; distribution is unlimited.

Flow Visualization Studies of a Sideslipping,  
Canard-Configured X-31A-Like Fighter Aircraft Model

by

Kim, Chang Ho  
Major, ROK Air Force  
B.S., ROK Air Force Academy, 1982

Submitted in partial fulfillment  
of the requirements for the degree of

MASTER OF SCIENCE IN ENGINEERING SCIENCE (AERONAUTICS)

from the

NAVAL POSTGRADUATE SCHOOL

December, 1991

Author:

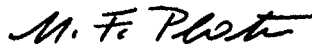


Kim, Chang Ho

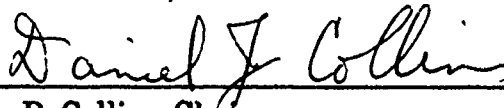
Approved by:



S.K. Hebbar, Thesis Advisor



M.F. Platzter, Co-Advisor



D. Collins, Chairman

Department of Aeronautics and Astronautics

## ABSTRACT

A water tunnel flow visualization investigation was performed to study the vortex development and bursting phenomena on a 2.3 % scale model of a X-31A-Like fighter aircraft. The main focus of this study was two-fold : First, to study the effects of angle of attack and static sideslip on the model vortical flow field. Secondly, to study the effects of dynamic sideslip motion at two reduced yaw rates. Results indicate that the wing root vortex bursting locations move upstream as the AOA increases; and at constant angle of attack ( $AOA < 30^\circ$ ) the leeward side vortex bursting location moves backward and outboard with sideslip inputs while the windward side vortex bursting location moves forward and inboard. The vortex asymmetry switches sides at higher angles of attack ( $AOA > 30^\circ$ ). The dynamic lag effects, which cause the leeward side vortex to burst earlier than in the static case during the positive sideslipping motion and later than in the static case during the negative sideslipping motion, increase with the magnitude of the sideslipping motion.

Accession For	
NTIS CRA&I	<input checked="" type="checkbox"/>
DTIC TAB	
Unannounced	
Justification _____	
By _____	
Distribution /	
Availability Codes	
Dist	Avail and/or Special
A-1	



## TABLE OF CONTENTS

I.	INTRODUCTION .....	1
II.	EXPERIMENTAL APPARATUS .....	5
A.	WATER TUNNEL .....	5
B.	X-31A-LIKE MODEL .....	8
C.	MODEL MOUNTING .....	10
III.	EXPERIMENTAL PROCEDURE .....	13
A.	EXPERIMENTS .....	13
B.	REDUCED YAW RATE SIMULATION .....	14
C.	DATA ACQUISITION .....	15
D.	DATA REDUCTION .....	16
E.	METHOD OF PHOTOGRAPHY .....	17
IV.	RESULTS AND DISCUSSION .....	19
A.	EFFECTS OF AOA ON THE WING FLOW FIELD OF X-31A MODEL .....	20
B.	STATIC SIDESLIP EFFECTS .....	21
C.	DYNAMIC SIDESLIP EFFECTS .....	23
1.	Sideslip-Increase Motion (Positive Sideslipping) .....	23
2.	Sideslip-Decrease Motion (Negative Sideslipping) .....	25

D.	BURSTING LOCATION PLOTS .....	28
V.	CONCLUSIONS AND RECOMMENDATIONS .....	31
	LIST OF REFERENCES .....	33
APPENDIX A.	EXPERIMENTAL RESULTS (PHOTOGRAPHS) .....	35
APPENDIX B.	EXPERIMENTAL RESULTS (GRAPHS) .....	101
APPENDIX C.	EXPERIMENTAL RESULTS (TABLES) .....	109
APPENDIX D.	MISCELLANEOUS DATA .....	113
	INITIAL DISTRIBUTION LIST .....	117

## **ACKNOWLEDGEMENT**

This thesis was sponsored by the Naval Air Systems Command, the Naval Postgraduate School, and the Naval Air Development Center.

First of all, I would like to thank God for all the love, grace and strength throughout my life, especially the last 3 years.

I would like to express my sincere appreciation to my thesis advisor, Professor S.K. Hebbbar, and co-advisor Professor M.F. Platzer, for their guidance, encouragement and patience throughout the course of this project.

I would like to thank the ROKAF for providing the opportunity to study at NPS.

I would also like to thank the many people at NPS who provided the services and expertise necessary for this research. In particular:

Mr. Al McGuire, Aeronautics Lab

Mr. Mitch Nichols, Photo Lab

Mr. John Molten, Aeronautics Metal Shop

Mr. Jack King, Aeronautics Lab

Finally, I would like to take this opportunity to express my deepest gratitude to my wife Sun-Rei and daughter, Seung-Hyun for their self sacrifice and encouragement in support of my efforts.

## I. INTRODUCTION

When fighter pilots describe the aircraft that served them well in combat, they use terms such as nimble, spry, light on the controls, to refer to aircraft ability to change directions quickly. Engineers need to know what aerodynamic configurations have these attributes so that they can design and test for them. And once the relationships between performance parameters and mission objectives are nailed down, military planners can set requirements for agility that designers can meet. [Ref.1]

In 1977, Messerschmitt Boelkow Blohm (MEB) started examining how aerial combat is affected by the ability to point and turn rapidly at low speeds. A key technological change driving these studies was the emergence of improved short range heat-seeking missiles that could lock on to the forward aspect of a target, and not just the hot rear view of the engine. All-aspect weaponry meant that tail-chase tactics no longer had to dominate short-range combat. Instead, just pointing at the adversary is sufficient, and this is greatly helped by being able to maintain control well beyond the angle of attack (AOA) for maximum lift.

Wolfgang Herbst and Karl Knauer of MBB concluded that better agility at low speeds and good supersonic maneuverability at medium to high altitudes would help both short- and medium-range encounters. They concluded that a delta wing/canard configuration would be equal to other designs at low speeds and give better supersonic performance. This configuration was adopted for the X-31A. [Ref.2]



The X-31A is an experimental aircraft developed under a joint program between Rockwell International Cooperation and MBB to determine the technical requirements for future tactical aircraft. The X-31A was designed to operate at AOA up to 70 degrees while retaining full control. Note that the configuration is not a highly optimized wing/canard configuration. Due to the lightly loaded canard, the X-31A can be best considered a delta wing with a recovery control surface. [Ref.3] Figure 1 shows the geometry of the X-31A.

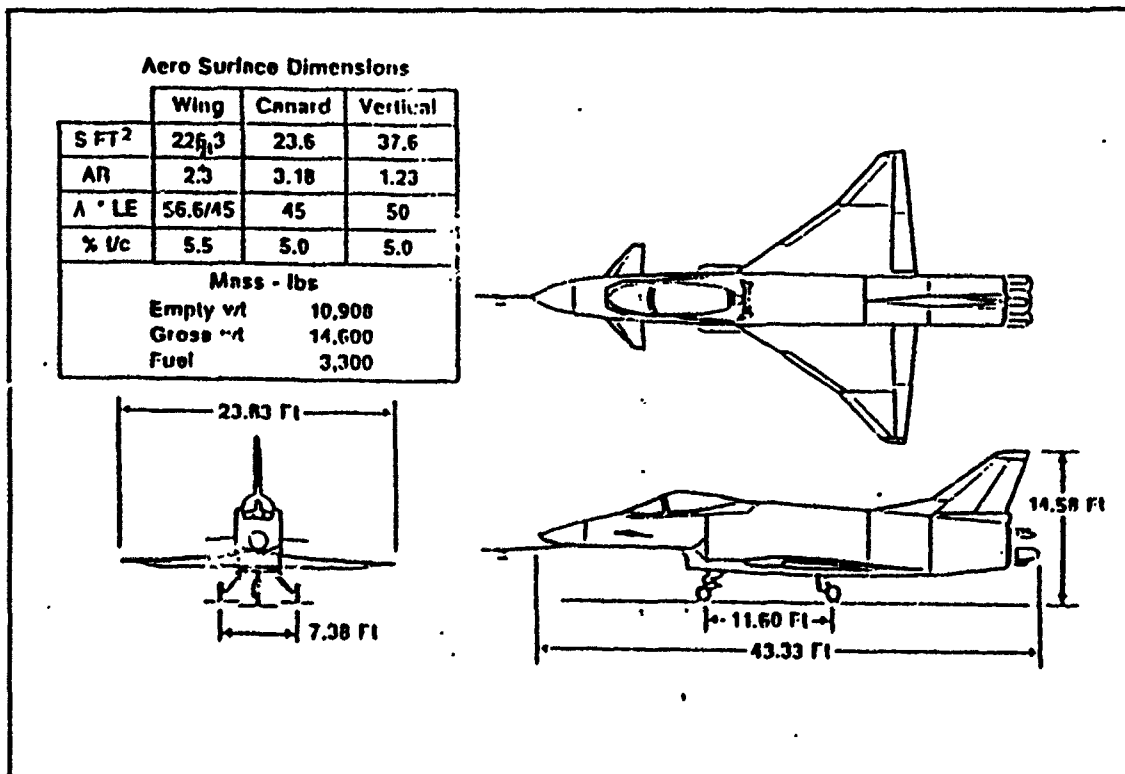


**Figure 1. X-31A Configuration**

The use of canard configurations as a potential method for improved aerodynamic performance has received considerable attention in recent years, both experimentally and

computationally. The combination of a delta wing with a properly designed and integrated close-coupled canard improves maximum lift with less penalties of canard wing interaction. At the same time, a canard can be used as a control device for optimum lift to drag ratio throughout the fighter envelope. [Ref.4]

As pointed out in [Ref.5], the flow physics of the canard-wing configuration is still insufficiently understood and documented. Of special significance is the understanding of the vortex development under rapid maneuvering conditions as envisioned for the X-31A aircraft. The recent investigation [Refs.6 and 7] carried out at the Naval Postgraduate School (NPS) as part of the enhanced fighter maneuverability research program was the first of its kind undertaken to characterize the flow field around a pitching canard-configured fighter aircraft model comparable to the X-31A.

The flow field about highly swept wings, including delta wings, at moderate to high AOA is characterized by the leading-edge vortices. These vortices contribute to the lift by generating low pressure regions over the wing suction side. This contribution is disrupted when vortex breakdown occurs and the vortex breakdown stagnation point crosses the wing trailing edge and moves upstream toward the wing apex as the AOA is increased. [Ref.8]

Vortex bursting (breakdown of the stable, spiral structure) is due to the instability from the core outward. When bursting is symmetric, only pitch stability is affected, i.e., as the bursting location moves toward the apex, the distribution of the lift is such that a pitch-up results. If bursting is asymmetric, a rolling moment will also result, adversely affecting both roll and yaw stability. [Ref.9]

At zero sideslip, the leading edge vortices are of equal strength and size, yielding a symmetric crossflow pattern and wing surface pressure distribution. Detailed experimental data on this type of symmetric vortex flow is available from many investigations carried out on slender delta wings or strake-wing configurations. [Refs.10 to 13]

Yaw effects can be important for the stability and control of aircraft at high AOA flight conditions occurring during takeoff, landing, and maneuvering. However, experimental data available on the influence of sideslip on the flow characteristics of delta wings is very limited.[Ref.14] The data on yaw rate effects is even scarcer.

The objective of this thesis, therefore, is to study the influence of sideslip on a X-31A-like model in both static and dynamic conditions. Specifically, the wing root vortex breakdown characteristics are investigated in the NPS water tunnel using dye injection flow visualization technique.

## II. EXPERIMENTAL APPARATUS

### A. WATER TUNNEL

The experiments were performed in the Naval Postgraduate School flow visualization water tunnel facility which was designed by Eidetics International, Inc, California and installed in late 1988 [Refs.15 and 16]. Figure 2 shows the layout of the water tunnel.

The NPS water tunnel is a closed circuit facility suitable for studying a wide range of aerodynamic and fluid dynamic phenomena. Its key design features are high flow quality,

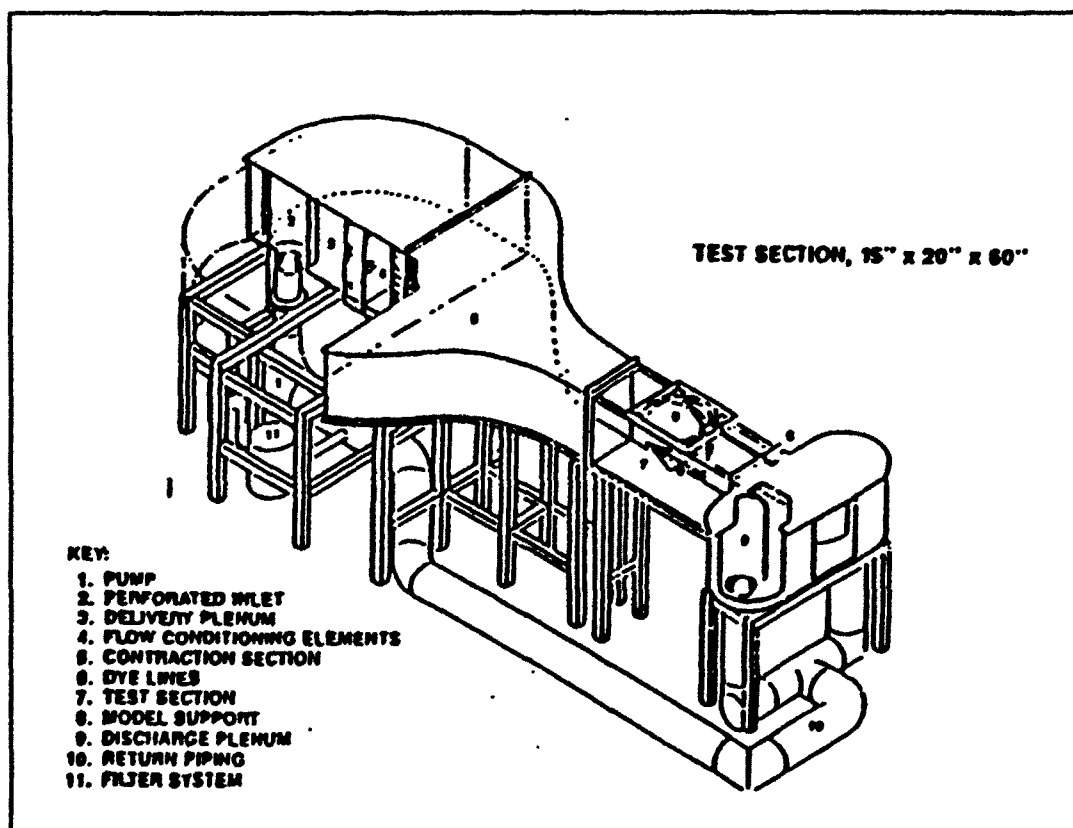


Figure 2. Water Tunnel Facility at NPS

horizontal orientation and continuous operation. The horizontal orientation facilitates access, and enables models to be readily changed without draining the water from the tunnel. The rate of circulation of water is up to 900 gallons/minute to provide up to 1 foot/sec flow rate in the test section.

The test section was nominally 15 inches wide, 20 inches high, and 60 inches long. The sidewalls of the test section have a slight divergence to compensate for boundary layer growth and to maintain uniform flow velocity throughout. It was constructed primarily of tempered glass to provide thermal stability, scratch resistance and maximum viewing of the model. Furthermore, the glass test section and the discharge plenum allowed simultaneous viewing of the model from the bottom, both sides and from the rear. The level of flow quality (measured outside the boundary layer) over the test section velocities was as follows:

Mean flow angularity :  $< \pm 1.0^\circ$  in both pitch and yaw angle

Turbulence intensity level :  $< 1.0\%$  RMS

Velocity uniformity :  $< \pm 2.0\%$

Six pressurized dye canisters using water-soluble food coloring were used for flow visualization. Each canister was pressurized with air by a small compressor and connected to the model port through an individually routed line. The value of a pressurized system was a finer control to regulate the dye emission and to provide a means of blowing air out of the dye lines going to the model.

The model support system mounted on the top of the test section utilized a C-strut to change the pitch angle and a turntable to change the yaw angle. Fig.3 illustrates the model support system.

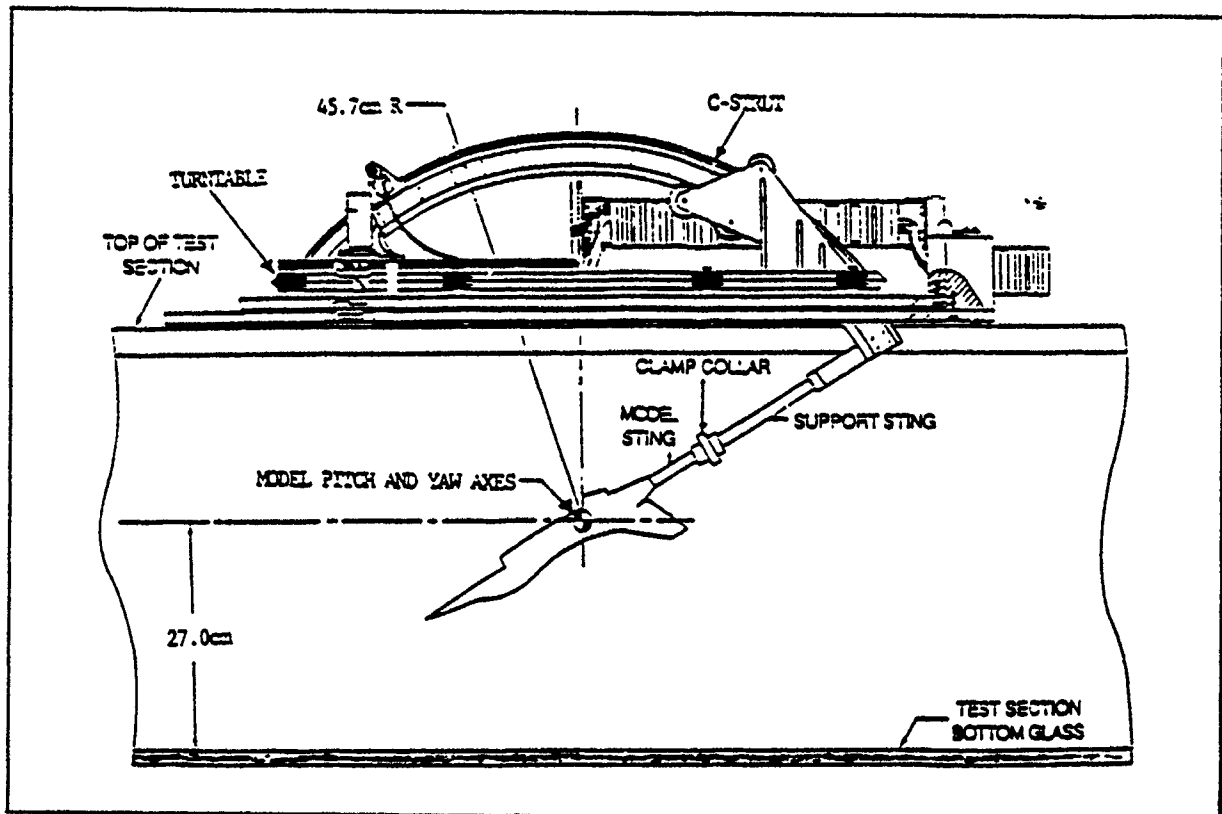


Figure 3. Model Support System of the NPS Water Tunnel

The model was usually mounted with a sting and upside down in the test section. Two remotely driven motors were used for varying the model attitude (pitch and yaw). Each motor had a high/low rate switch and could be controlled by a remote control to investigate the dynamic motion of the model. The high yaw rate and low yaw rate corresponded to 2.8 deg./sec and 1.8 deg./sec, respectively. More details about the water tunnel facility may be found in [Ref.17].

## **B. X-31A-LIKE MODEL**

A 2.3 % scale model of X-31A fighter aircraft was used in this investigation. Figure 4 shows the configuration of the X-31A-like model. The difference between the model and the actual X-31A was not severe. The model did not have a canopy and a vertical tail, but had a double-delta wing and a delta-canard like the X-31A. The modular construction of the fuselage allowed for easy variations in the horizontal and vertical locations of the canard with respect to the main wing. Previous studies have indicated that a close-coupled canard configuration results in a more favorable aerodynamic interference between the vortex systems of the canard and the wing; and a high canard location (unlike a low canard/coplanar-location relative to the wing) influences the wing flow field favorably. The location of the canard selected for the current investigation closely approximated these conditions. The horizontal and vertical distances of the quarter-chord point of the canard root chord from the quarter-chord point of the wing root chord were 43.18 % and 7.95 % of the wing root chord, respectively. The upper surface of the wing and the fuselage had grid lines measured at every quarter inch for easy identification of vortex burst locations. The key dimensions of the model are listed below:

1. Total length = 12.0 in.
2. Span (wing, canard) = 8.0 in., 2.0 in.
3. Wing chord = 5.5 in.(root), 2.64 in.(mid), 0.75 in.(tip)
4. Sweep angle (wing, canard) = 58°/46°, 30°
5. Wing mean aerodynamic chord = 3.369 in.

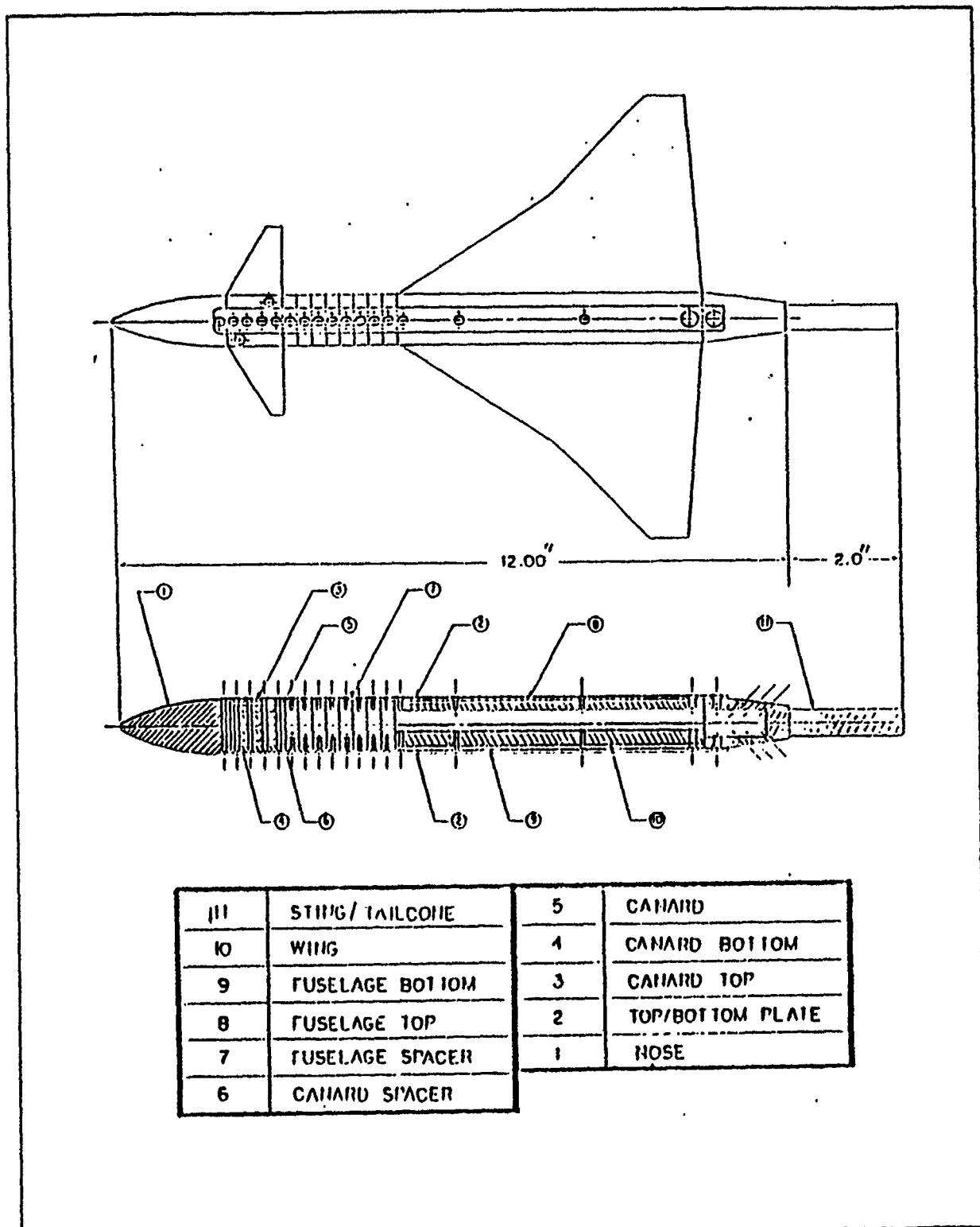


Figure 4. X-31A-Like Model Configuration



6. Wing area =  $19.866 \text{ in}^2$ .
7. Canard chord = 1.0 in.(root), 0.25 in.(tip)
8. Canard area =  $1.563 \text{ in}^2$ .
9. Area ratio (canard/wing) = 7.87 %
10. Canard setting angle =  $2^\circ$

Table 1 (Appendix D) shows the geometric coordinates of the canard and the wing. Fig.5 shows the dye-port locations on the X-31A-like model. The canard had four dye-injection ports and the wing had six. As the main focus of this investigation was the development and bursting of the vortices shed from the root of the wing, only canard tip and wing root dye ports were used.

### C. MODEL MOUNTING

It was very important to insure that the model was mounted horizontally in the water tunnel with zero pitch, zero yaw, and zero roll. The installation of the model in the test section was accomplished in the following way. [Ref.6] First, the model with an extension bar was attached to the sting holder on the model support base by using a small hexagonal head screw. The model was introduced into the water surface by lowering the model support base to its horizontal position and the model horizontality was checked visually by the timing and the degree of wetting on both wing surfaces. The centerline of the model (fuselage) was then aligned with the freestream (tunnel center line) by using spacers as

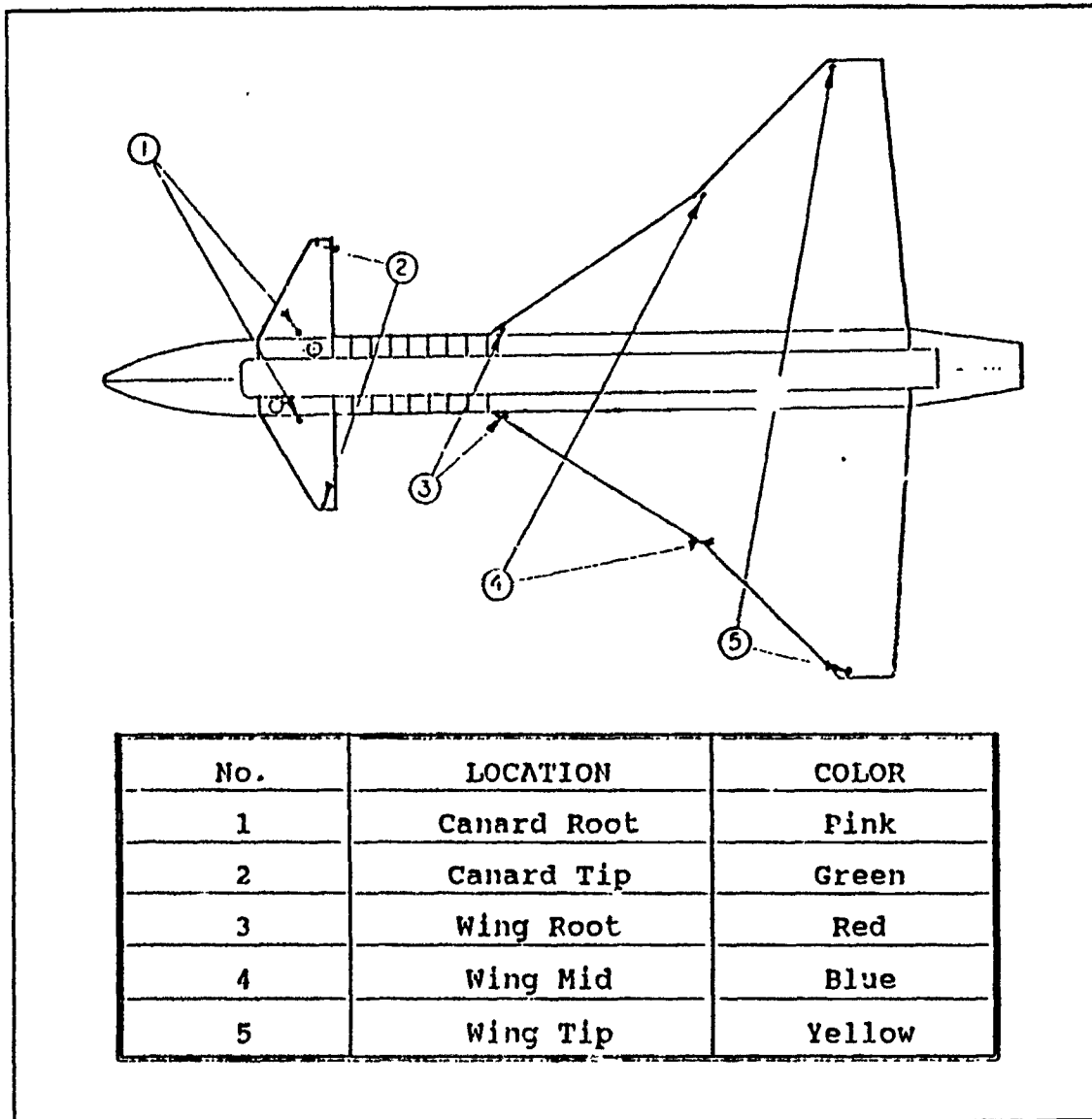


Figure 5. Dye-Port Location on the X-31A-Like Model

needed between the model support base and the top of the test section frame. The pitch angle was calibrated by choosing a reference line on the model (fuselage center line).

The zero yaw angle was checked by setting the model nose equidistant from either side wall of the test section and by observing symmetric dye lines from both wing surfaces

at zero pitch angle. The yaw angle was calibrated by choosing a reference line on the model (fuselage center line). Finally, zero roll angle was checked by locating the left and right wing tips at the same height from the bottom of the test section. The axes of rotation for both pitch and yaw motions were located at 8.45 inches aft of the nose.

### III. EXPERIMENTAL PROCEDURE

#### A. EXPERIMENTS

The goal of this investigation was to study the influence of sideslip, in both static and dynamic conditions, on the development and bursting of vortices shed from the wing root of the X-31A-like model. The experiments consisted of flow visualization of the X-31A-like model for static conditions and for two yaw rates, with sideslip angle ( $\beta$ ) varying from  $0^\circ$  to  $20^\circ$  (simple sideslip increase) and  $20^\circ$  to  $0^\circ$  (simple sideslip decrease). The angle of attack ( $\alpha$ ) was varied from  $15^\circ$  to  $50^\circ$  at intervals of  $5^\circ$ . Note that for angles of attack less than  $15^\circ$ , the vortex structure is not well defined.[Ref. 6] Table 2 illustrates the different test conditions.

Table 2. WING ROOT VORTEX FLOW VISUALIZATION

YAW(degree)	CONDITIONS	YAW RATE	AOA(degree)	REMARKS
$0^\circ$ to $20^\circ$  at $5^\circ$  increments	Static	- - -	$15^\circ, 20^\circ, 25^\circ,$  $30^\circ, 35^\circ, 40^\circ,$  $45^\circ, 50^\circ$	Side view, Top view,
	Dynamic	Low yaw rate increase		Still picture,  Video tape recording
		Low yaw rate decrease		
		High yaw rate increase		
		High yaw rate decrease		

Both still-picture photography and videotape recording were used for documentation of the flow visualization of the model. The flow velocity in the test section was kept nearly constant at 0.25 ft/sec which corresponds to a nominal Reynolds number of 22,500 per foot or 10,200 based on the wing root chord of the model. Studies by other researchers have indicated that the water tunnel data on bursting locations of vortices shed off sharp leading edges compare very favorably with the data from flight and ground tests in spite of very low Reynolds number in the water tunnel. [Refs.15, 16, 18 and 19]

## **B. REDUCED YAW RATE SIMULATION**

In the low Reynolds number aerodynamics, all investigations and design methods have been based on steady state flow conditions. However, aircraft encounter unsteadiness under all flight conditions whether due to inputs of dynamic motion (i.e., pitch-up/down, yaw-increase/decrease), or of natural disturbances (i.e., wind shear, gusts). Therefore to understand the stability of an aircraft operating in these conditions, a knowledge of its response to flow unsteadiness is essential.

The guiding non-dimensional parameter during yawing motions is the reduced yaw rate,  $k$ , given by the following formula:

$$k = \frac{\dot{\beta} b}{2U_{\infty}}$$

where,

$k$  : reduced yaw rate, non-dimensional

$\dot{\beta}$  : yaw rate, rad/sec

$b$  : characteristic span of the model, ft

$U_{\infty}$  : free stream velocity, ft/sec

For a yawing wing, the reduced yaw rate represents non-dimensional yaw rate. In the case of a wing yawing about its geometric center, the reduced yaw rate may be interpreted as the ratio of the lateral motion of the leading edge to its longitudinal motion.

Using this formula the reduced yaw rate for the full scale X-31A aircraft was calculated and compared with the values for the water tunnel model. Table 3 lists these values and indicates that the water tunnel facility is capable of simulating the full scale value of the reduced yaw rate for the X-31A aircraft.

Table 3. REDUCED YAW RATE

Yaw Rate *	$\dot{\beta}$ (rad/sec)	Span (ft)	$U_{\infty}$ (ft/sec)	$K$ (Reduced Yaw rate)
Low Yaw Rate	0.032	0.75	0.25	0.05
High Yaw Rate	0.051	0.75	0.25	0.08
Full Scale X-31A aircraft	0.700	22.83	253	0.03

\* The model yaw-axis was located at 8.45 inches aft of the nose.

### C. DATA ACQUISITION

This was accomplished using two 35 mm automatic cameras. The data collection consisted of taking photographs providing a simultaneous sideview (leeward side, and topview of the vortical flow field originating off the wing root port of the X-31A-like model.

A video camera was also used to record the flow phenomena for static and dynamic conditions. It should be noted here that a good deal of direct visual analysis of the flow field preceded the actual data collection phase. The lighting and camera settings are described in section E.

#### **D. DATA REDUCTION**

Data reduction essentially consisted of measuring the bursting location of the vortex shed off the wing root port and plotting it as a function of angle of attack at different yaw rates. When a yaw is imposed on an aircraft the side opposite the yaw input is called the windward side, and the side in the same direction as the yaw input is called the leeward side. For this investigation all measurements were made on the leeward side of the X-31A model using the leading edge of the wing root chord as the reference point. The vortex bursting locations for the static case were visually determined from the photographs. For the dynamic case the vortex bursting locations were first observed visually by naked eye, then checked during the playback of the videotape and finally determined from the photographs. The measurements of the vortex bursting locations were made with utmost care and consistency, and scaled for non-dimensionalization using the wing root chord. Some degree of imprecision may be still present in the reduced data due to the difficulty in determining the vortex bursting location particularly at high angle of attack and at high yaw rate. It should be pointed out here that during the static segment of the experiment, the vortex bursting location at any model attitude was found to fluctuate up to  $\pm 0.25$  inches. The bursting locations are listed in Tables 4-8 (Appendix C).

## **E. METHOD OF PHOTOGRAPHY**

The equipment used for the photographic session consisted of two 35 mm automatic cameras, 4 Smith-Victor 600 watts photographic lights, and a fixed flood light installed below the test section. For the sideview photographs two of the lights were placed at a distance of three feet at a 45 degrees angle from the test section. Another photographic light was placed below the test section at 45 degrees angle near the front of the model. The last one was placed below the test section at 45 degrees angle near the rear of the model.

Figure 6 illustrates the lighting setup for both the sideview and topview photographs. The same lighting arrangement was used for videotaping of the vortical flow field on the model.

A Minolta 5000i camera with depth card and all the automatic functions of focusing, shutter speed control, aperture control and ASA setting was used for taking topview pictures. A Nikon 2050 camera with features similar to Minolta 5000i camera (except automatic ASA setting) was used for taking sideview pictures. The two automatic cameras were very effective for both sideview and topview pictures, in particular during the dynamic case, because the focusing was automatically adjusted as the yaw angle was changed. The type of film used for all the photographs was 35 mm black and white ASA 400 film. During the exposure of the film, the topview camera (Minolta 5000i) was set to auto ASA, auto aperture, auto shutter speed, and auto focus. The sideview camera (Nikon 2050) was loaded manually to ASA 400 and set to auto aperture, auto shutter speed, and auto focus on the leeward side of the model. The sideview camera was adjusted so that the center of the





Figure 6. Camera and Lighting Setup for Photographs

camera focus was aligned with the model's pitch rotation axis, and the camera body was slightly pitched up to have the model always at the center of the picture regardless of changing yaw angle.

A clear plastic plate with a circular scale attached to the bottom wall shows up in the topview photographs and helps in reading the instantaneous yaw angle. The 0 degree line in the scale was aligned with the model fuselage center line. Also, the angle-of-attack scale fixed to the rear side wall of the tunnel shows up in the sideview photographs and helps in reading of the instantaneous angle of attack. To know the yaw angle in the sideview photographs or the pitch angle in the topview photographs it is necessary to take both the sideview and topview photographs simultaneously. This was accomplished by exposing the two cameras simultaneously using two remote shutter release cables.

#### IV. RESULTS AND DISCUSSION

The results of this investigation will be discussed in a series of 3 numbered photographic sequences and bursting location plots. Several rolls of 35 mm black and white films were exposed and several hours of videotape recorded during this investigation. The results of the 35 mm photography are presented in Appendix A (Figures 7 through 71). Each figure shows two views of the flow field, one in the sideview and the other in the topview (taken from below the test section of the water tunnel). Note that the AOA reading in these photographs is not necessarily the true AOA because the sideview camera was not always focussed exactly at the fuselage centerline of the model. The true AOA was read off the AOA indicator on the control box. The bursting location plots derived from the photographs are included in Appendix B (Figures 72 through 78). The experimental data on vortex bursting location is tabulated in Appendix C (Tables 4 through 8).

However, before discussing these results, some general comments will be made on the effect of angle of attack (AOA) on the wing vortical flow field visualized during the series of preliminary experiments. Then the flow visualization photographs will be examined in detail to highlight the wing vortical flow field characteristics for static sideslip conditions at a given AOA. Finally, with the aid of the photograph and the burst location plots, the effects of the sideslip rate on the development and bursting of the wing root vortices will be discussed.

## **A. EFFECTS OF AOA ON THE WING FLOW FIELD OF X-31A MODEL**

Sequence number 1, Figures 7 through 14. These figures show the effects of AOA on the wing vortical flow field of X-31A model at zero yaw angle. At  $0^\circ$  AOA, the flow over the wing is particularly smooth, attached and symmetric (Figure 7). At  $5^\circ$  AOA, the flow at the inner trailing edge of the wing has dispersed outward (Figure 8). As the angle of attack is increased further, the flow from the inside of the wing root surface progressively disperses outward to the tip, fluctuates, and starts to coil up into a vortex core shape with a maximum vortex core length on the wing surface at about  $12^\circ$  AOA (Figure 9). This vortex core is tightly wound and extends aft until undergoing vortex core breakdown. The vortex core bursting is usually signified by the stagnation of the core and abrupt expansion in its diameter.

As the AOA is increased further, the vortex core bursting point moves upstream over the wing surface (Figures 10 through 13) and finally the bursting occurs very close to the leading edge at about  $50^\circ$  AOA (Figure 14). These effects of AOA on the bursting location of the wing root vortex core at zero yaw angle are illustrated quantitatively in Figure 72. The slope of the bursting location plot is seen to be steeper in the  $12^\circ$  to  $30^\circ$  AOA range than in the  $30^\circ$  to  $50^\circ$  AOA range, suggesting non-uniform movement of the vortex burst with respect to AOA. These observations are similar to the ones made by Kwon (Ref. 6) in his investigation of the wing flow field of X-31A model.

## B. STATIC SIDESLIP EFFECTS

Sequence number 2, figures 15 through 26. These figures show some selected model flow fields under static conditions with the AOA ranging from  $15^\circ$  to  $50^\circ$  for sideslip angles of  $0^\circ$ ,  $5^\circ$ ,  $10^\circ$ ,  $15^\circ$ ,  $20^\circ$ .

Figures 15 to 19 show the development of wing root vortices at constant AOA =  $20^\circ$ , as the sideslip angle increases from  $0^\circ$  to  $20^\circ$ . Figure 15,  $\alpha = 20^\circ$ ,  $\beta = 0^\circ$ , shows a pair of well developed, strong, and symmetrical wing root vortices on either side of the fuselage with either vortex bursting at about 66 % of the wing root chord. As the sideslip angle increases (Figs. 16 and 17), a pair of asymmetrical vortices develops, with the leeward side vortex bursting later than the windward side vortex. With increasing sideslip, the leeward vortex bursting locations move rearward and outboard whereas the windward vortex bursting locations move forward and inboard. The leeward vortex bursting locations for  $\alpha = 20^\circ$ ,  $\beta = 5^\circ$  and  $\alpha = 20^\circ$ ,  $\beta = 10^\circ$  are at 75 % and 81.8 % of the wing root chord, respectively. At  $\beta = 15^\circ$  and  $20^\circ$ , the leeward vortex bursting locations move further backward and into the trailing edge wake and outboard with the windward vortex bursting locations still moving forward (Figs. 18 and 19). It can be seen from these figures that the leeward vortex bursting height from the wing surface increases with the sideslip, this height almost doubling when sideslip changes from  $0^\circ$  to  $20^\circ$ . In addition, the leeward vortex becomes weaker with increasing sideslip angle.

Figures 20, 17, 21 and 22 show the development of wing root vortices at a constant sideslip of  $10^\circ$  as the AOA increases from  $15^\circ$  to  $30^\circ$ . Figure 20,  $\alpha = 15^\circ$ ,  $\beta = 10^\circ$ , shows that

the leeward vortex core initially moves outboard (parallel to leading edge), then inboard (parallel to fuselage), and finally bursts downstream of the trailing edge. Likewise, the windward vortex core moves outboard first, then inboard and finally bursts at 75 % of the wing root chord. With further increase in the AOA, both these burst locations move forward (Fig.17). However, the rate of movement on the windward side is slower than that on the leeward side. Also, the rate of movement of bursting location on either side slows down in the higher AOA range ( $20^{\circ}$ - $30^{\circ}$ ), with the result that almost symmetrical vortices develop and burst in this AOA range (Figs. 21 and 22).

Figures 23 through 26 show the wing root vortices at a sideslip angle of  $20^{\circ}$  as the AOA increases from  $35^{\circ}$  to  $50^{\circ}$ . The height of the leeward vortex bursting location from the wing surface increases as the vortex bursting moves outboard in this AOA range. In particular, the windward vortices are developed more inboard and their burst locations lag those on the leeward side.

To summarize the sideslip effects for static conditions, at a small sideslip angle ( $\beta = 5^{\circ}$ ,  $10^{\circ}$ ) in the  $15^{\circ}$ - $20^{\circ}$  AOA range, an asymmetric wing root vortex pair is seen to develop with the wing root vortex core bursting later on the leeward side than on the windward side. In the  $25^{\circ}$ - $30^{\circ}$  AOA range, the vortices become symmetrical and burst at approximately the same location on both the leeward side and the windward side. In the  $35^{\circ}$ - $50^{\circ}$  AOA range, the vortices become asymmetrical once again with the windward side vortex bursting later than the leeward side vortex. At a sideslip angle of  $20^{\circ}$  (for AOA  $> 30^{\circ}$ ) a weak rolling vortex is observed to develop on the leeward side that causes the bursting location to move both outward and upward as can be seen in the photographs (Figs. 23 through 26). Similar

trends were observed by CAVAZOS in his investigation of static sideslip effects on bursting of LEX vortices of F/A-18 aircraft model [Ref. 15] and by Del Frate and Zuniga in their in-flight investigations [Ref.19].

## C. DYNAMIC SIDESLIP EFFECTS

Sequence number 3 (Figures 27 through 71) shows some selected model flow fields during simple sideslipping motions (sideslip increasing from  $0^\circ$  to  $20^\circ$  and sideslip decreasing from  $20^\circ$  to  $0^\circ$ ) at two reduced yaw rates and constant AOAs of  $15^\circ$ ,  $20^\circ$ ,  $25^\circ$ ,  $30^\circ$ ,  $35^\circ$ ,  $40^\circ$ ,  $45^\circ$  and  $50^\circ$ .

### 1. Sideslip - Increase Motion (Positive sideslipping)

In figures 27 through 31 the model is sideslipping at 2.8 deg/sec with  $\text{AOA}=20^\circ$ . The sideslip on the leeward side is increasing at a reduced yaw rate of 0.08. As sideslipping starts at  $\beta=0^\circ$ , figure 27 essentially represents the static flow field (same as in Fig. 15). Figure 28,  $\beta=5^\circ$ , shows a pair of asymmetric vortices with the leeward side vortex clearly lagging. However, the amount of asymmetry is less than that in the corresponding static case (Fig. 16,  $\alpha=20^\circ$ ,  $\beta=5^\circ$ ).

As the sideslip is increased further (Figs. 29 through 31), the leeward side vortex bursting location moves outboard and rearward whereas the windward side vortex bursting location moves forward with little change in its lateral position. At  $\beta=15^\circ$  and  $20^\circ$  (Figs. 30 and 31) the leeward side vortex splits into two segments. The segments develop into weak vortices initially, and finally rejoin again at the bursting point.

Figures 32, 29, 33 and 34 show the development of wing root vortices at the instantaneous sideslip of  $10^\circ$  for AOAs of  $15^\circ$ ,  $20^\circ$ ,  $25^\circ$  and  $30^\circ$ , respectively. The trends seen in these figures are similar to those discussed earlier under static sideslip effects (Figs. 20, 17, 21 and 22), with the vortices bursting almost symmetrically on either side of the fuselage at  $\alpha=30^\circ$  (Fig.34). However, the leeward vortices burst earlier than in the static case at each AOA. The reason for the earlier bursting may be attributed to the so-called dynamic lag effect. During the dynamic motion, with positive sideslipping, the effective angle of attack on the leeward side is decreasing in this AOA range, which causes earlier bursting of the vortex compared to the static case.

Figures 35 through 37 correspond to the development of wing root vortices at the instantaneous sideslip of  $20^\circ$  for AOAs of  $35^\circ$ ,  $45^\circ$  and  $50^\circ$ , respectively. At  $\alpha=35^\circ$ ,  $\beta=20^\circ$  (Fig. 35), the leeward side vortex moves outboard (parallel to the leading edge) and the windward side vortex inboard (parallel to fuselage). As the AOA increases to  $45^\circ$  and  $50^\circ$  (Figs. 36 and 37) the leeward side vortex moves inboard with the bursting location moving forward while the windward side vortex still remains inboard and bursts later relative to the leeward side vortex.

In figures 38 through 49 the model is sideslipping at  $1.8 \text{ deg/sec}$  with different AOAs. The sideslip on the leeward side is increasing at a reduced yaw rate of  $0.05$ . Because the sideslipping motion starts at  $\beta=0^\circ$ , the flow field represented in figure 38,  $\alpha=20^\circ$  and  $\beta=0^\circ$ , is essentially a static flow field as in Fig.15. The flow field in figure 39,  $\alpha=15^\circ$  and  $\beta=5^\circ$  is somewhat similar to the sideslipping case shown in figure 28 ( $\alpha=20^\circ$ ,  $\beta=5^\circ$ ). As the sideslip increases further to  $\beta=10^\circ$  (Fig. 40), the leeward side vortex bursting location

moves backward and outboard while the windward side vortex bursting location moves a little forward with no appreciable lateral shift. The leeward side vortices, at last, burst out at  $\beta = 20^\circ$  (Fig. 41); the leeward side vortex bursts downstream of the leading edge which compares with the bursting in the static case (Fig. 19).

Figures 42 through 44 display the flow field at the instantaneous sideslip of  $10^\circ$  for AOAs of  $15^\circ$ ,  $25^\circ$  and  $30^\circ$ , respectively. The trends seen in these figures are similar to those discussed earlier under dynamic sideslip effects at the higher yaw rate (Figs. 32 through 34). However, at each AOA the leeward side vortex bursts later than in the higher yaw rate case but earlier than in the static case. Thus the associated dynamic lag effects have decreased at this lower yaw rate.

Figures 45 through 48 correspond to the model flow field at the instantaneous sideslip of  $20^\circ$  for AOAs of  $35^\circ$ ,  $40^\circ$ ,  $45^\circ$  and  $50^\circ$ , respectively. These figures clearly show that in this AOA range, the bursting of the wing root vortex occurs earlier on the leeward side than on the windward side. Also, the vortex bursting features in this AOA range are very similar to the ones discussed earlier for the static case in the same AOA range. The dynamic lag effects are present, but at a reduced level.

## **2. Sideslip-Decrease Motion (Negative Sideslipping)**

As in the previous case, two reduced yaw rates will be considered corresponding to  $\dot{\beta} = -2.8$  deg/sec and  $-1.80$  deg/sec.

Figures 49 through 53 show the development of the vortical flow field with the model sideslipping at  $-2.8$  deg/sec at a constant AOA =  $20^\circ$ . This sideslip on the leeward



side is decreasing from  $\beta = 20^\circ$  to  $0^\circ$  at a reduced yaw rate of 0.08. The leeward side vortex burst occurs downstream of the trailing edge for  $\beta = 20^\circ$ ,  $15^\circ$  and  $10^\circ$  (Figs.49, 50 and 51) and upstream almost at the trailing edge for  $\beta = 5^\circ$  (Fig. 52) and upstream of the trailing edge for  $\beta = 0^\circ$  (Fig.53). In the static case, the corresponding burst locations occur much earlier. For example, with  $\beta = 10^\circ$  and  $\alpha = 20^\circ$  (Fig.17) the leeward side vortex burst occurs at 81.8 % of wing root chord. The delayed bursting in the dynamic case is once again due to the dynamic lag referred to earlier. It is also seen that the leeward side vortex moves from the outboard to the inboard while the windward side vortex moves in the reverse order.

Figures 54 and 55 display the model flow field at the instantaneous sideslip of  $10^\circ$ , for AOAs of  $15^\circ$  and  $25^\circ$ , respectively. There is no leeward side vortex bursting on the wing surface at  $\alpha = 15^\circ$  (Fig.54). It just starts to show up on the wing surface at  $\alpha = 25^\circ$  (Fig.55).

Figures 56 through 59 correspond to the model flow field at the instantaneous sideslip of  $0^\circ$ , for AOAs of  $35^\circ$ ,  $40^\circ$ ,  $45^\circ$  and  $50^\circ$ , respectively. In this AOA range, the leeward side vortex burst location moves forward with the increase in AOA. However, this rate of forward movement is quite small when compared with the movement in the  $15^\circ$ - $30^\circ$  AOA range. Little movement of vortices either toward the inboard or the outboard is observed on both the leeward side and the windward side. A pair of almost symmetric vortices is seen but the bursting of the leeward side vortex occurs a little bit earlier than the windward side vortex.

Figures 60 through 64 show the development of vortical flow field with the model sideslipping at  $-1.8$  deg/sec at a constant AOA  $= 20^\circ$ . The sideslip on the leeward side

is decreasing from  $\beta=20^\circ$  to  $0^\circ$  at a reduced yaw rate of 0.05. Because the sideslipping motion starts at  $\beta=20^\circ$ , the flow field represented in figure 60,  $\alpha=20^\circ$ ,  $\beta=20^\circ$ , is essentially a static flow field as in Fig.19. The vortex development trends in these figures are qualitatively similar to those observed earlier for the sideslipping motion at -2.8 deg/sec (Figs. 49 through 53). For  $\beta=20^\circ$ ,  $15^\circ$  and  $10^\circ$  (see Figs. 60 through 62) the leeward side vortex bursting occurs downstream of the trailing edge. At  $\beta=5^\circ$ , it occurs at 88.6 % of the wing root chord (Fig.63), as compared to the 95.5 % bursting location for the sideslipping motion at -2.8 deg/sec (Fig. 52). This difference in the bursting location between the two sideslipping motions implies that the dynamic lag effect on the model decreases with decreasing rate. These figures also indicate that the leeward side vortex bursts later than the windward side vortex during the sideslipping motion from  $20^\circ$  to  $0^\circ$ .

Figures 65 through 67 display the model flow field at the instantaneous sideslip of  $10^\circ$  for AOAs of  $15^\circ$ ,  $25^\circ$  and  $30^\circ$ , respectively. The leeward side vortex bursts downstream of the trailing edge at  $\alpha=15^\circ$  (Fig. 65); starts moving upstream, lags the windward side location at  $\alpha=25^\circ$  (Fig.66) and finally leads the windward side burst location at  $\alpha=30^\circ$  (Fig. 67).

Figures 68 through 71 correspond to the model flow field at the instantaneous sideslip of  $0^\circ$  for AOAs of  $35^\circ$ ,  $40^\circ$ ,  $45^\circ$  and  $50^\circ$ , respectively. The leeward side vortex bursting location moves forward with AOA, but the rate of forward movement is small compared to that during the sideslipping motion at -2.8 deg/sec. The windward side vortex burst location is lagging the leeward side location, but the pair of vortices tends to become symmetric with increasing AOA.

To summarize the effects of sideslip for dynamic conditions, the trends observed in the wing root vortex development and bursting characteristics are similar to those for the static case and the dynamic lag effects play a key role. At relatively low AOAs ( $15^\circ$ - $20^\circ$ ) the leeward side vortex bursts later than the windward side vortex, a pair of almost symmetric vortices develops in the  $25^\circ$  -  $30^\circ$  AOA range and finally, for  $\text{AOA} > 30^\circ$ , a pair of asymmetric vortices develops with the windward side vortex bursting later than the leeward side vortex. During the positive sideslipping motion, the vortex bursting location on the leeward side occurs earlier than in the equivalent static case. Likewise, during the negative sideslipping motion, the vortex bursting location on the leeward side occurs later than in the equivalent static case. These dynamic lag effects are a function of the reduced yaw rate (nondimensional sideslipping rate).

#### D. BURSTING LOCATION PLOTS

The wing root vortex core bursting locations for both static conditions and dynamic sideslip motions are plotted as a function of angle of attack in figures 73 through 78 (Appendix B). The plots are obtained from the data listed in Tables 4 through 8 (Appendix C). It should be noted that in these figures the bursting location refers to the bursting of the wing root vortex on the leeward side only.  $X_b$  represents longitudinal distance of vortex bursting location from the leading edge of the wing root chord of length  $C_{wr}$ .

Figure 73 shows the effect of sideslip on the bursting location of the wing root vortex for the static case. It is clear from the figure that the major effect of sideslip is to delay the vortex bursting on the leeward side throughout the AOA range tested ( $15^\circ$  -  $50^\circ$ ). At

AOA = 15°, the leeward side vortex bursts on the wing surface for only two sideslip angles,  $\beta = 0^\circ$  and 5°, and at AOA = 20°, for only three sideslip angles of  $\beta = 0^\circ$ , 5° and 10°.

In the 15° - 30° AOA range the sideslip input causes a rapid movement of burst location toward the trailing edge, but the rate of this rearward movement of burst location with sideslip input decreases considerably in the 30° - 50° AOA range.

Figure 74 compares the negative sideslipping motions for two reduced yaw rates with the static case for 0° sideslip angle. It can be seen clearly that during the negative sideslipping motions in the AOA range considered, the vortex bursting location on the leeward side always occurs later relative to the static case. Thus the burst location curves for the dynamic motion consistently overshoot the corresponding static case curve during negative sideslipping. This is clearly seen in the photographs (see Figs. 15 and 53). The overshoot is seen to increase with the rate of sideslip, although this increase is reduced for AOA > 30°. It should be noted here that the curves corresponding to positive sideslipping motion for two reduced yaw rates coincide with the static curve for  $\beta = 0^\circ$  case (as the sideslipping starts at  $\beta = 0^\circ$ ).

Figures 75, 76, and 77 show the bursting location plots highlighting the dynamic sideslip effects relative to the static case during positive sideslipping and negative sideslipping motions for two reduced yaw rates. These figures correspond to instantaneous sideslip angles of 5°, 10° and 15°, respectively. Throughout the whole AOA range, it is seen that relative to the static case, the vortex bursting on the leeward side always occurs earlier during the positive sideslipping motion but later during the negative sideslipping motion. Therefore, the bursting location curves for the positive sideslipping motion consistently

undershoot the corresponding curve for the static case while those for the negative sideslipping motion overshoot the static curve. The burst location curves for the dynamic motion as well as the static case exhibit similar slope with respect to AOA, the slope being steeper for  $AOA < 30^\circ$ . This indicates that the rate of forward movement of the burst location decreases at higher AOAs.

Finally, figure 78 compares the positive sideslipping motions for two reduced yaw rates with the static case for  $20^\circ$  sideslip angle. As before, the bursting location curves consistently undershoot the corresponding static case curve during the positive sideslipping motions. In the static case for  $AOA < 20^\circ$ , the leeward side vortex bursts outside the wing surface, whereas for the positive sideslipping motion with high yaw rate, it bursts upstream of the trailing edge. The slopes of the curves in this figure are similar to those of previous figures. It should be noted here that the curves corresponding to negative sideslipping motion for two reduced yaw rates coincide with the static curve for  $\beta = 20^\circ$  case (as the sideslipping starts at  $\beta = 20^\circ$ ).

## V. CONCLUSIONS AND RECOMMENDATIONS

A low speed flow visualization investigation was initiated to study the vortex development and bursting phenomena on a 2.3 % scale model of a X-31A-like fighter aircraft using dye injection in the NPS water tunnel. The main focus of this study was two-fold : First, to study the effects of angle of attack and static sideslip on the vortical flow field. Secondly, to study the effect of dynamic sideslip motion at two reduced yaw rates. The water tunnel visualization data reported here is believed to be the first of its kind for a canard-configured X-31A-like aircraft model in dynamic sideslipping motion. The following conclusions are drawn from the results of the experimental investigation:

1. Effects of AOA: As the AOA increases from  $15^\circ$  to  $50^\circ$ , a pair of symmetric vortices develops and the bursting locations move upstream, indicating that the separated flow region increases at higher angles of attack.
2. Static Sideslip Effects: Vortex core bursting location is also a function of sideslip angle. At a constant AOA, the leeward side vortex bursting location moves backward and outboard with sideslip inputs and the windward side vortex bursting location moves forward and inboard. The vortex asymmetry switches sides as the AOA is increased. For example, a pair of asymmetric vortices observed in the  $15^\circ$ - $20^\circ$  AOA range, becomes almost symmetrical in the  $25^\circ$ - $30^\circ$  AOA range, but changes back to asymmetry with sides switched in the  $30^\circ$ - $50^\circ$  AOA range.

3. Dynamic Sideslip Effects: During the positive sideslipping motion the leeward side vortex bursting occurs earlier relative to the static case. During the negative sideslipping motion the leeward side vortex bursting occurs later relative to the static case. These dynamic lag effects associated with sideslipping motion increase with the magnitude of the sideslipping motion (that is with the reduced yaw rate).

The following recommendations are made based on this investigation:

1. A scale for the sideslip is highly recommended at the back of the model, preferably below the model support.
2. An automated dye injection system for carrying out the dynamic flow visualization experiments is highly recommended.
3. This flow visualization experiment should be extended to study the dynamic condition in which pitch and sideslip vary simultaneously.

## LIST OF REFERENCES

1. Thomas P. Mcatee, "Agility in Demand", Aerospace America, May 1988.
2. Michael A. Dornheim, "X-31 Flight Tests to Explore Combat Agility to 70 Degree AOA", Aviation Week and Space Technology, March 1991.
3. P.T. Yeh, M.W. George, W.C. Clever, C.K. Tam, C.J. Woan, "Numerical Study of the X-31 High AOA Flow Characteristics", AIAA-91- 1630, June 1991.
4. W.B. Herbst, "Future Fighter Technologies", Journal of Aircraft, Vol.17 No.8, August 1980.
5. D.Hummel and H-Chr.Oelker, "Effects of Canard Position on the Aerodynamic Characteristics of a Close-Coupled Canard Configuration at Low Speed", Agard Conference Proceedings No.465.
6. H.M. Kwon, Water Tunnel Flow Visualization Studies of a Canard-Configured X-31A-Like Fighter Aircraft Model, Master's Thesis, NPS, Monterey, California, September 1990.
7. S.K. Hebbar, M.F. Platzer, H.M. Kwon, "Static and Dynamic Water Tunnel Flow Visualization Studies of a Canard-Configured X-31A-Like Fighter Aircraft Model", AIAA-91-1629, 22nd Fluid Dynamics, Plasma Dynamics and Laser Conference, June 24-26, 1991/Honolulu, Hawaii.
8. J. Er-El, A. Seginer, "Vortex Trajectories and Breakdown on Wing-Canard Configurations", Journal of Aircraft, Vol.22 No.8, August 1985.
9. David Manor, "Flow over Double Delta Wing and Body at High AOA", Journal of Aircraft, Vol.22 No.1, January 1985.
10. B.B. Gloss, L.W. McKinney, Canard-Wing Lift Interference Related to Maneuvering Aircraft at Subsonic Speeds, NASA TMX-2897, December 1973.
11. B.B. Gloss, Effect of Canard Location and Size on Canard-Wing Interference and Aerodynamic Center Shift Related to Maneuvering Aircraft at Transonic Speeds, NASA TND-7505, June 1974.
12. William P. Henderson, The Effect of Canard and Vertical Tails on the Aerodynamic Characteristics of a Model with a 59 Degree Swept Back Wing at a Mach number of 0.30, NASA TMX-3088, September 1974.



13. J. Er-El, "Effect of Wing/Canard Interference on the Loading of a Delta Wing", Journal of Aircraft, Vol.25 No.1, January 1988.
14. Nick G. Verhaagen, Steven H.J. Naarding, "Experimental and Numerical Investigation of Vortex Flow over a Sideslipping Delta Wing", Journal of Aircraft, Vol.26 No.11, November 1989.
15. O.V. Cavazos, A Flow Visualization Study of LEX Generated Vortices on a Scale Model of a F/A-18 Fighter Aircraft at High Angles of Attack, Master's Thesis, NPS, Monterey, California, June 1990.
16. S.K. Hebbar, M.F. Platzer, O.V. Cavazos, "A Water Tunnel Investigation of the Effects of Pitch Rate and Yaw on LEX Generated Vortices of an F/A-18 Fighter Aircraft Model", AIAA-91-0280, January 7-10, 1991/Reno, Nevada.
17. User's Manual, Flow Visualization Water Tunnel Operation's Manual for Model 1520, Eidetics International, Inc., Torrance, California, 1988 (prepared for NPS, Monterey, California).
18. D.Manor, L.Miller, W.H. Jr. Wentz, "Static and Dynamic Water Tunnel Tests of Slender Wings and Wing-Body Configuration at Extreme Angle of Attack", AIAA-90-3027-CP, August 20-22, 1990/Portland, Oregon.
19. J.H.D. Frate, F.A. Zuniga, "In-Flight Flow Field Analysis on the NASA F-18 High Alpha Research Vehicle with Comparisons to Ground Facility Data", AIAA-90-0231, 28th Aerodynamic Science Meeting, January 8-11, 1990/Reno, Nevada.

## **APPENDIX A. EXPERIMENTAL RESULTS (PHOTOGRAPHS)**

**FIGURES 7 THROUGH 71**

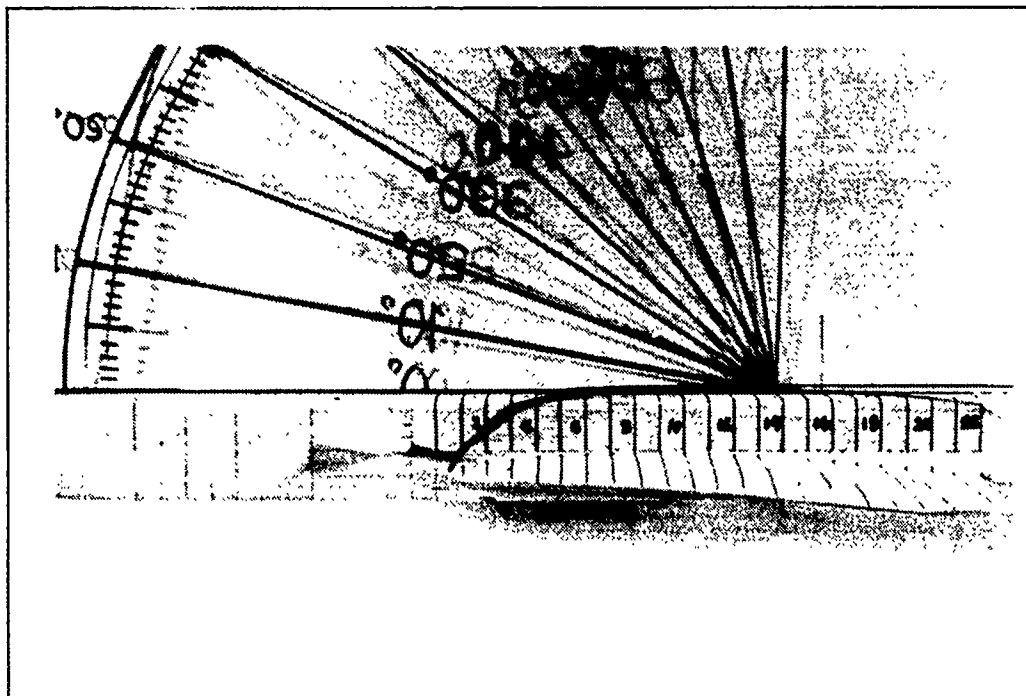
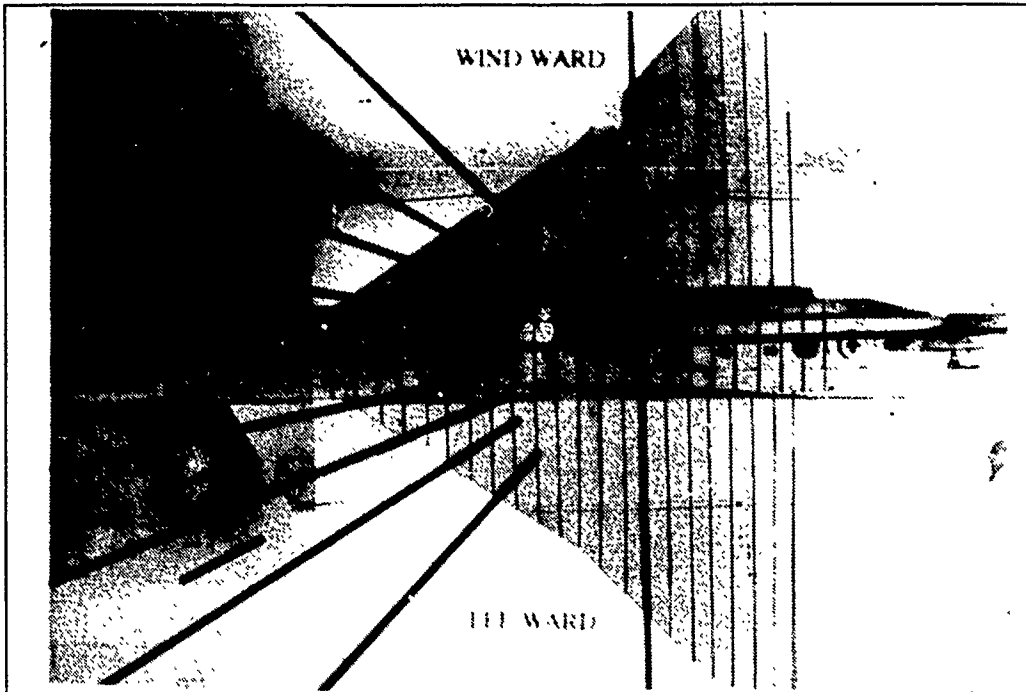


Figure 7. Wing Root Vortex Flow, Static Case,  $\alpha=0^\circ$ ,  $\beta=0^\circ$

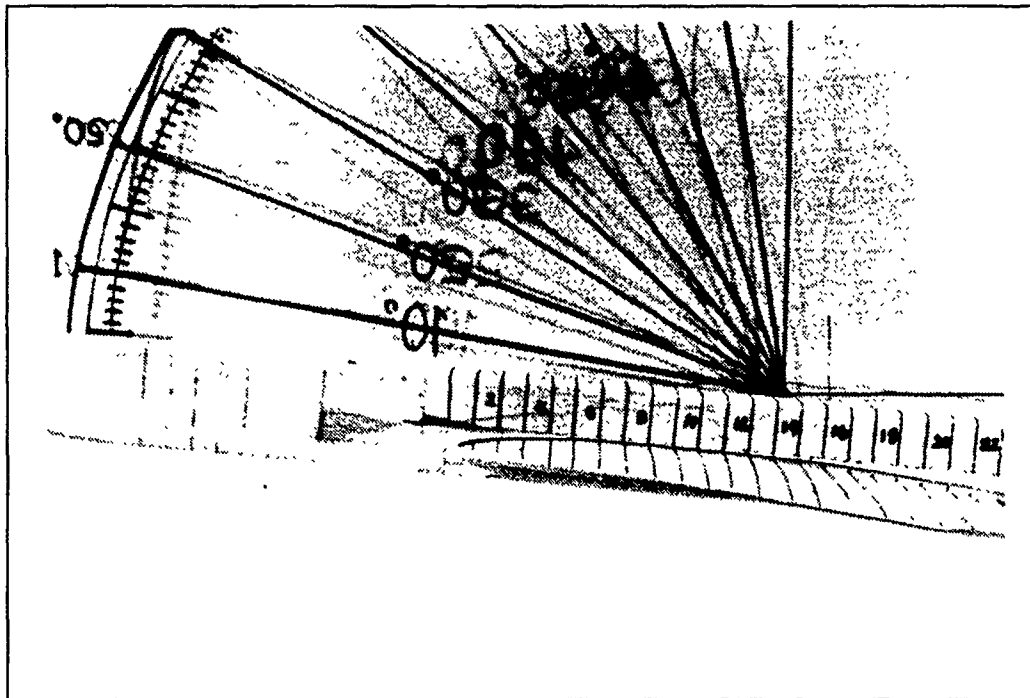
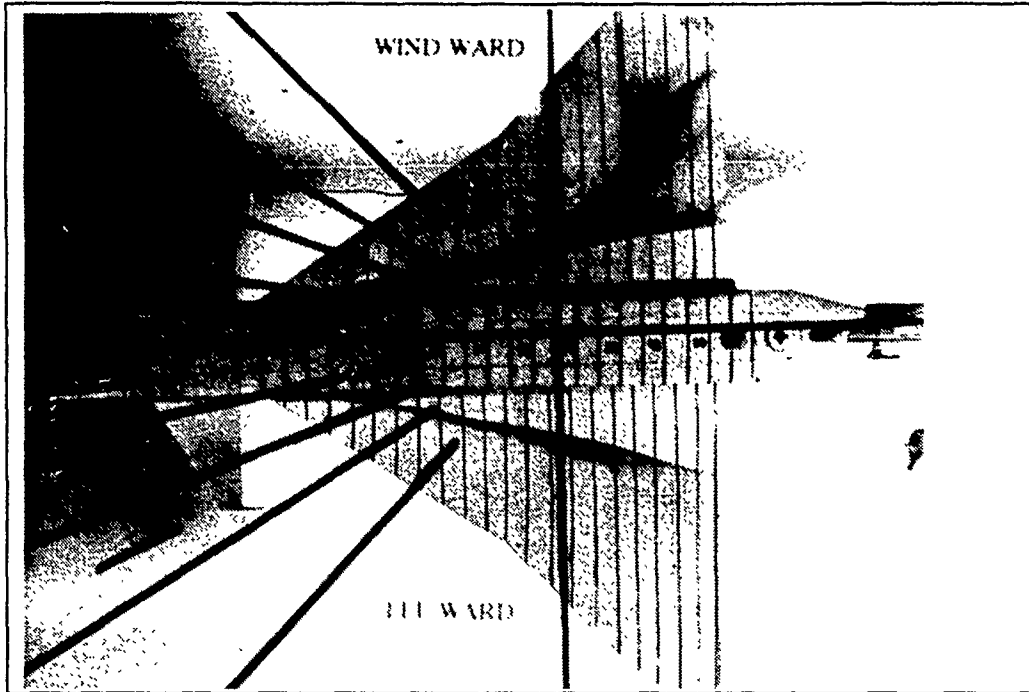


Figure 8. Wing Root Vortex Flow, Static Case,  $\alpha=5^\circ$ ,  $\beta=0^\circ$

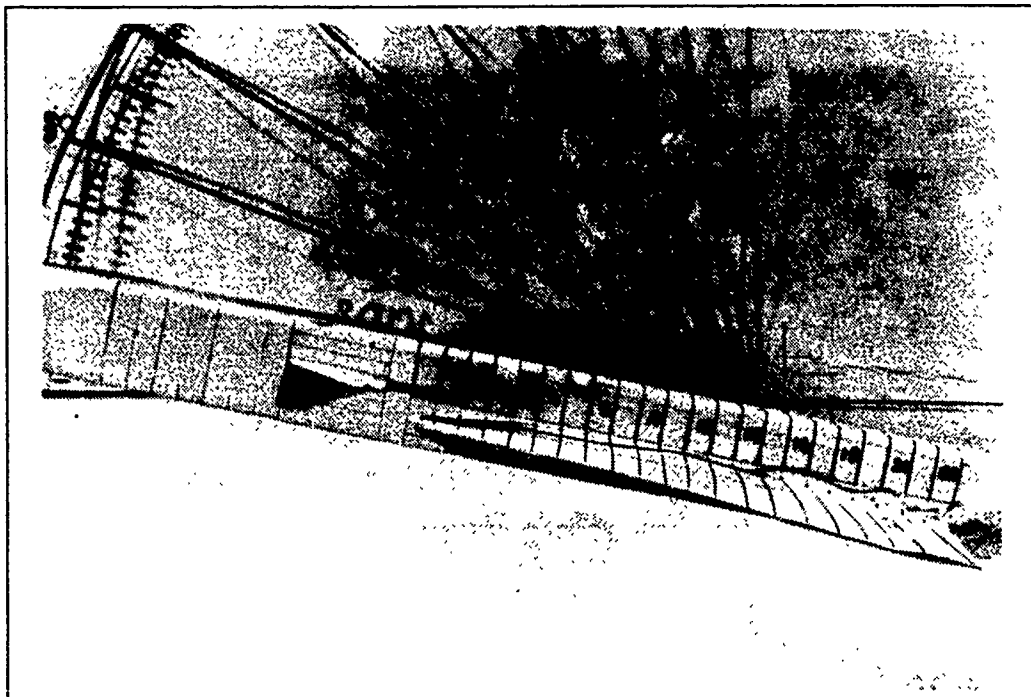
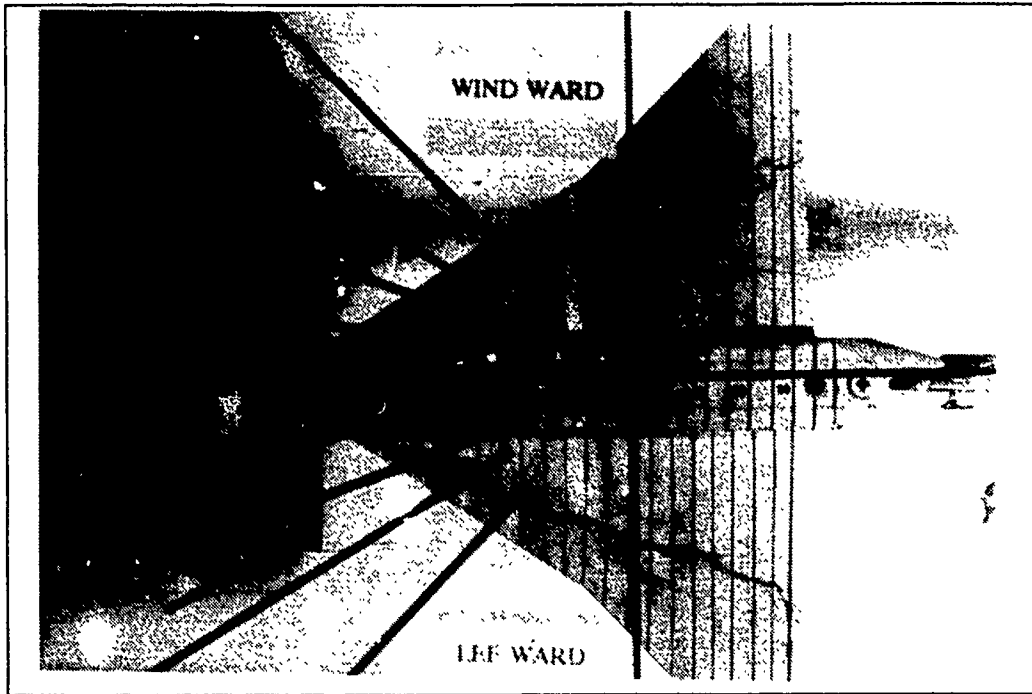


Figure 9. Wing Root Vortex Flow, Static Case,  $\alpha=12^\circ$ ,  $\beta=0^\circ$

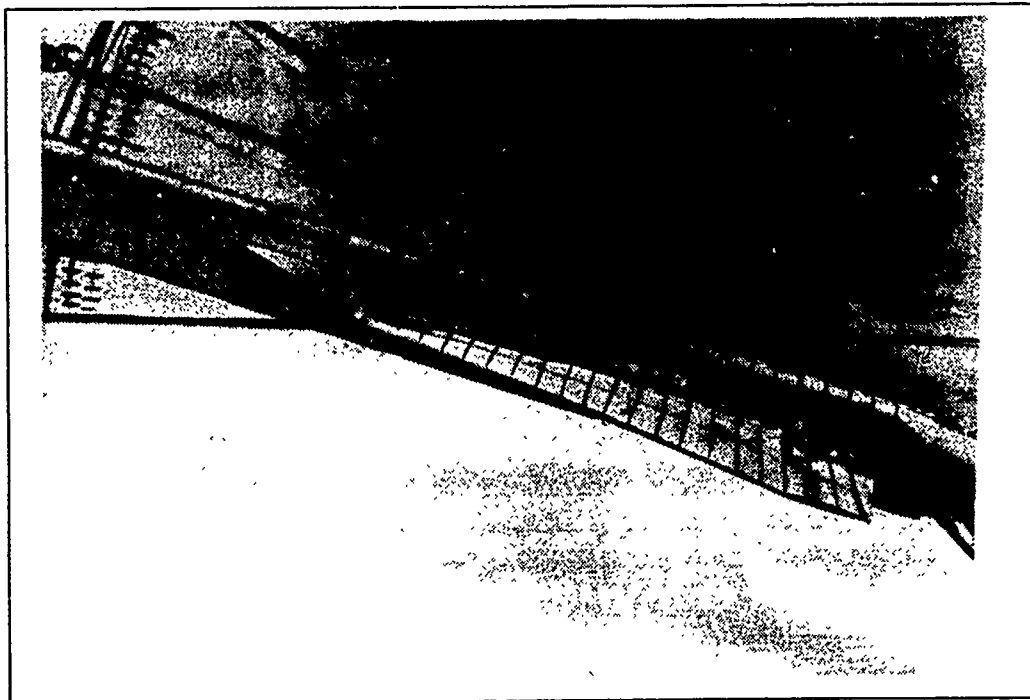
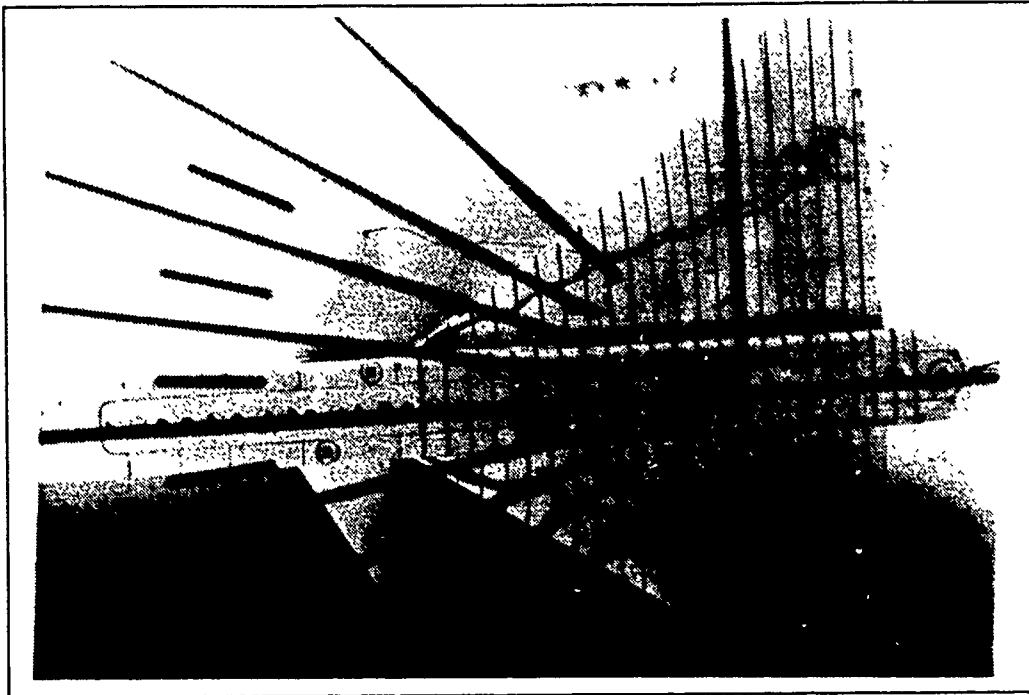


Figure 10. Wing Root Vortex Flow, Static Case,  $\alpha=15^\circ$ ,  $\beta=0^\circ$

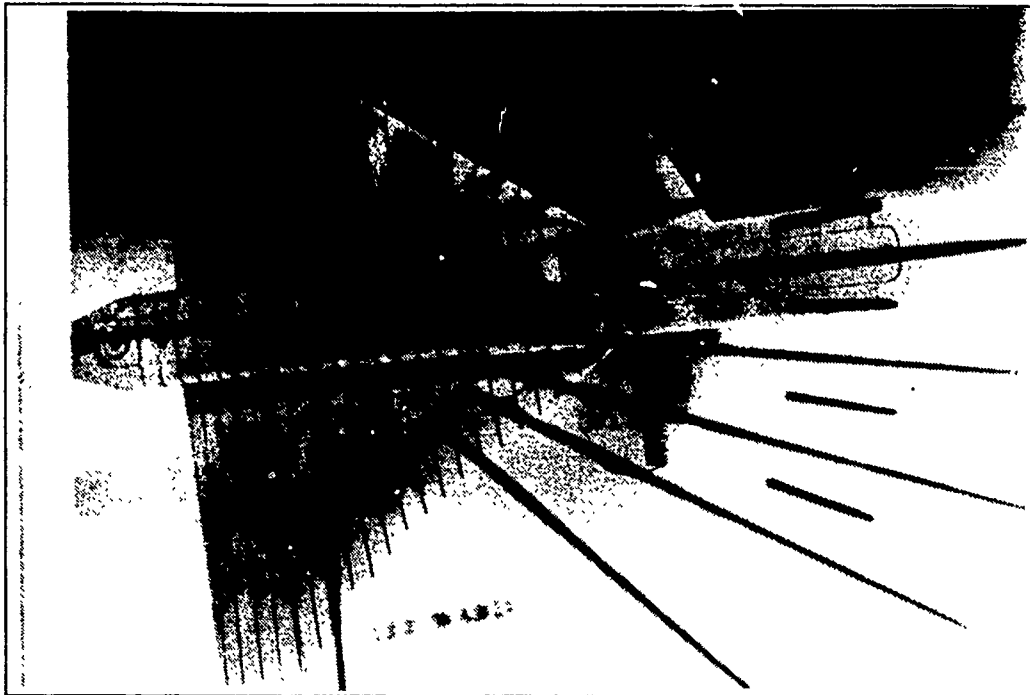


Figure 11. Wing Root Vortex Flow, Static Case,  $\alpha=25^\circ$ ,  $\beta=0^\circ$

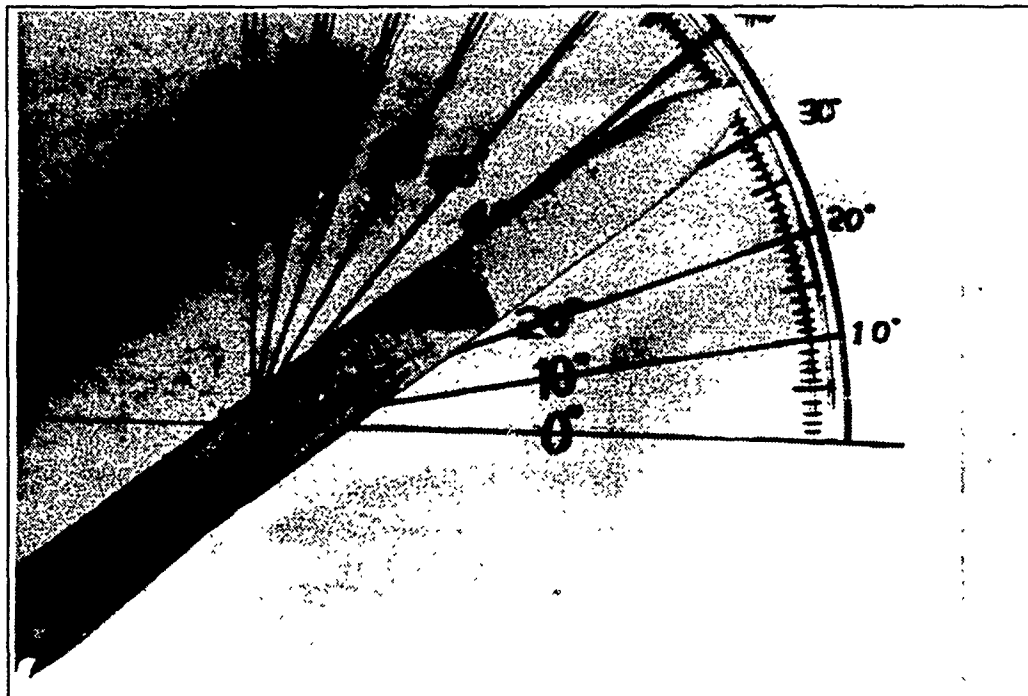
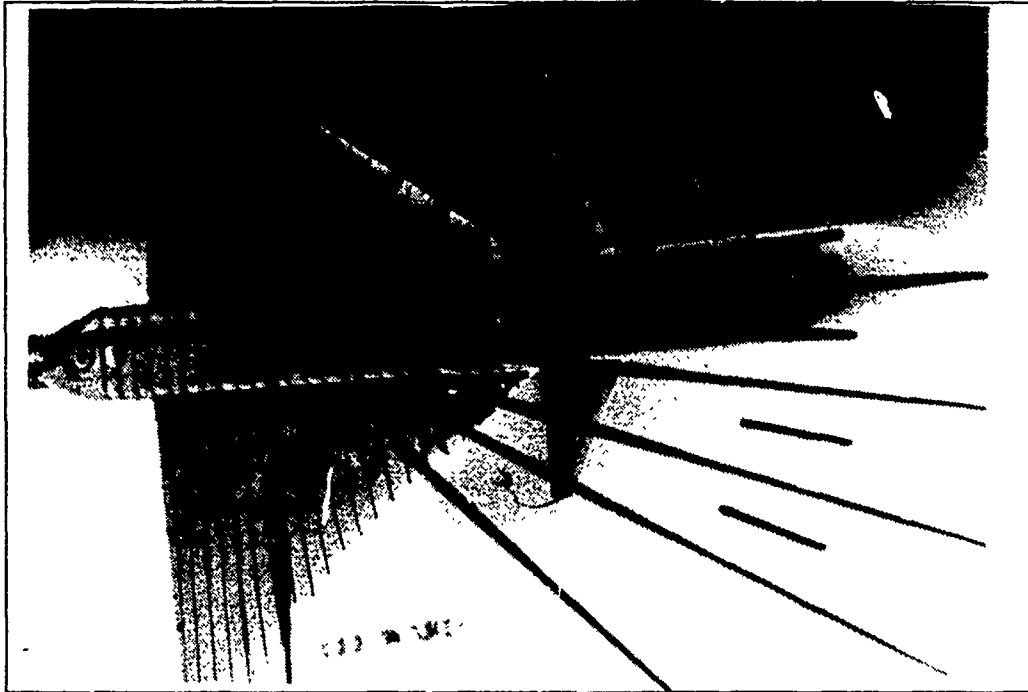


Figure 12 Wing Root Vortex Flow, Static Case,  $\alpha=35^\circ$ ,  $\beta=0^\circ$



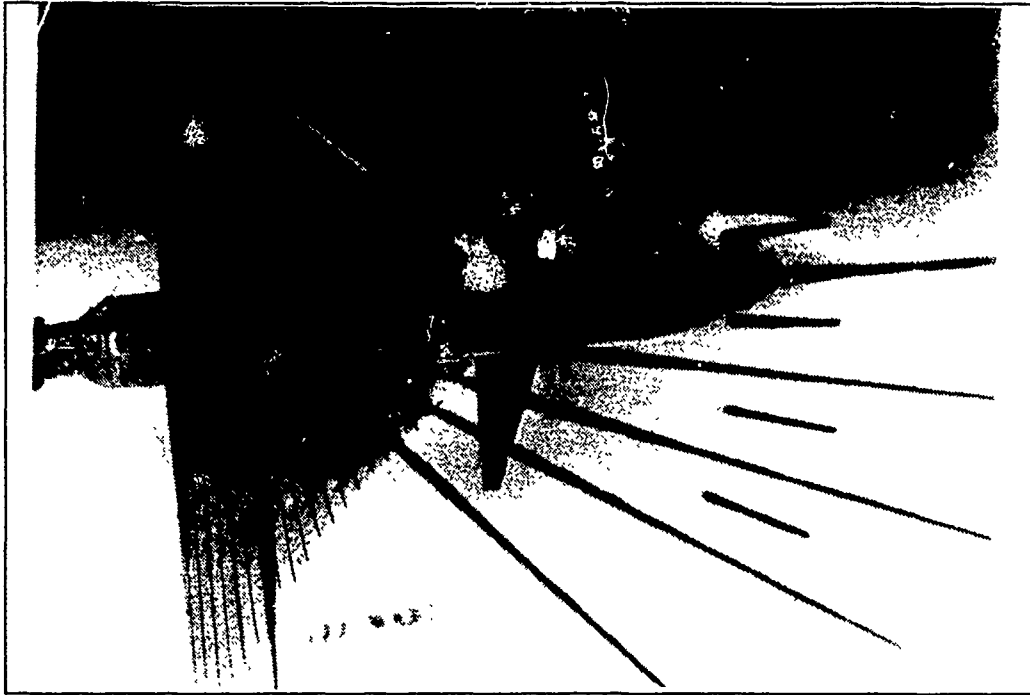


Figure 13. Wing Root Vortex Flow, Static Case,  $\alpha=45^\circ$ ,  $\beta=0^\circ$

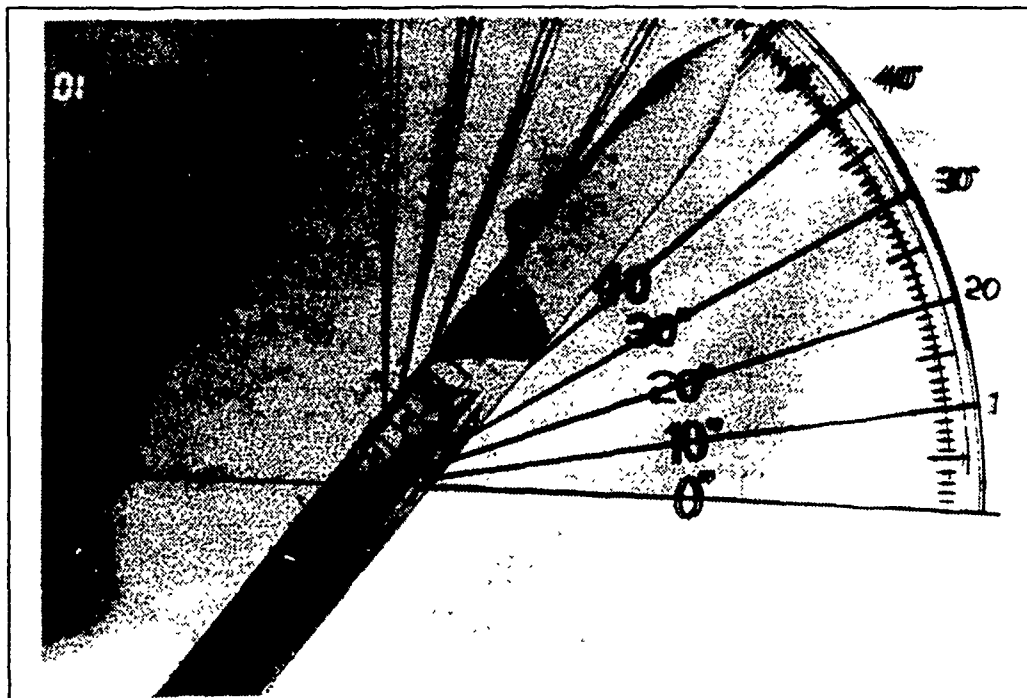


Figure 14. Wing Root Vortex Flow, Static Case,  $\alpha=50^\circ$ ,  $\beta=0^\circ$

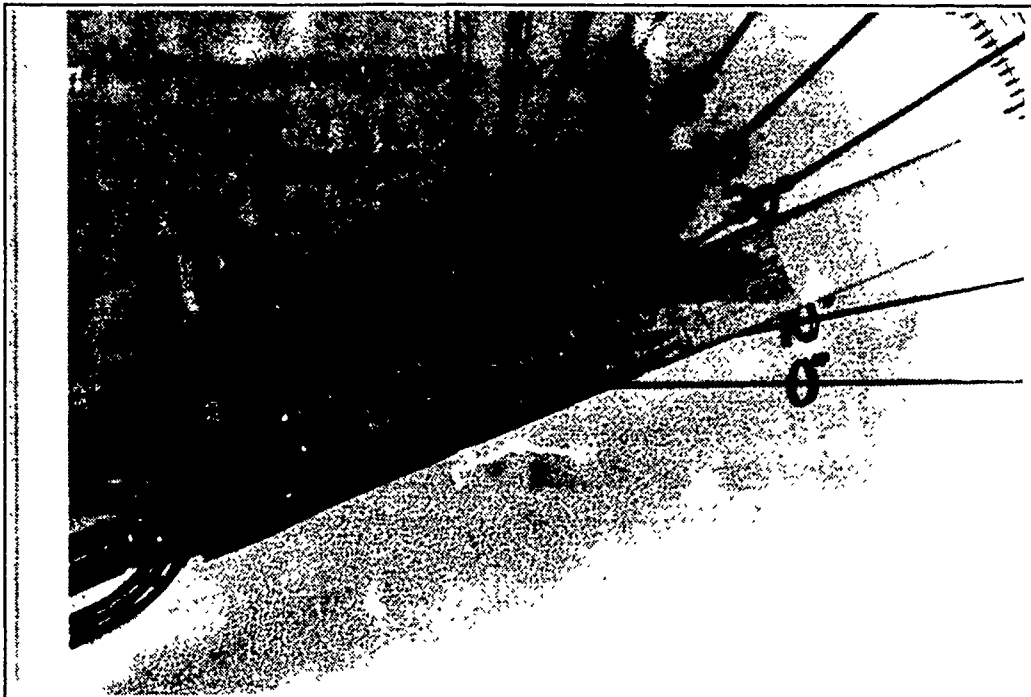
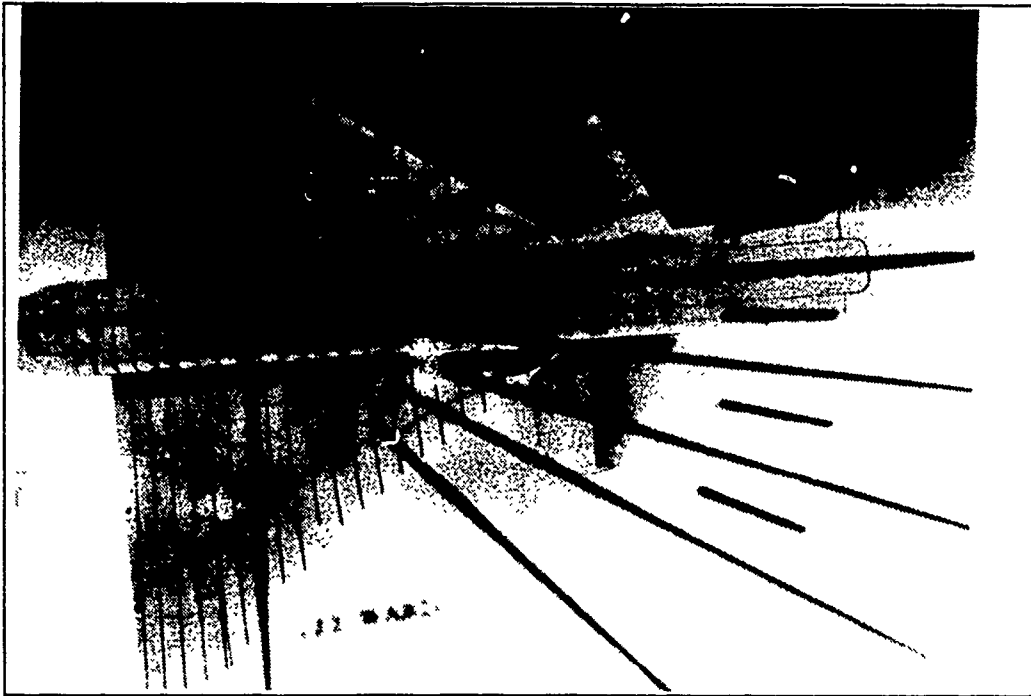


Figure 15. Wing Root Vortex Flow, Static Case,  $\alpha=20^\circ$ ,  $\beta=0^\circ$

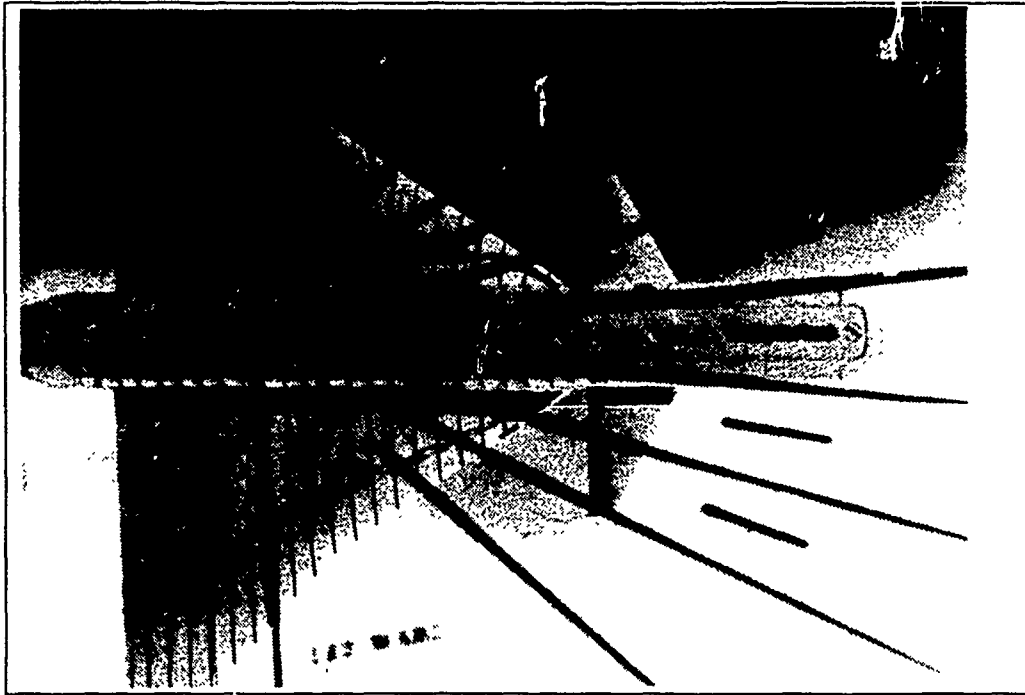


Figure 16. Wing Root Vortex Flow, Static Case,  $\alpha=20^\circ$ ,  $\beta=5^\circ$

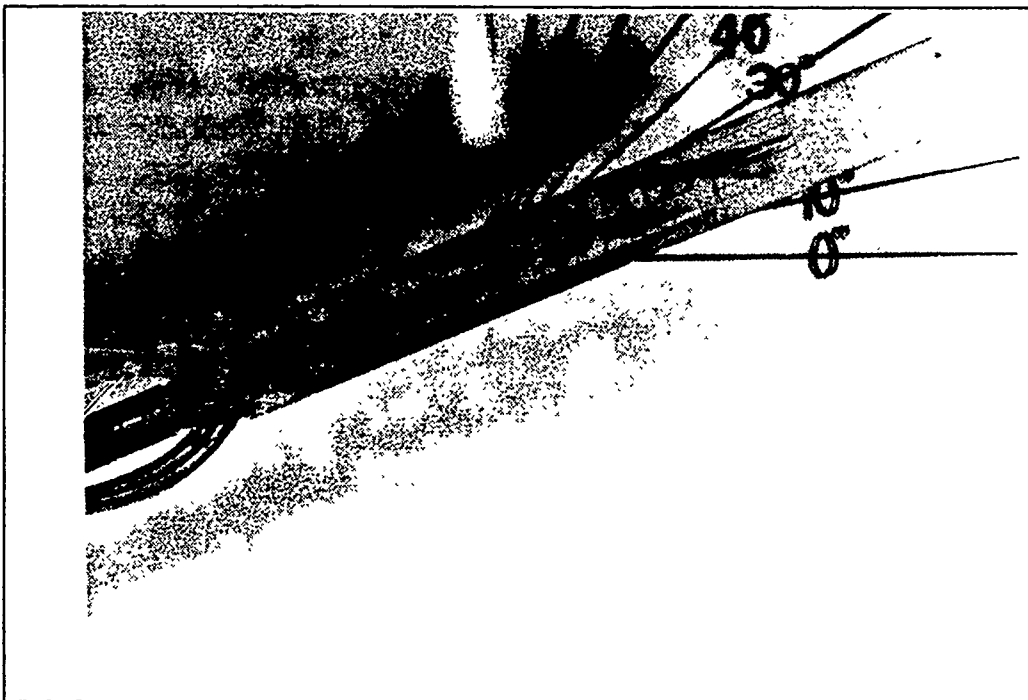
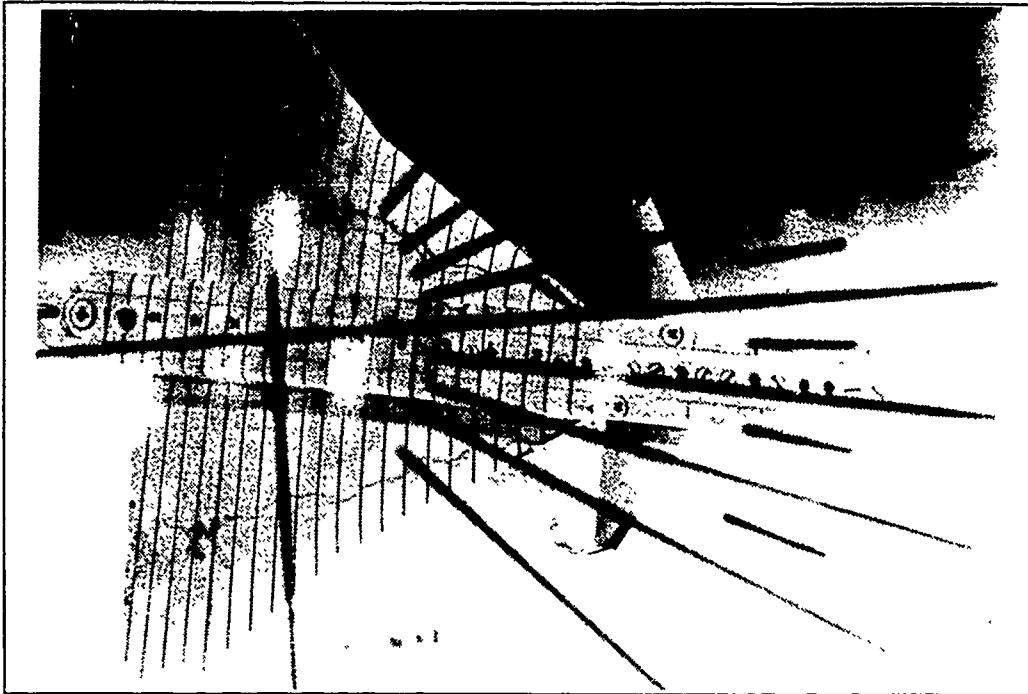


Figure 17. Wing Root Vortex Flow, Static Case,  $\alpha=20^\circ$ ,  $\beta=10^\circ$

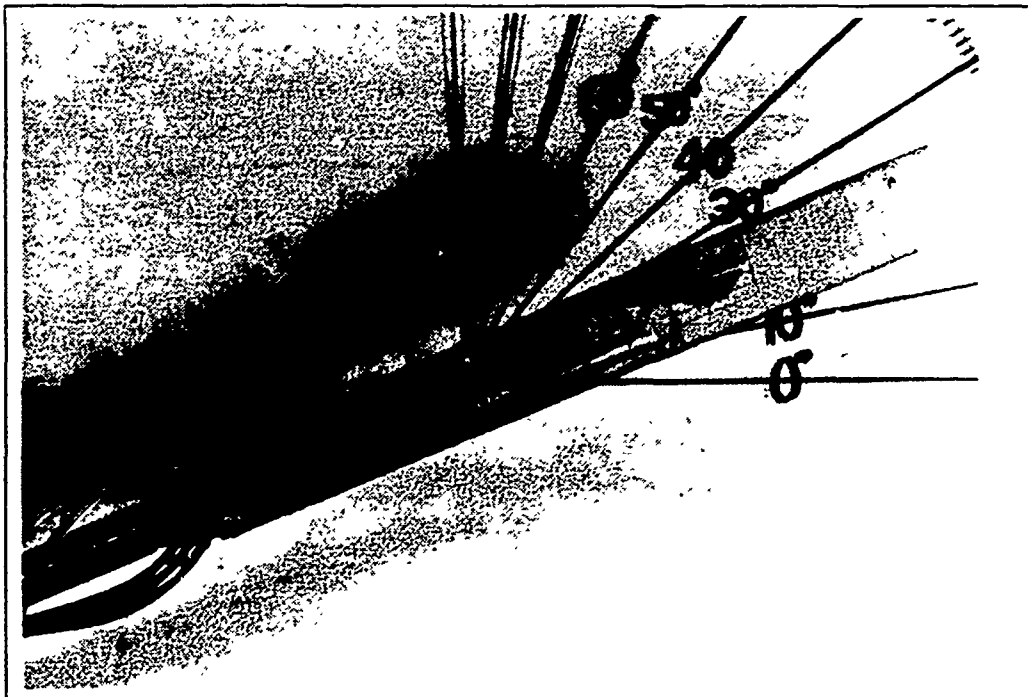
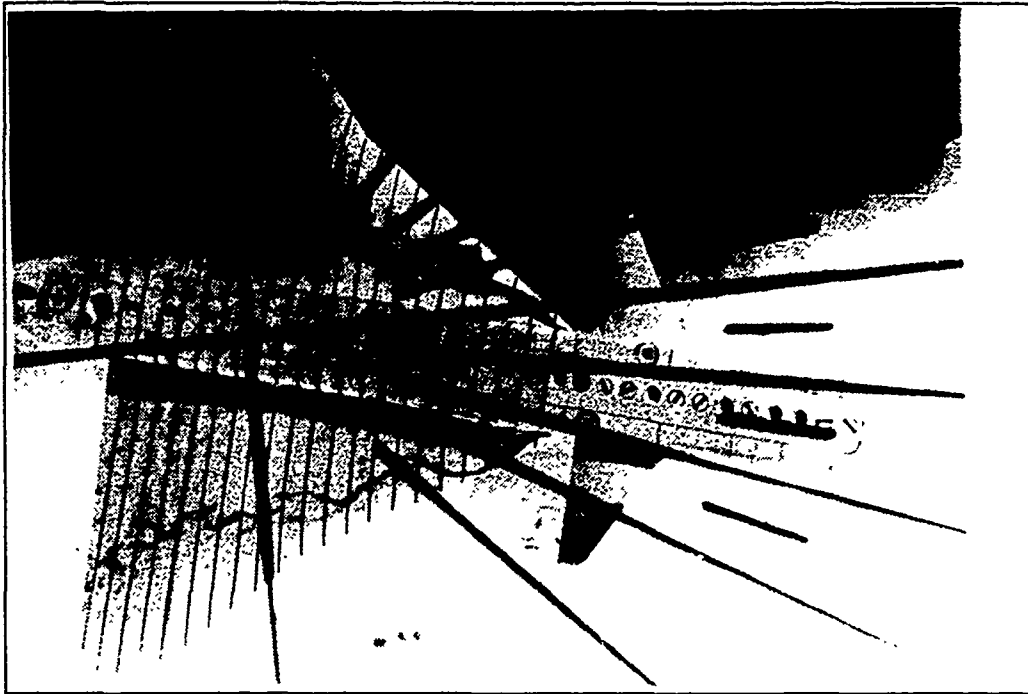


Figure 18. Wing Root Vortex Flow, Static Case,  $\alpha=20^\circ$ ,  $\beta=15^\circ$

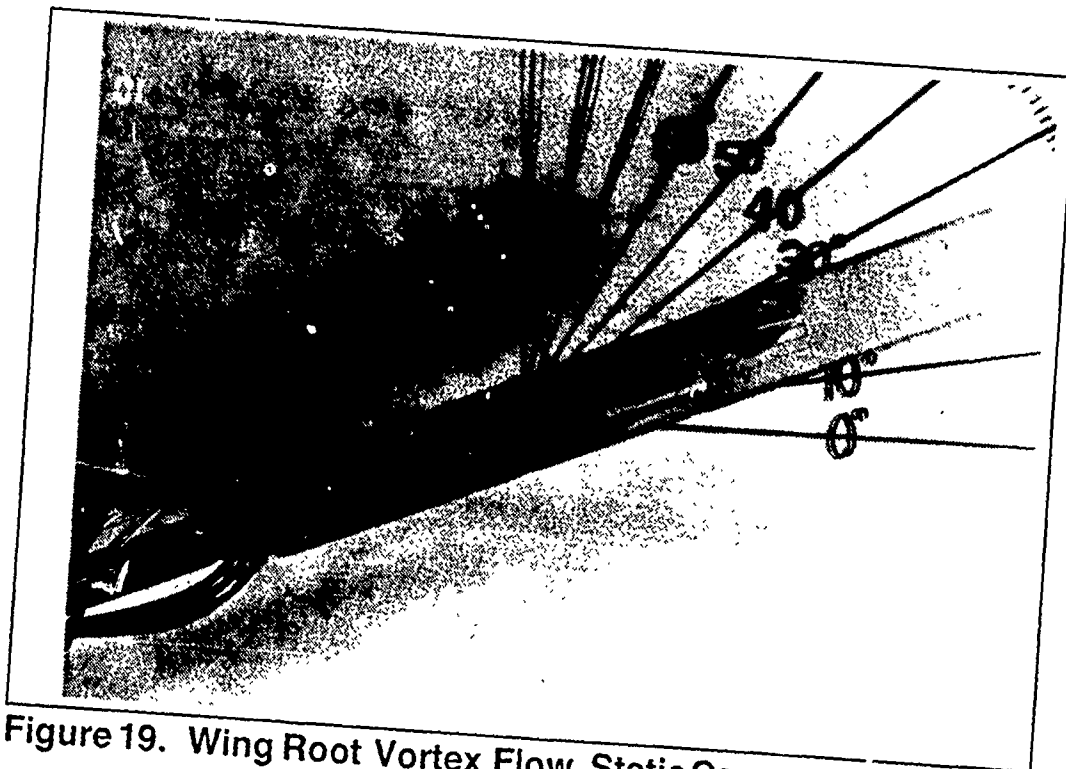
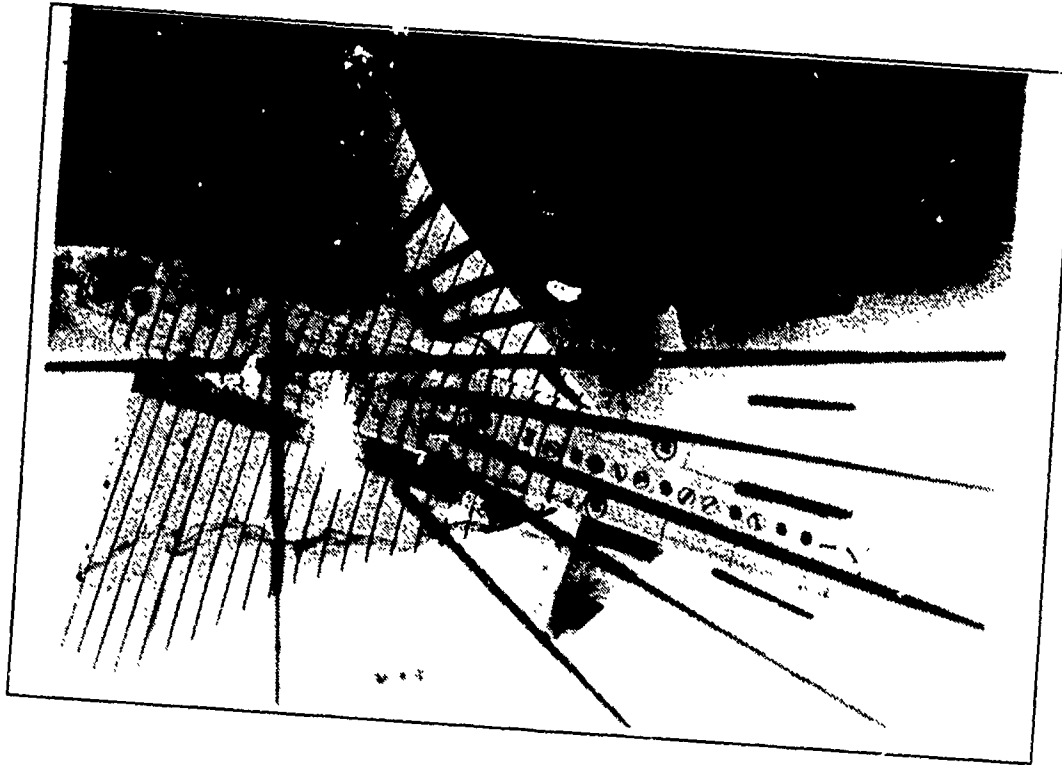


Figure 19. Wing Root Vortex Flow, Static Case,  $\alpha=20^\circ$ ,  $\beta=20^\circ$

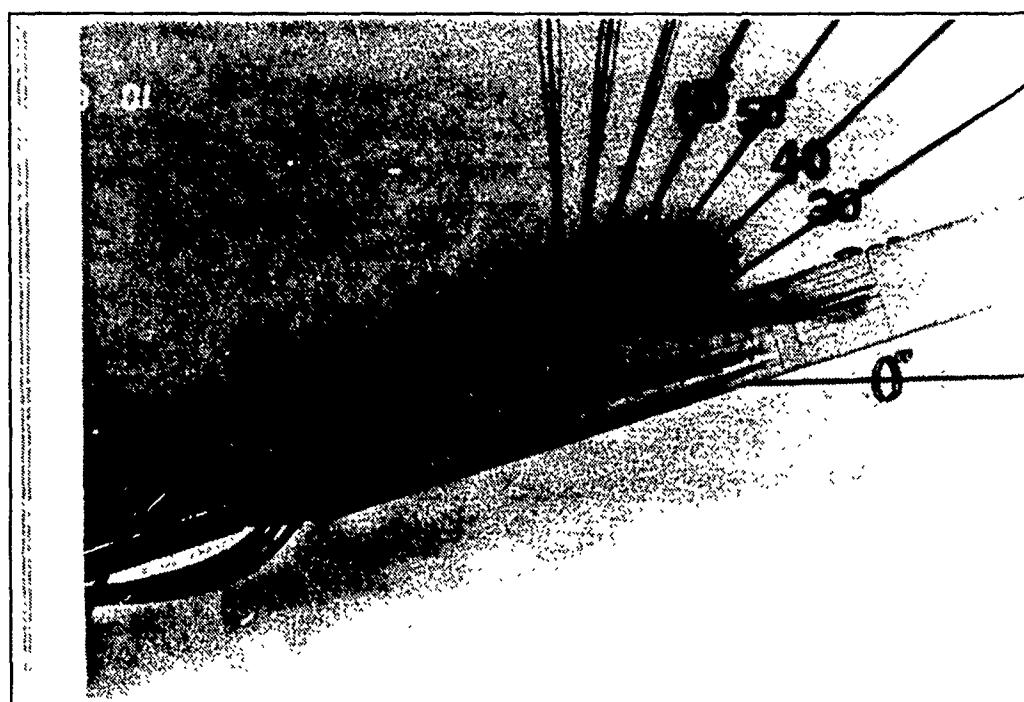
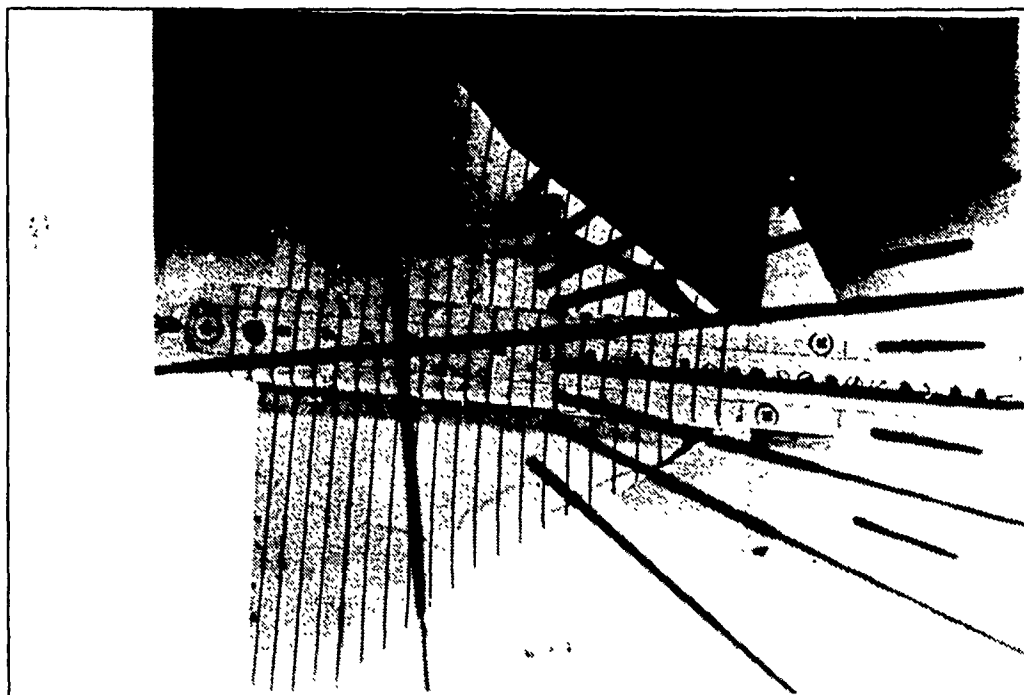


Figure 20. Wing Root Vortex Flow, Static Case,  $\alpha=15^\circ$ ,  $\beta=10^\circ$



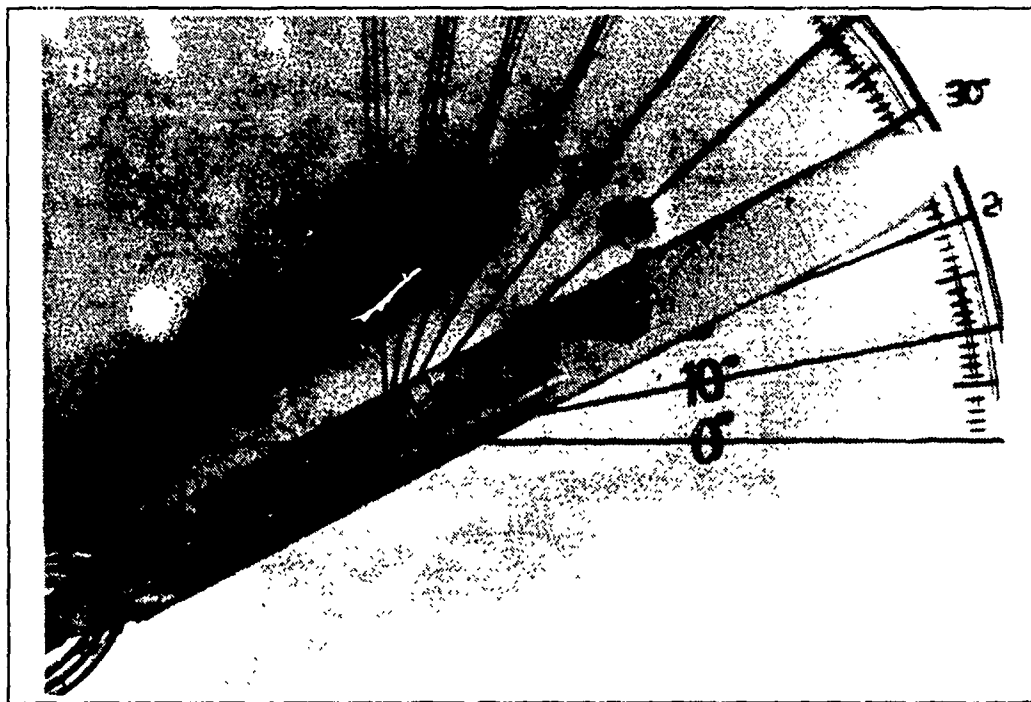
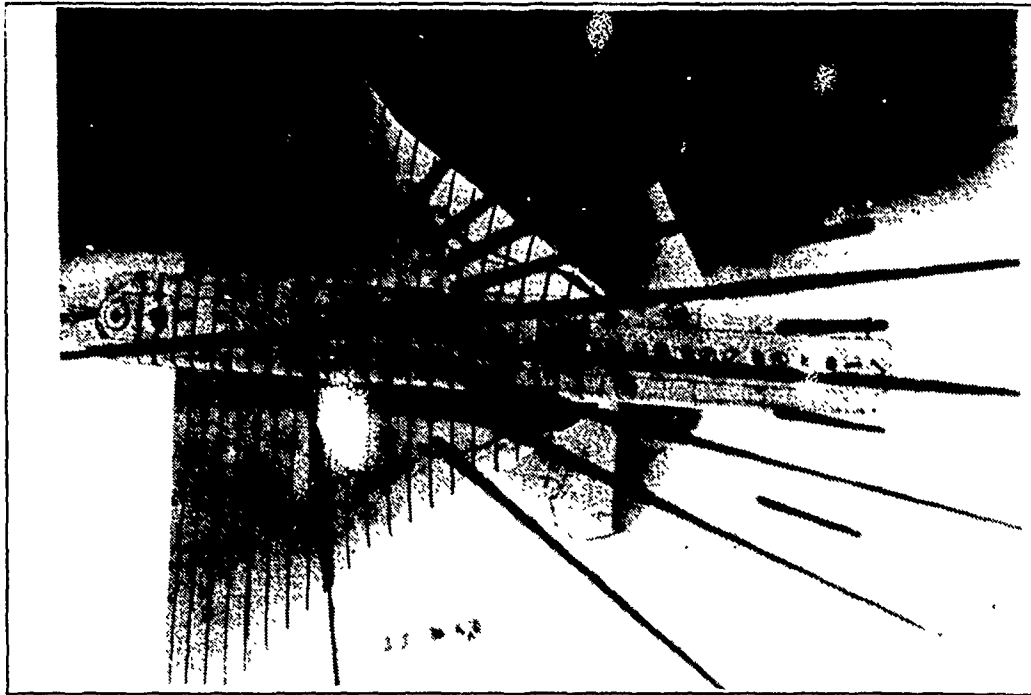


Figure 21. Wing Root Vortex Flow, Static Case,  $\alpha=25^\circ$ ,  $\beta=10^\circ$

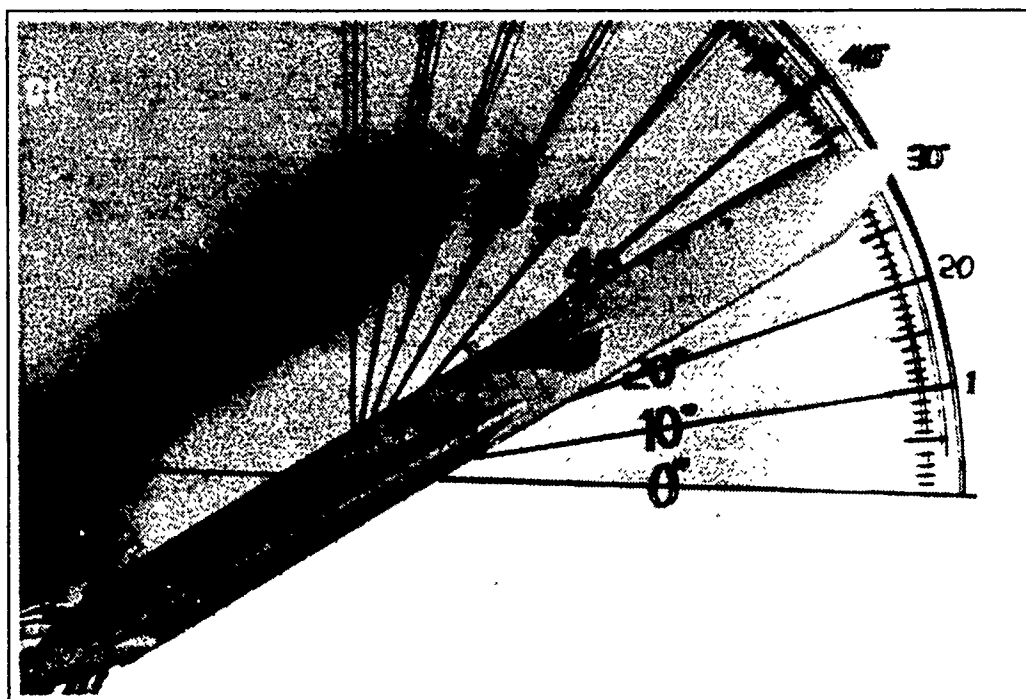
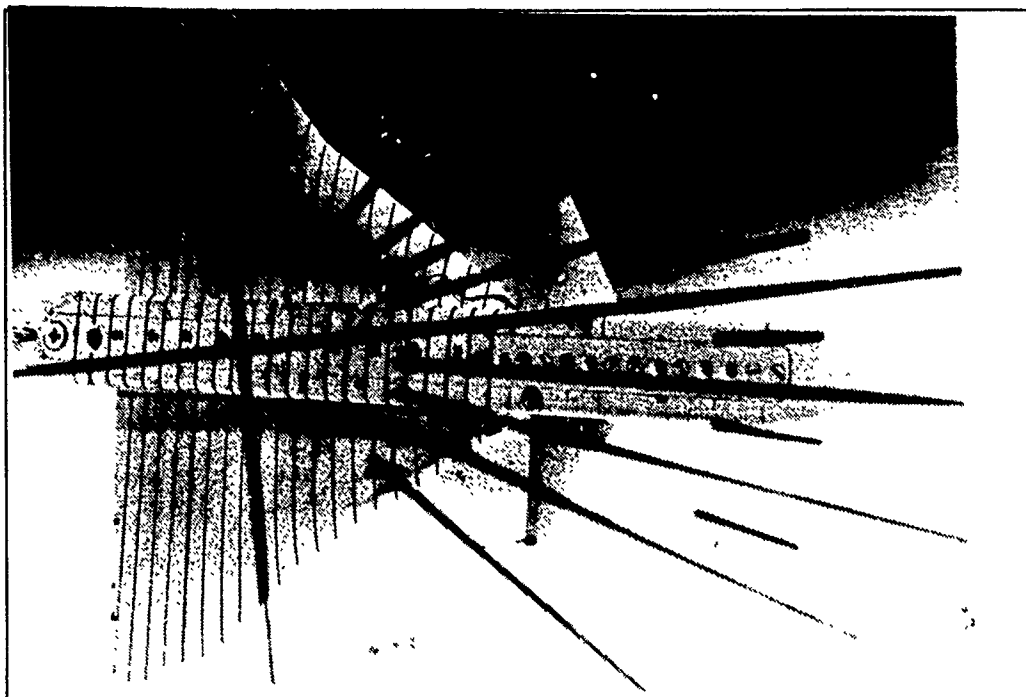


Figure 22. Wing Root Vortex Flow, Static Case,  $\alpha=30^\circ$ ,  $\beta=10^\circ$

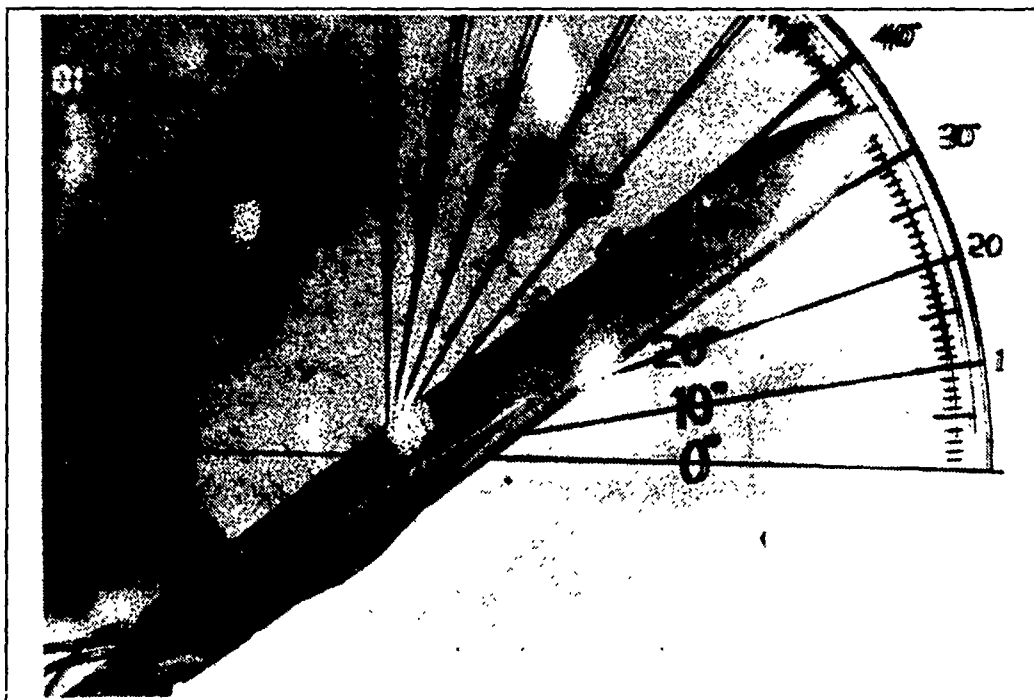
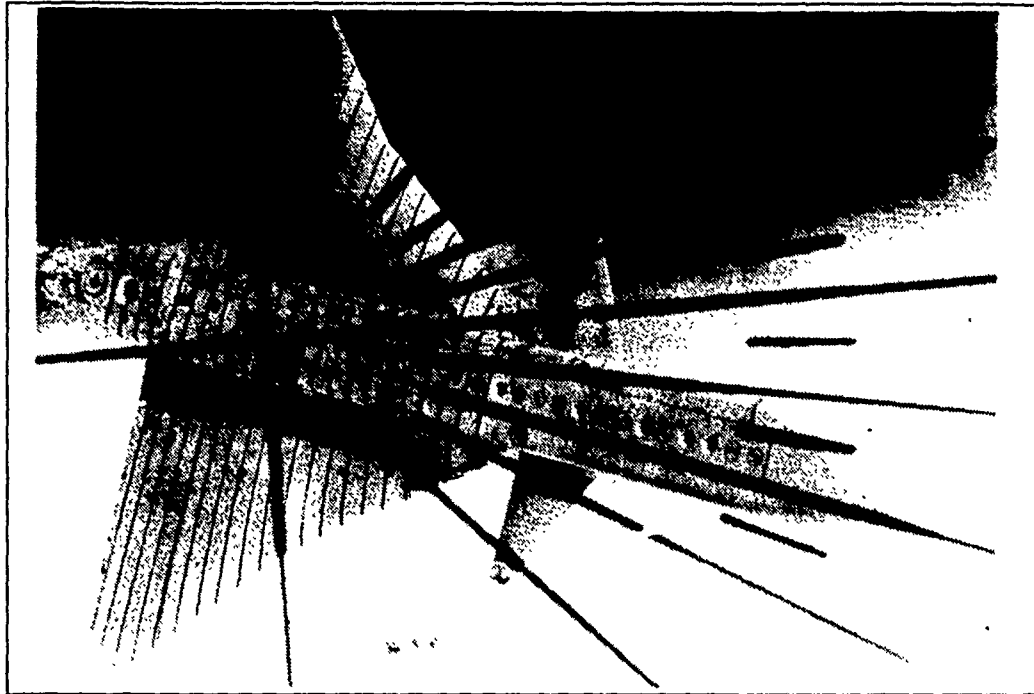


Figure 23. Wing Root Vortex Flow, Static Case,  $\alpha=35^\circ$ ,  $\beta=20^\circ$

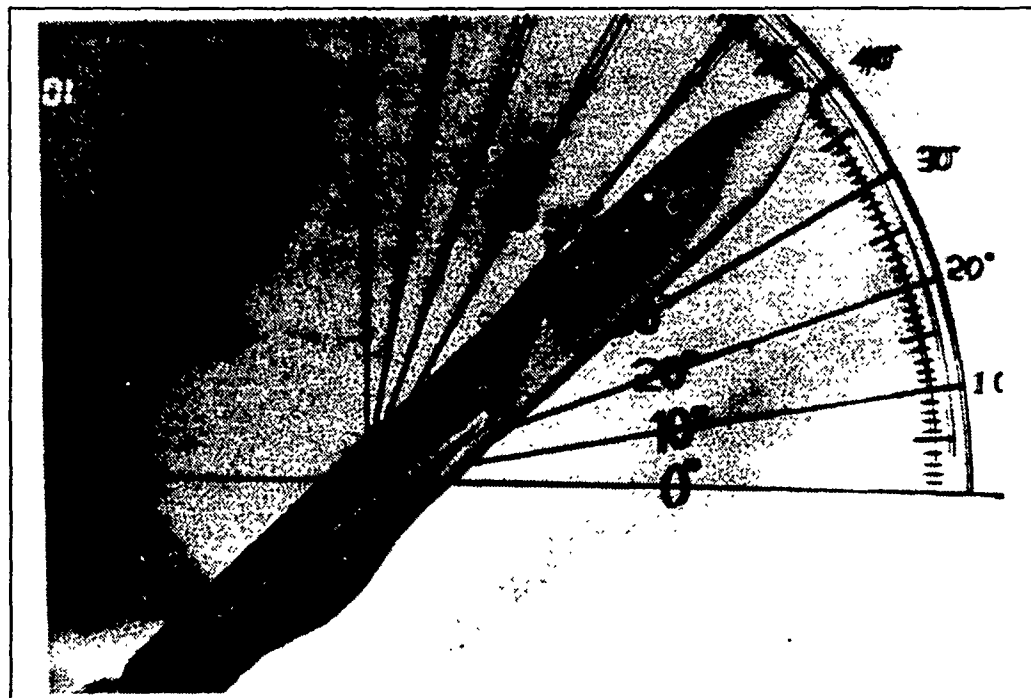
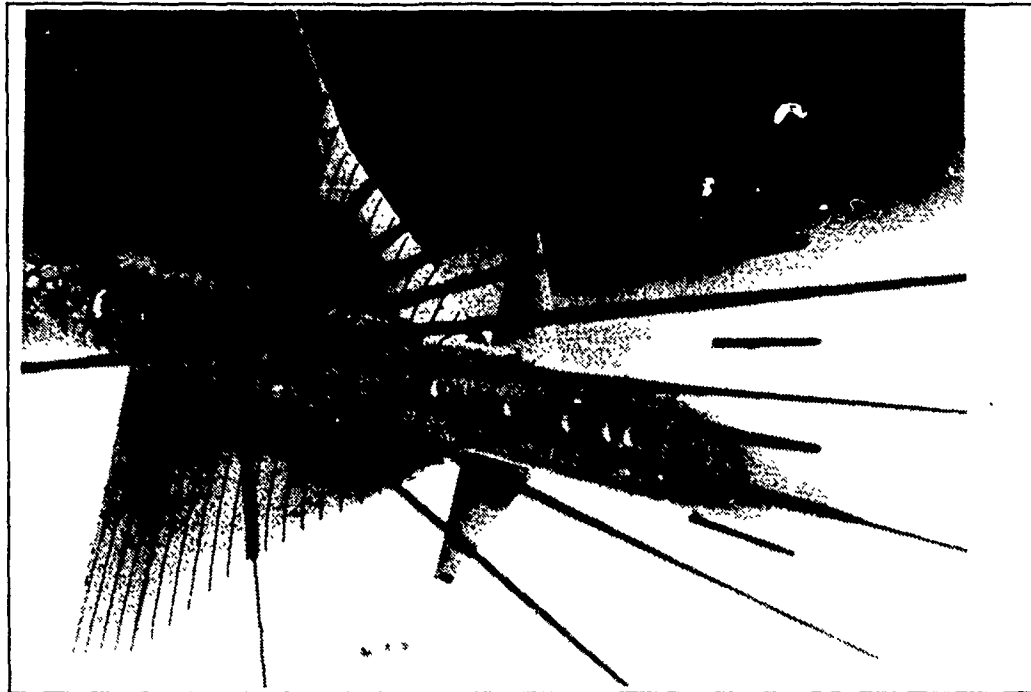


Figure 24. Wing Root Vortex Flow, Static Case,  $\alpha=40^\circ$ ,  $\beta=20^\circ$

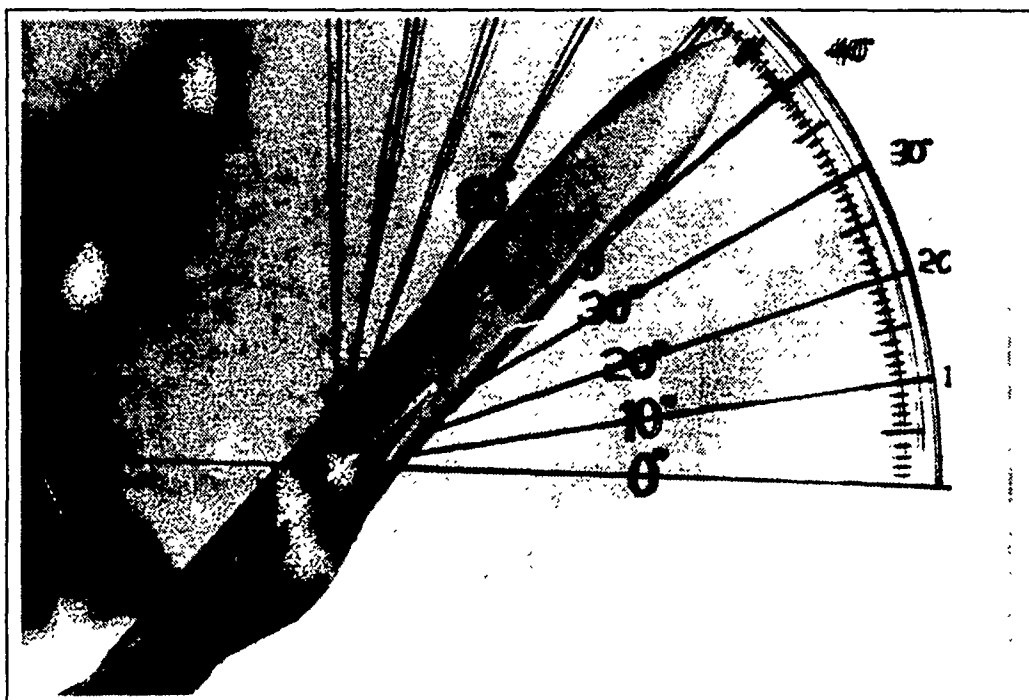
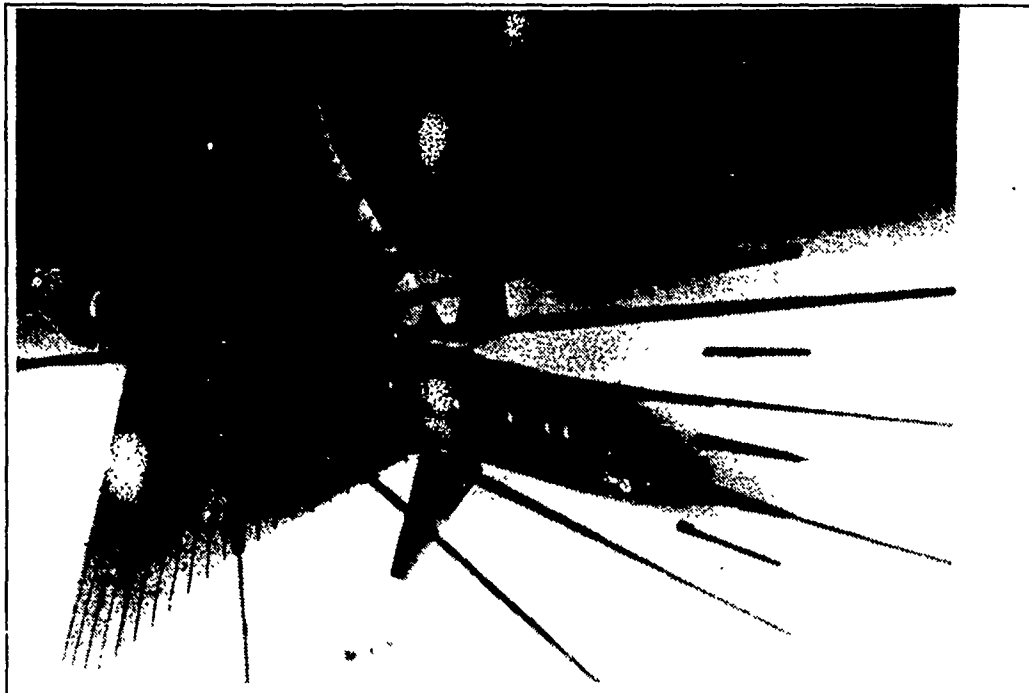


Figure 25. Wing Root Vortex Flow, Static Case,  $\alpha=45^\circ$ ,  $\beta=20^\circ$

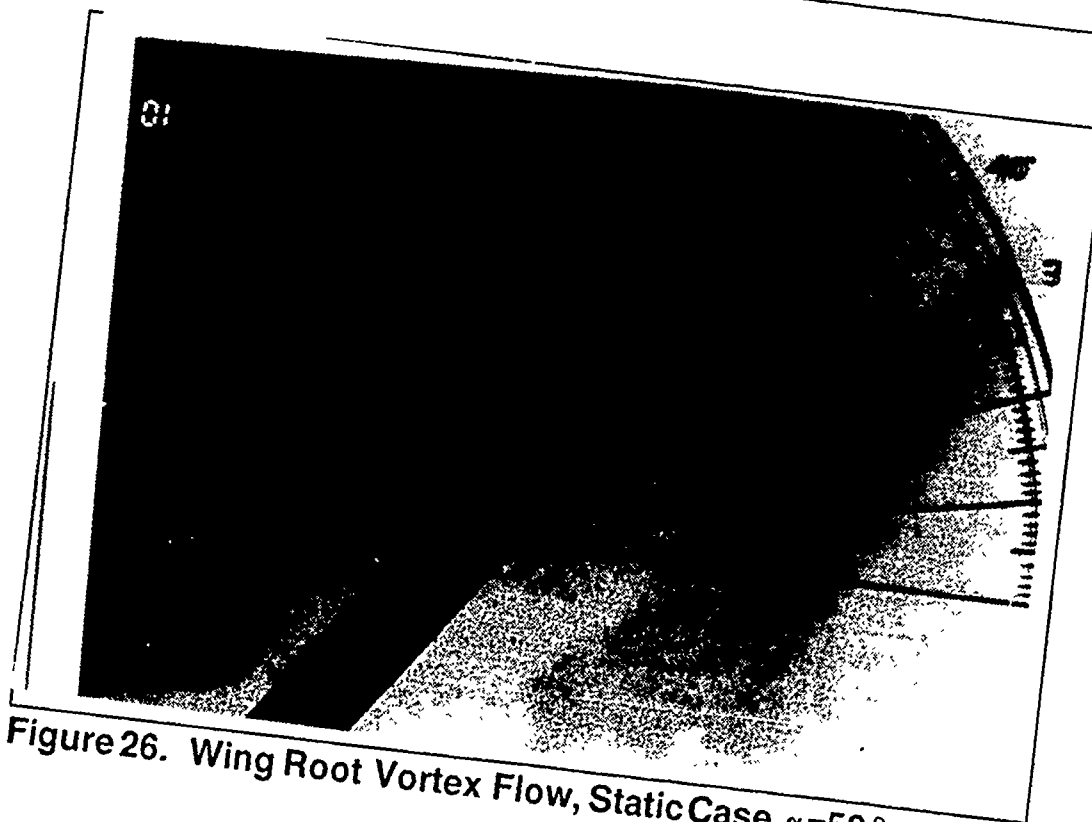
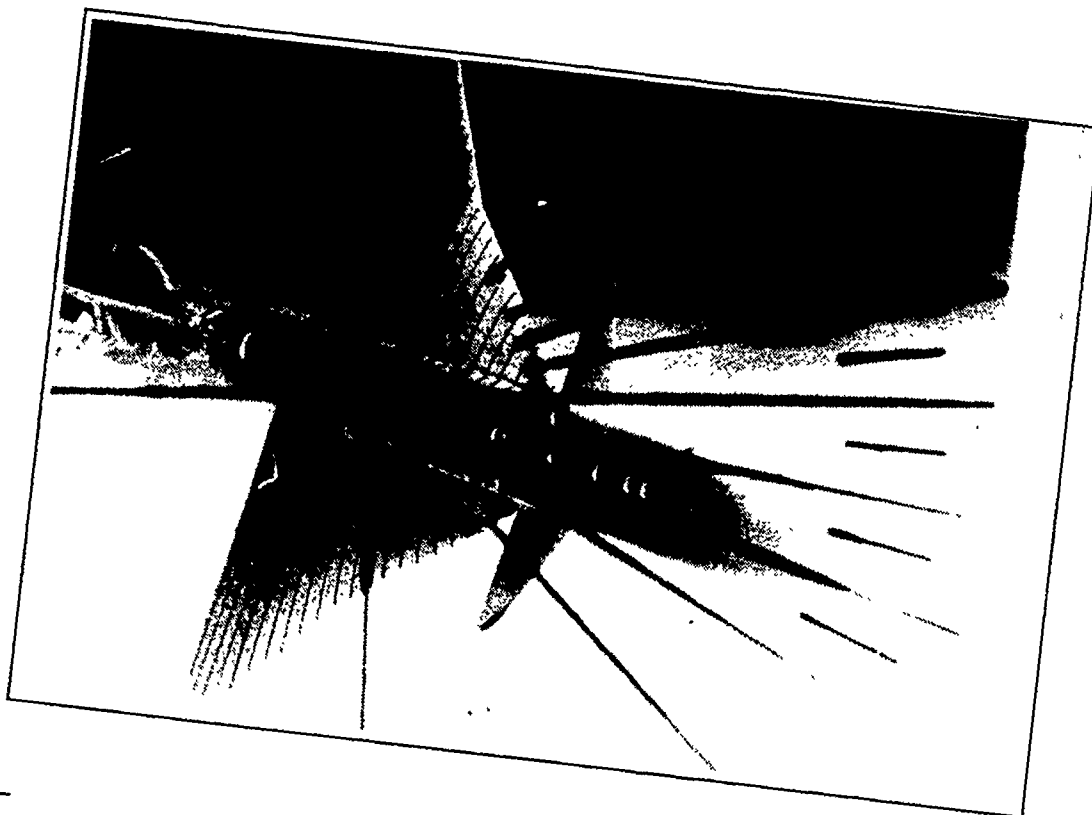


Figure 26. Wing Root Vortex Flow, Static Case,  $\alpha=50^\circ$ ,  $\beta=20^\circ$

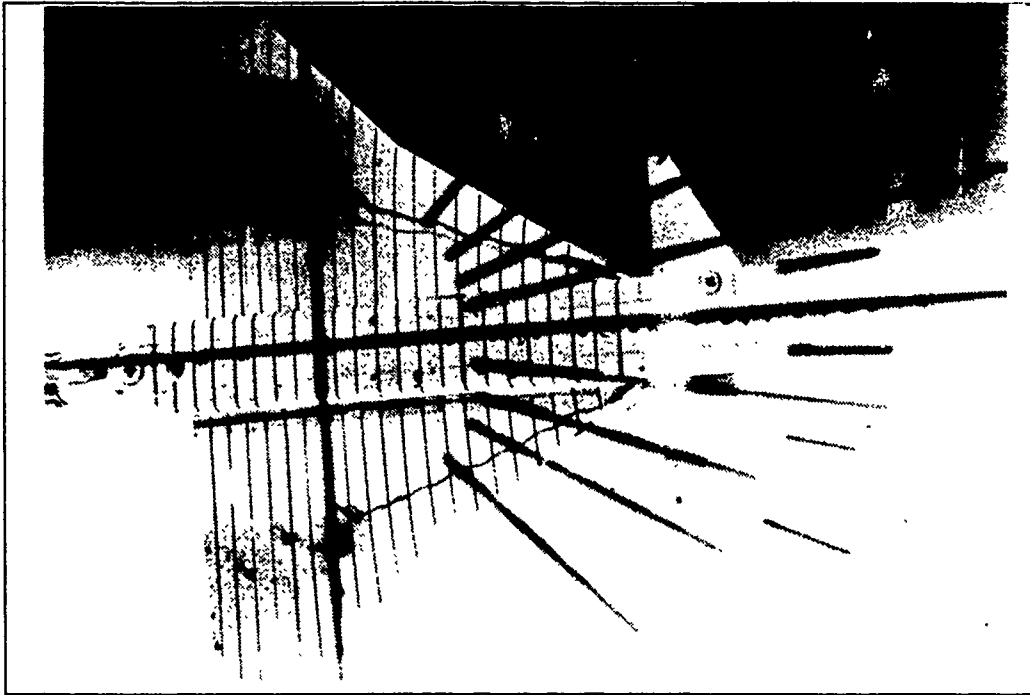


Figure 27. Wing Root Vortex Flow, Positive Sideslipping ( $k=0.08$ ),  $\alpha=20^\circ$ ,  $\beta=0^\circ$  (Same as Static Case, Fig. 15)

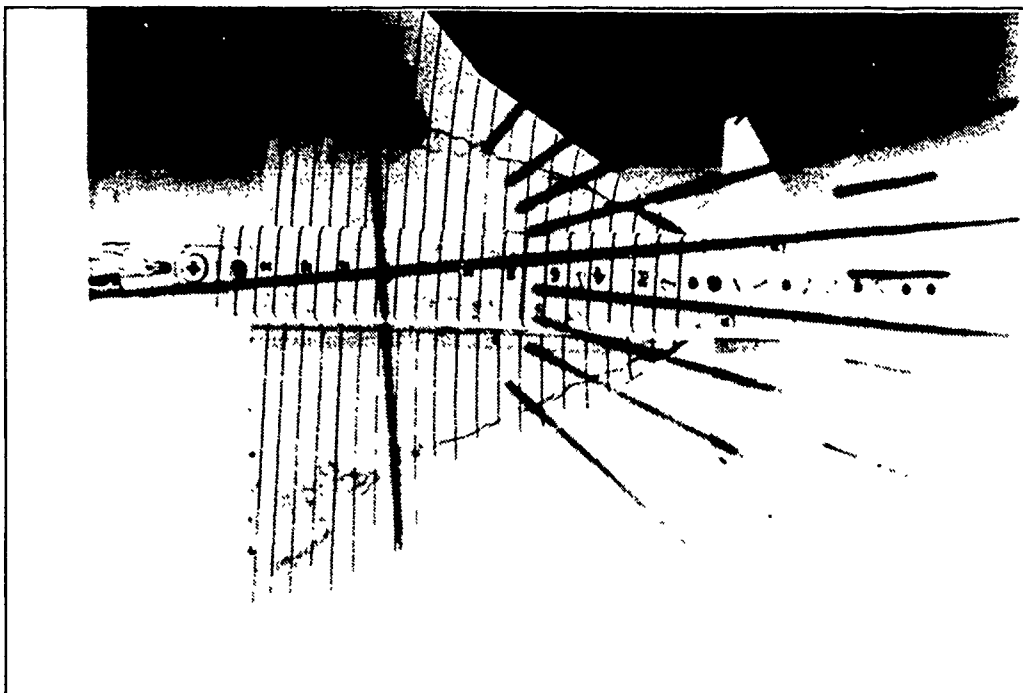


Figure 28. Wing Root Vortex Flow, Positive Sideslipping ( $k=0.08$ ),  $\alpha=20^\circ$ ,  $\beta=5^\circ$



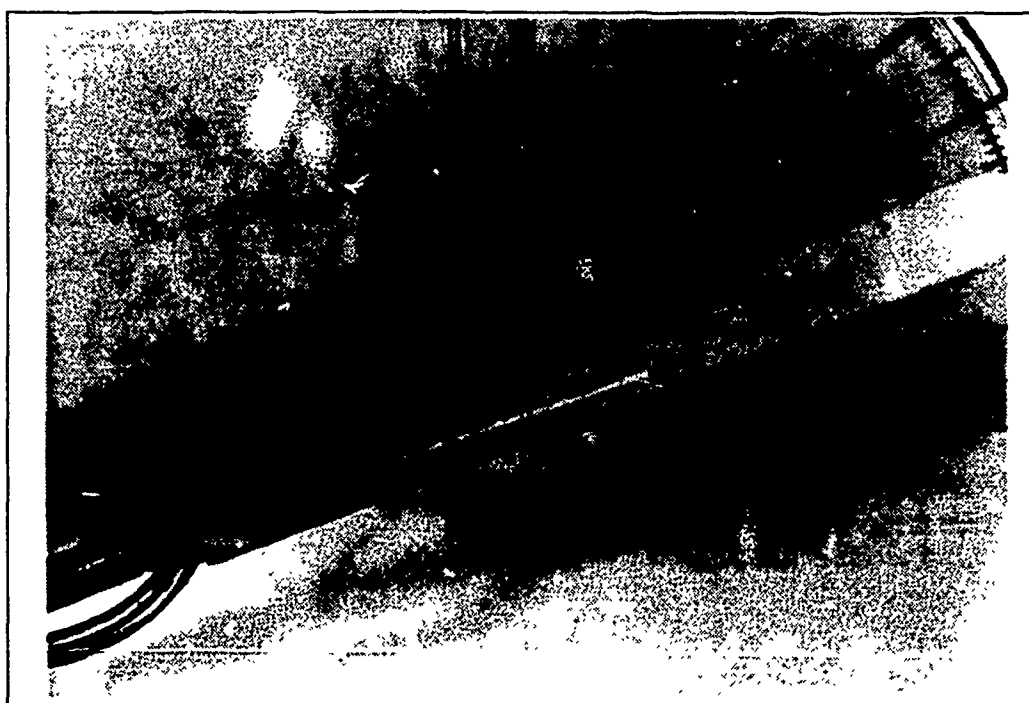
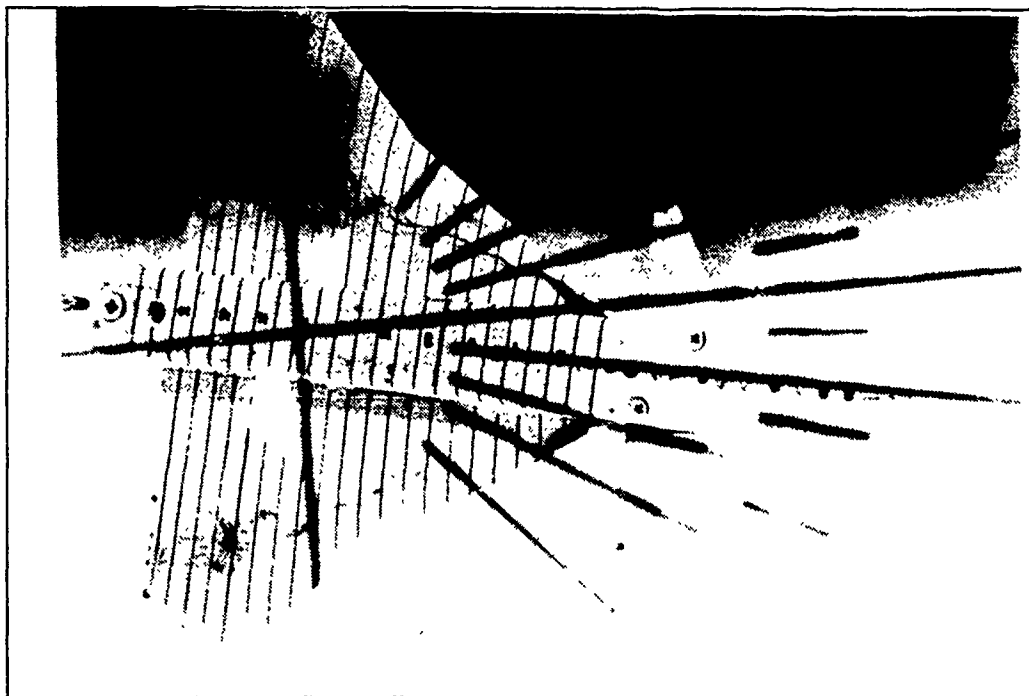


Figure 29. Wing Root Vortex Flow, Positive Sideslipping  
 $(k=0.08)$ ,  $\alpha=20^\circ$ ,  $\beta=10^\circ$

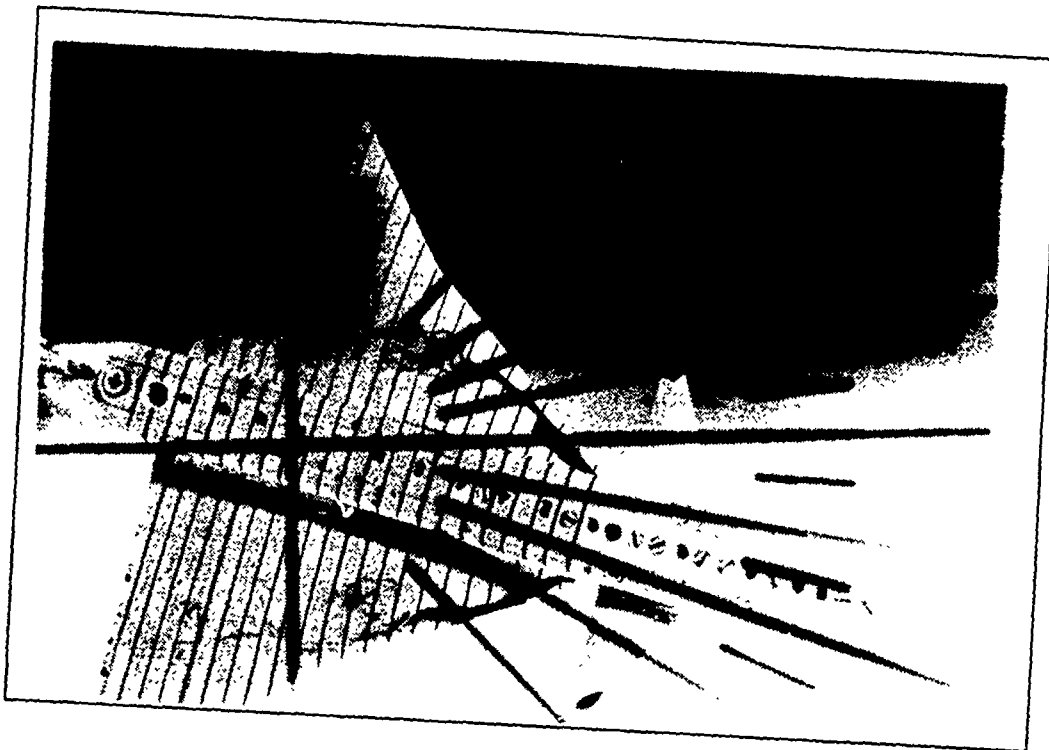


Figure 30. Wing Root Vortex Flow, Positive Sideslipping  
( $k=0.08$ ),  $\alpha=20^\circ$ ,  $\beta=15^\circ$

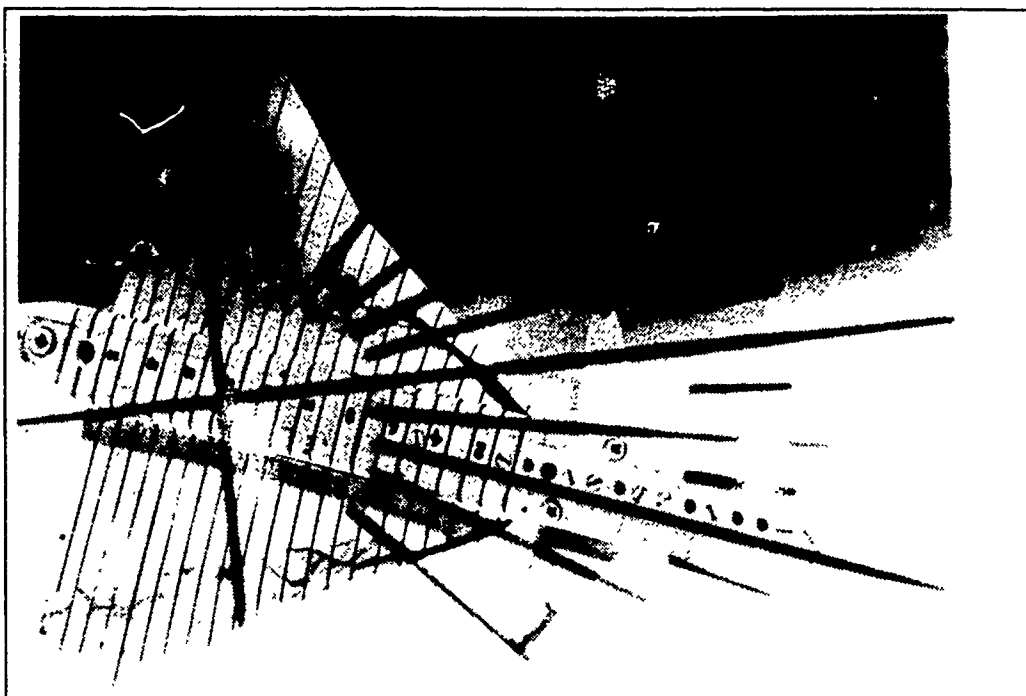


Figure 31. Wing Root Vortex Flow, Positive Sideslipping  
 $(k=0.08)$ ,  $\alpha=20^\circ$ ,  $\beta=20^\circ$

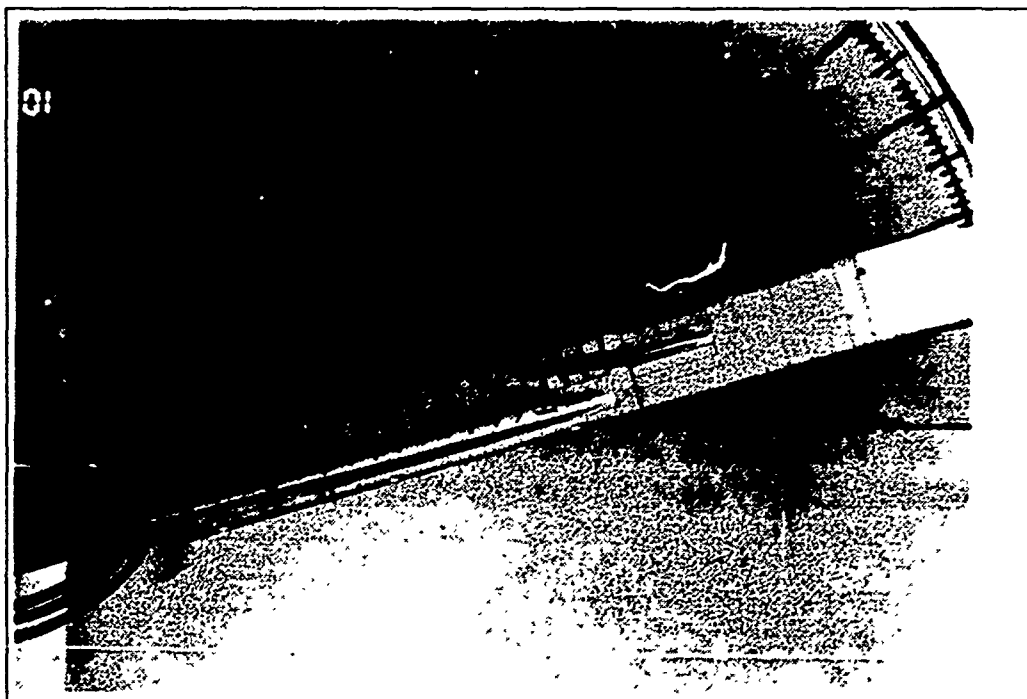
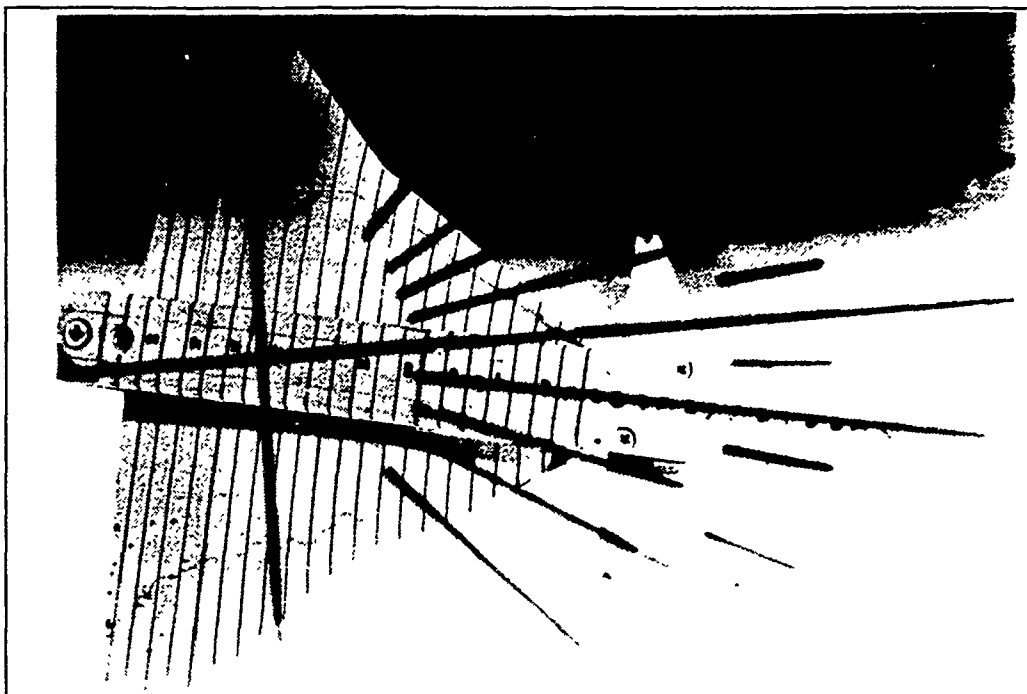


Figure 32. Wing Root Vortex Flow, Positive Sideslipping  
( $k=0.08$ ),  $\alpha=15^\circ$ ,  $\beta=10^\circ$

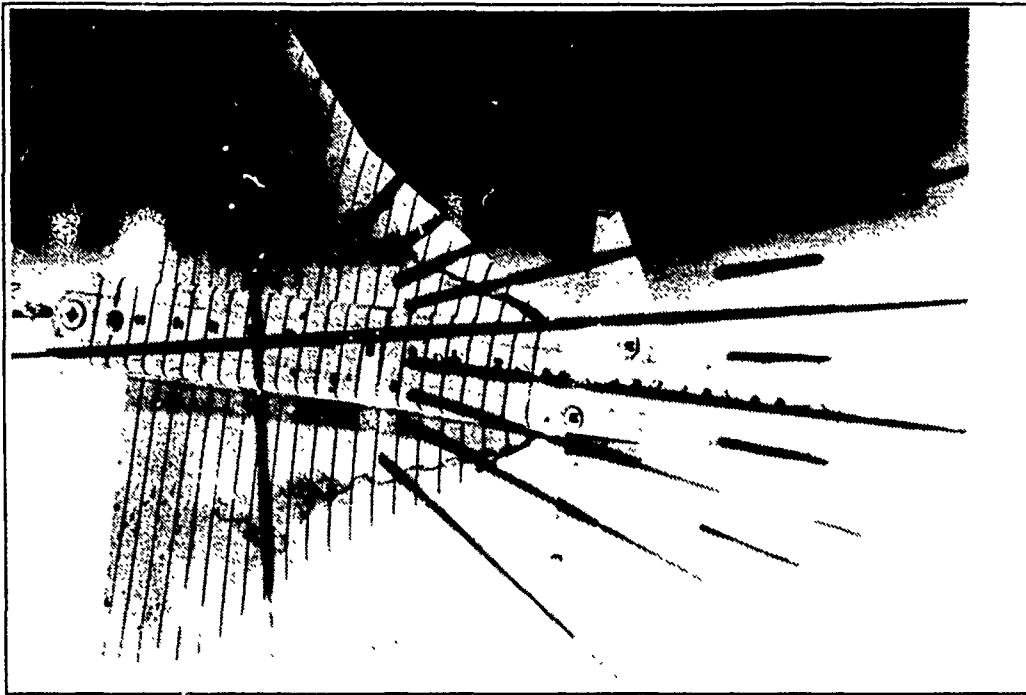


Figure 33. Wing Root Vortex Flow, Positive Sideslipping  
( $k=0.08$ ),  $\alpha=25^\circ$ ,  $\beta=10^\circ$

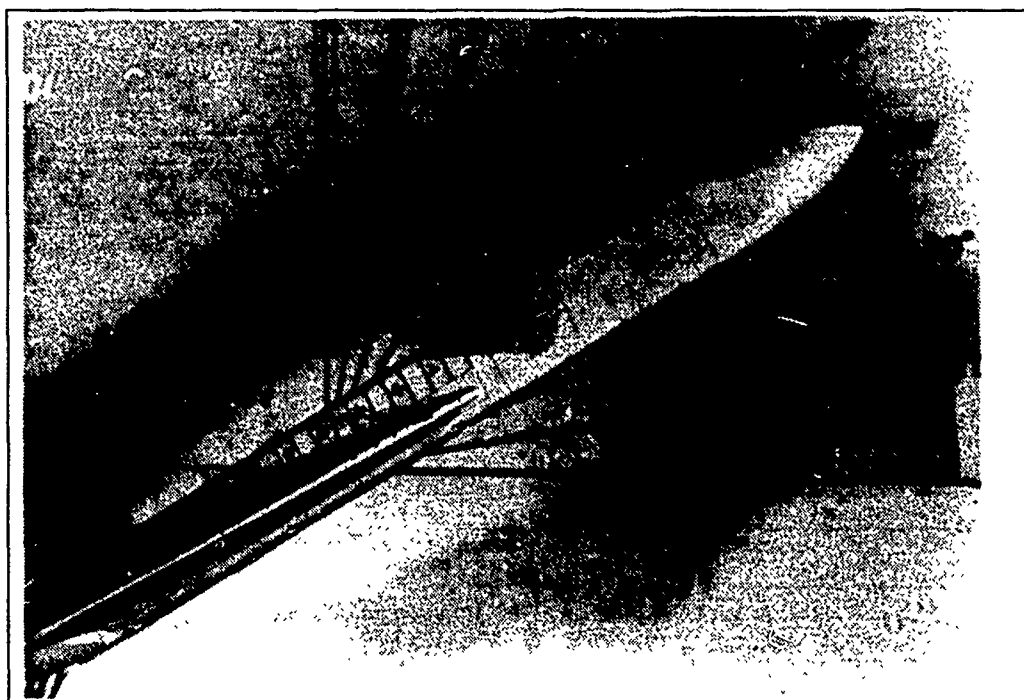
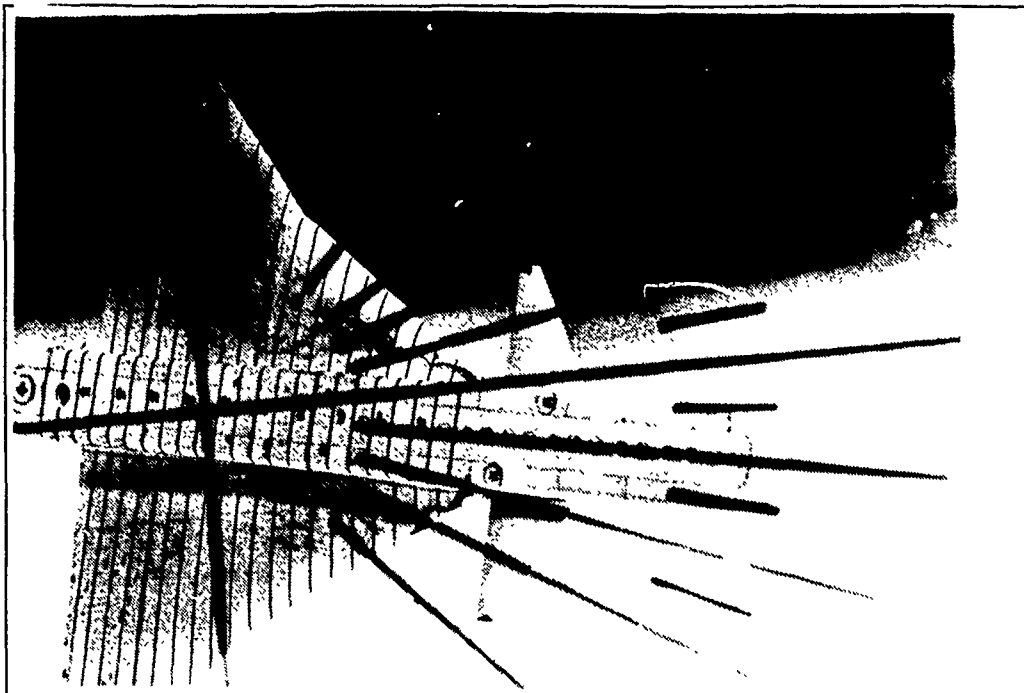


Figure 34. Wing Root Vortex Flow, Positive Sideslipping  
 $(k=0.08)$ ,  $\alpha=30^\circ$ ,  $\beta=10^\circ$

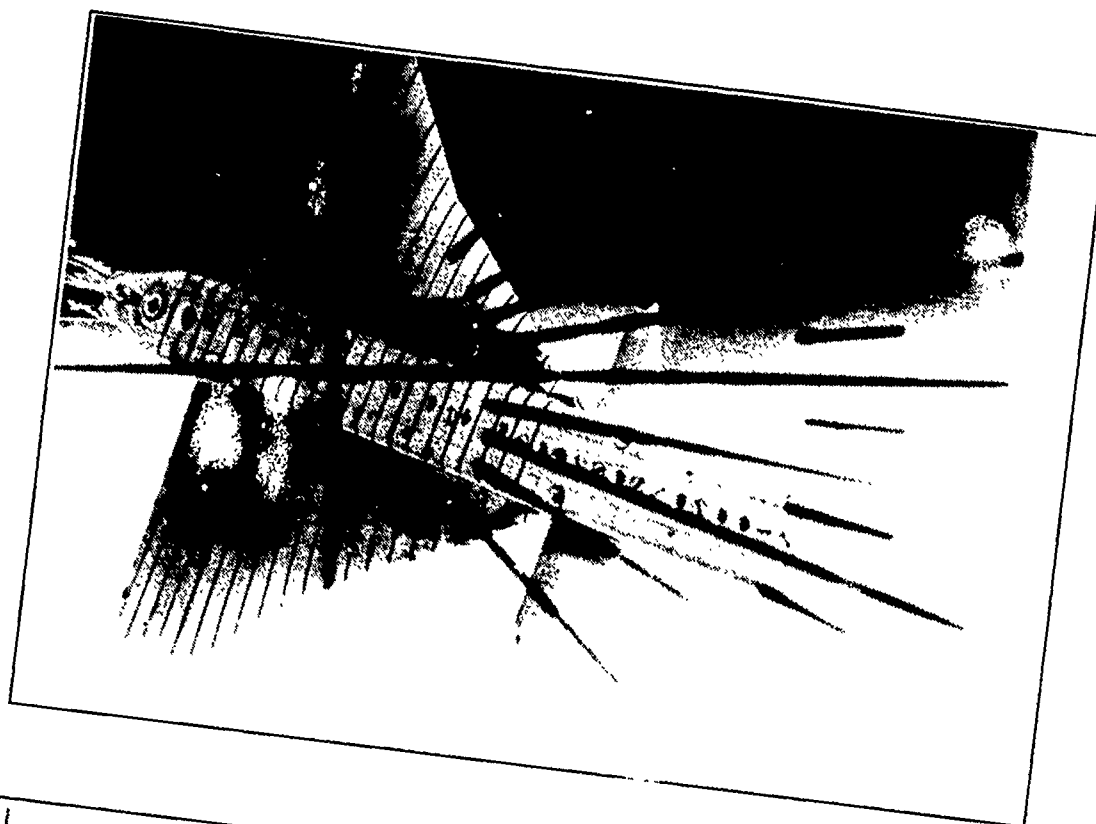


Figure 35. Wing Root Vortex Flow, Positive Sideslipping  
 $(k=0.08)$ ,  $\alpha=35^\circ$ ,  $\beta=20^\circ$

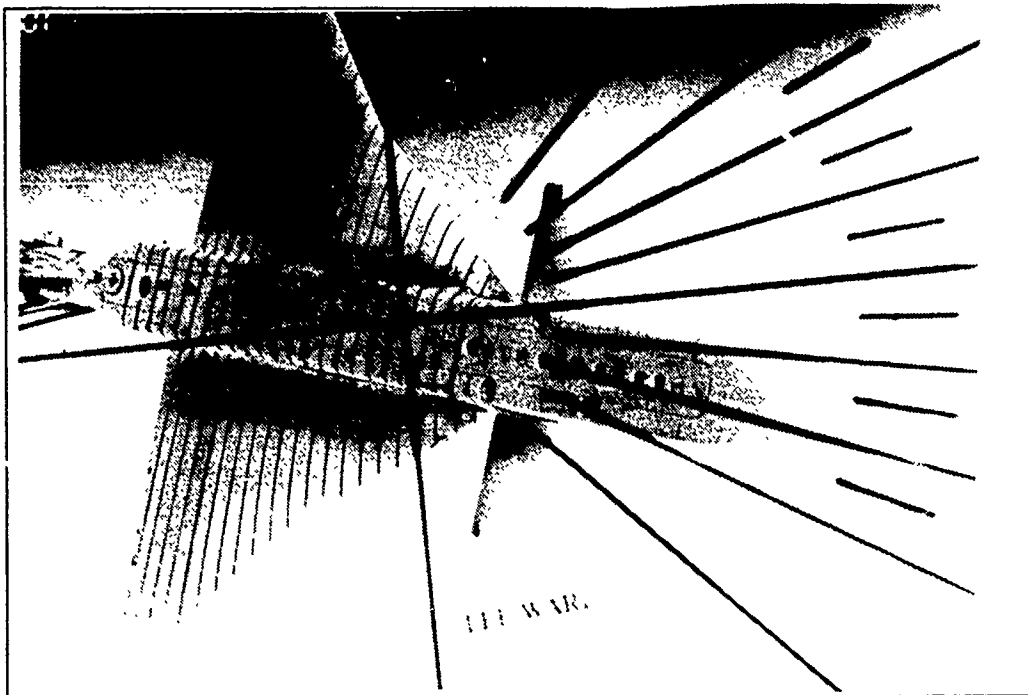


Figure 36. Wing Root Vortex Flow, Positive Sideslipping  
( $\lambda=0.08$ ),  $\alpha=45^\circ$ ,  $\beta=20^\circ$



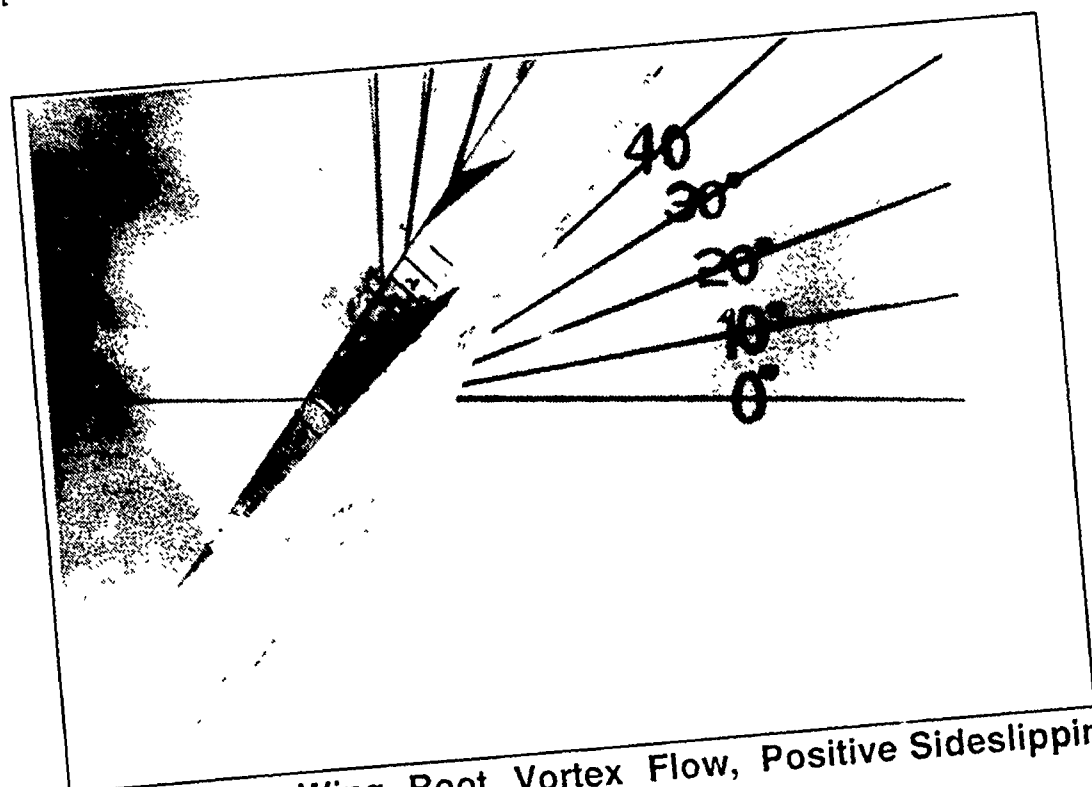
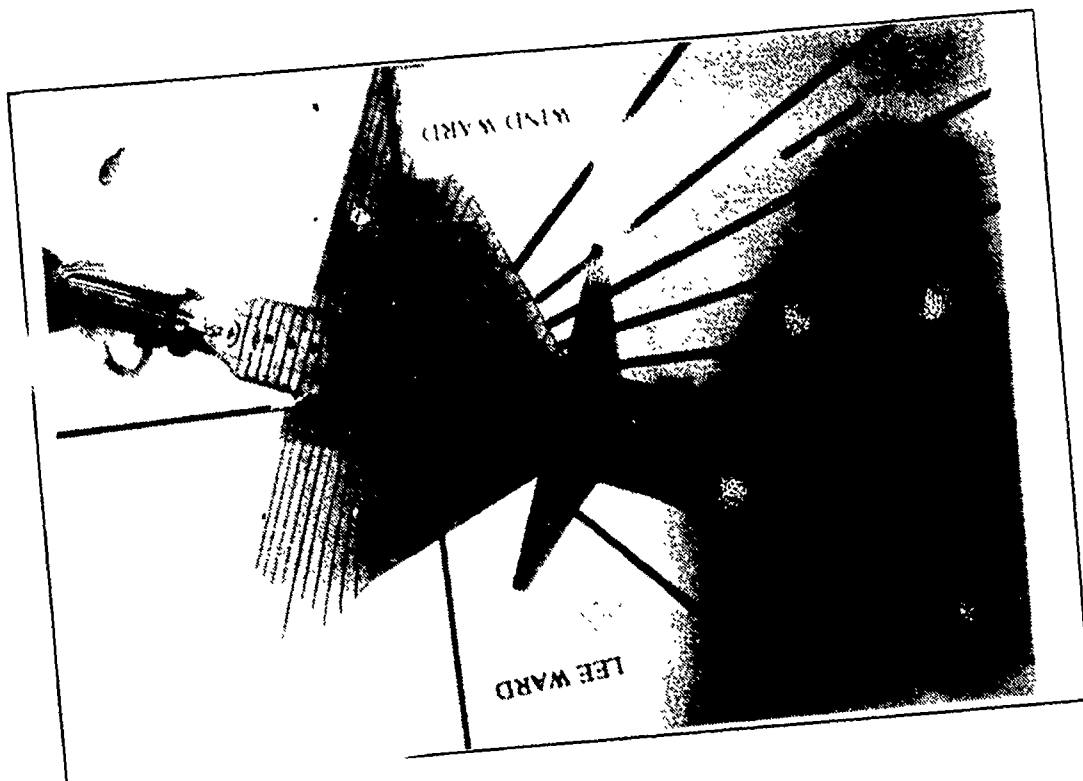


Figure 37. Wing Root Vortex Flow, Positive Sideslipping  
 $(k=0.08)$ ,  $\alpha=50^\circ$ ,  $\beta=20^\circ$

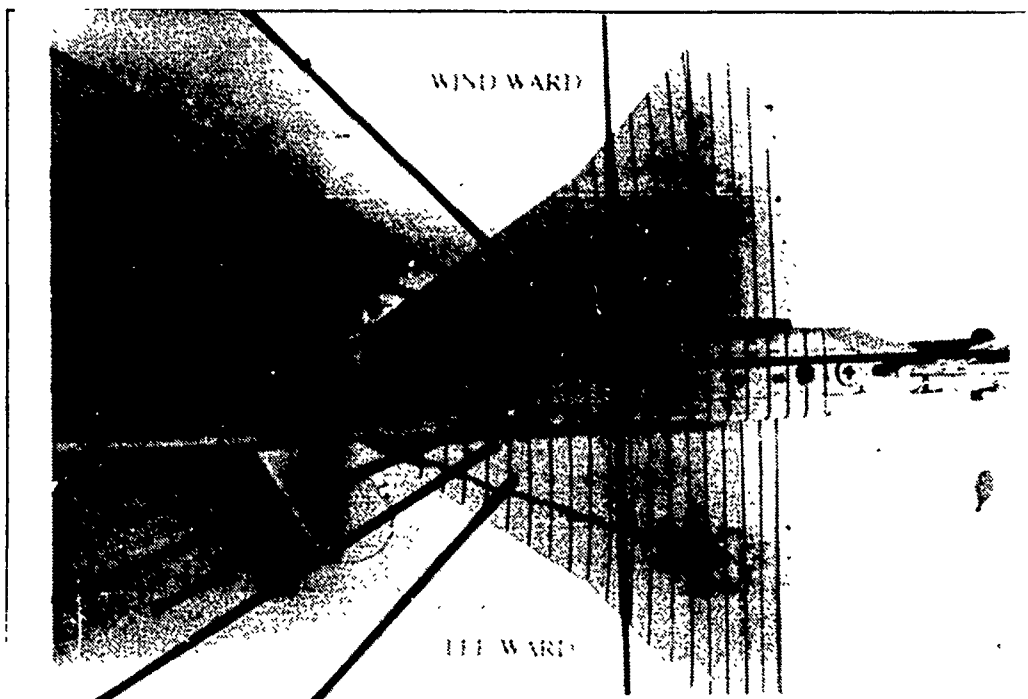


Figure 38. Wing Root Vortex Flow, Positive Sideslipping ( $k=0.05$ ),  $\alpha=20^\circ$ ,  $\beta=0^\circ$  (Same as Static Case Fig. 15)

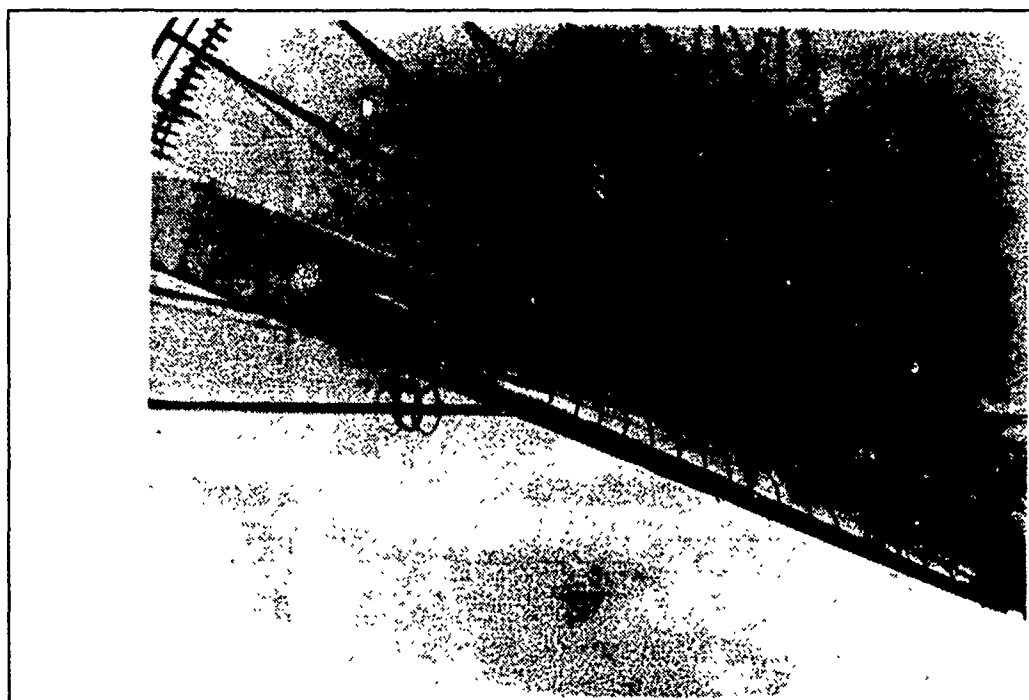
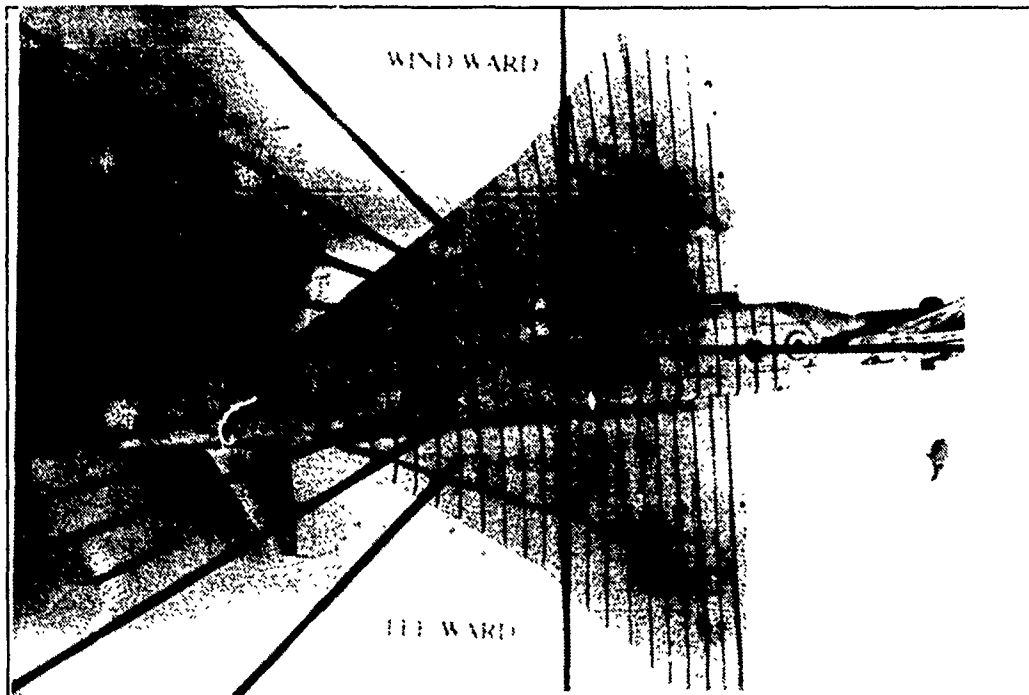


Figure 39. Wing Root Vortex Flow, Positive Sideslipping ( $k=0.05$ ),  $\alpha=15^\circ$ ,  $\beta=5^\circ$

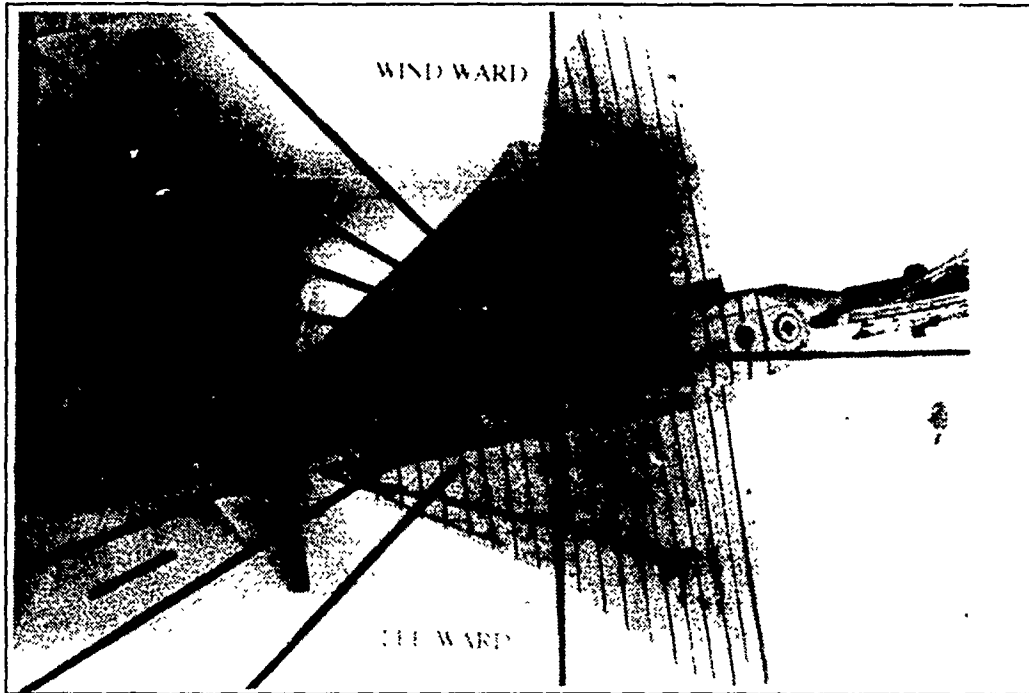


Figure 40. Wing Root Vortex Flow, Positive Sideslipping ( $k=0.05$ ),  $\alpha=20^\circ$ ,  $\beta=10^\circ$

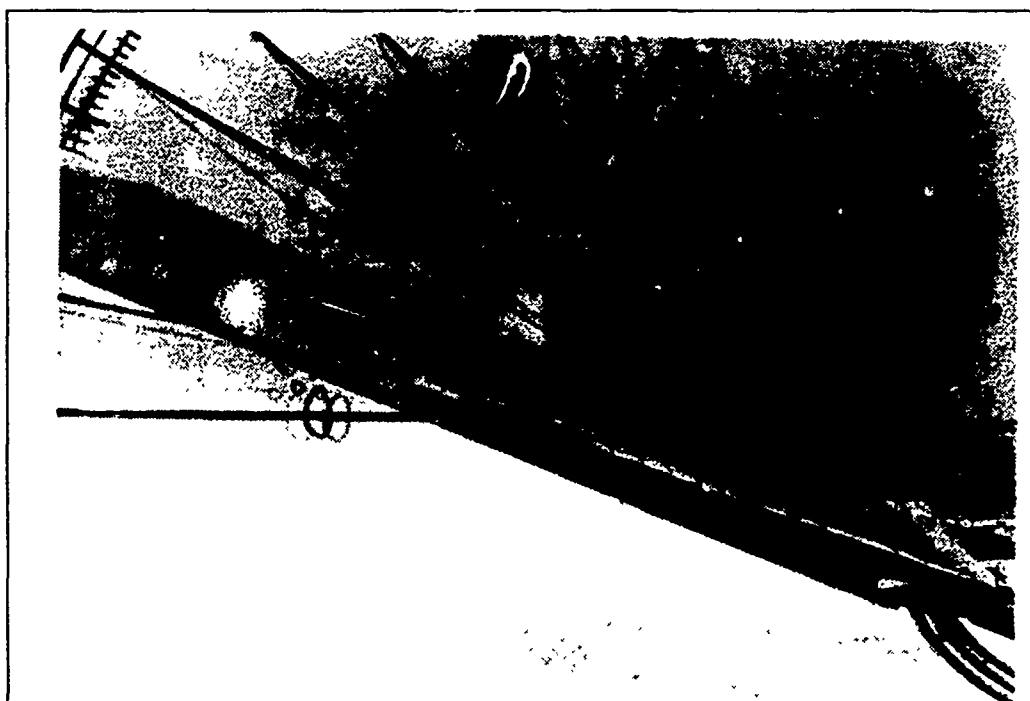
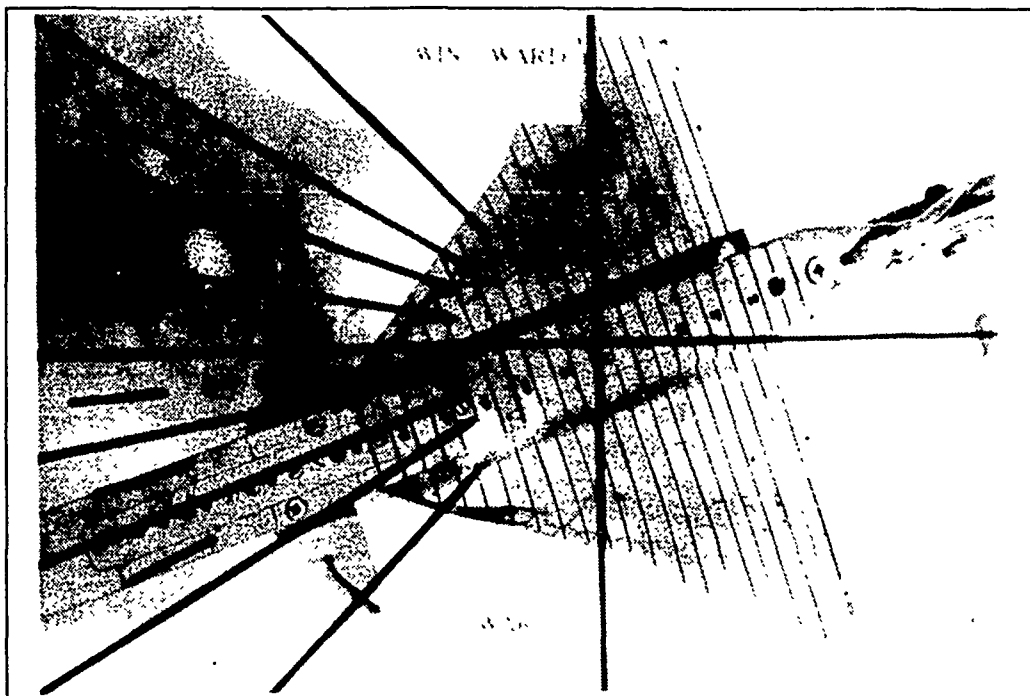


Figure 41. Wing Root Vortex Flow, Positive Sideslipping  
( $k=0.05$ ),  $\alpha=20^\circ$ ,  $\beta=20^\circ$

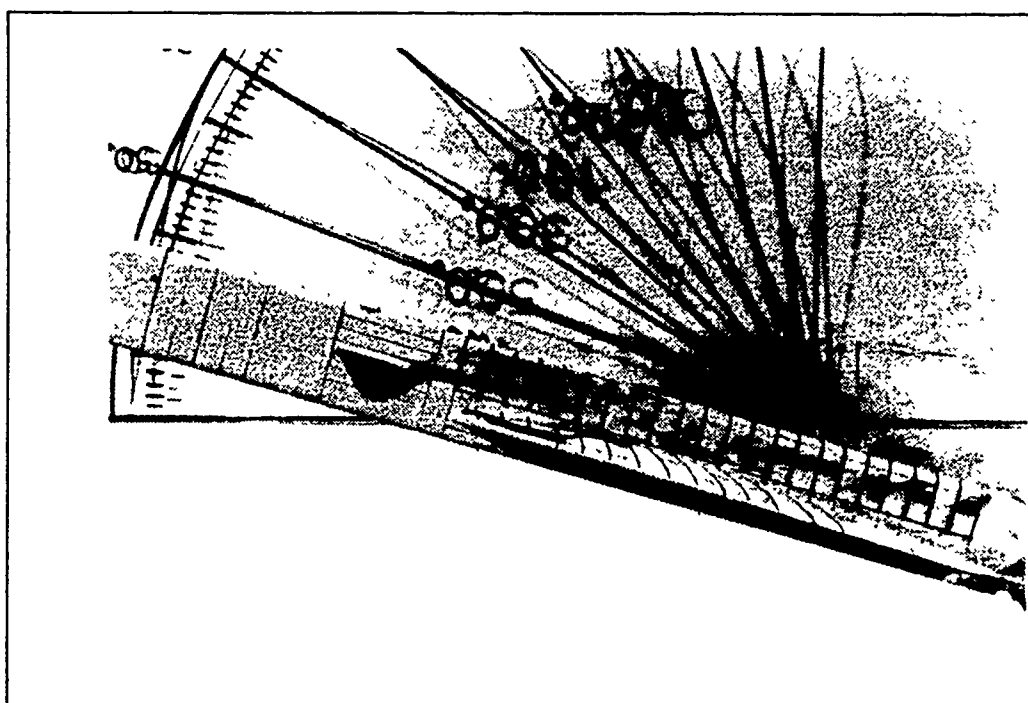
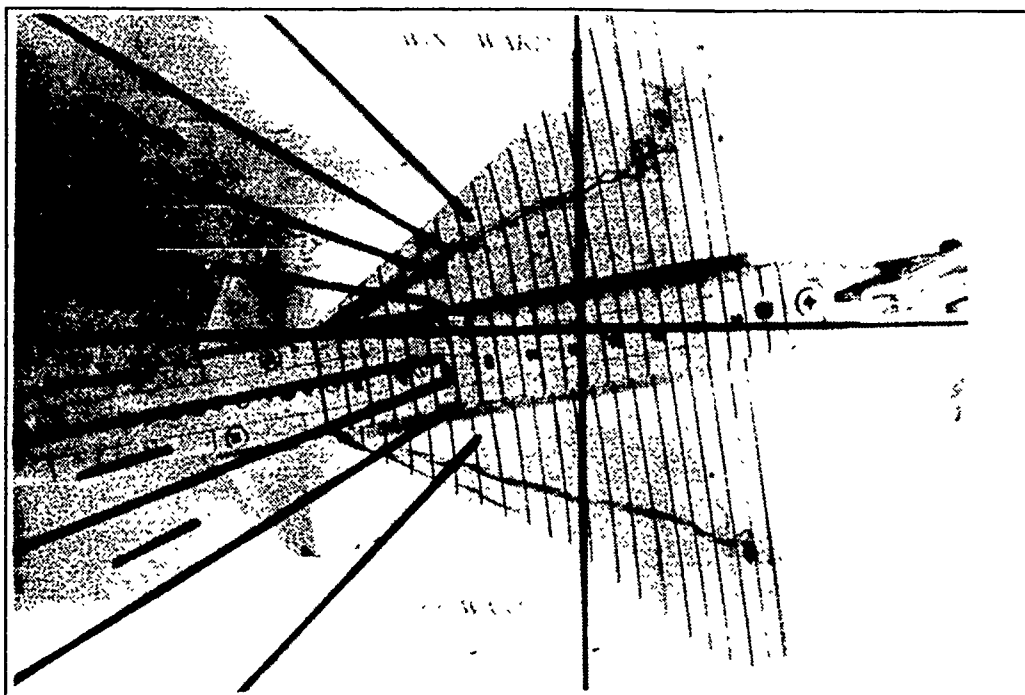


Figure 42. Wing Root Vortex Flow, Positive Sideslipping  
 $(k=0.05)$ ,  $\alpha=15^\circ$ ,  $\beta=10^\circ$

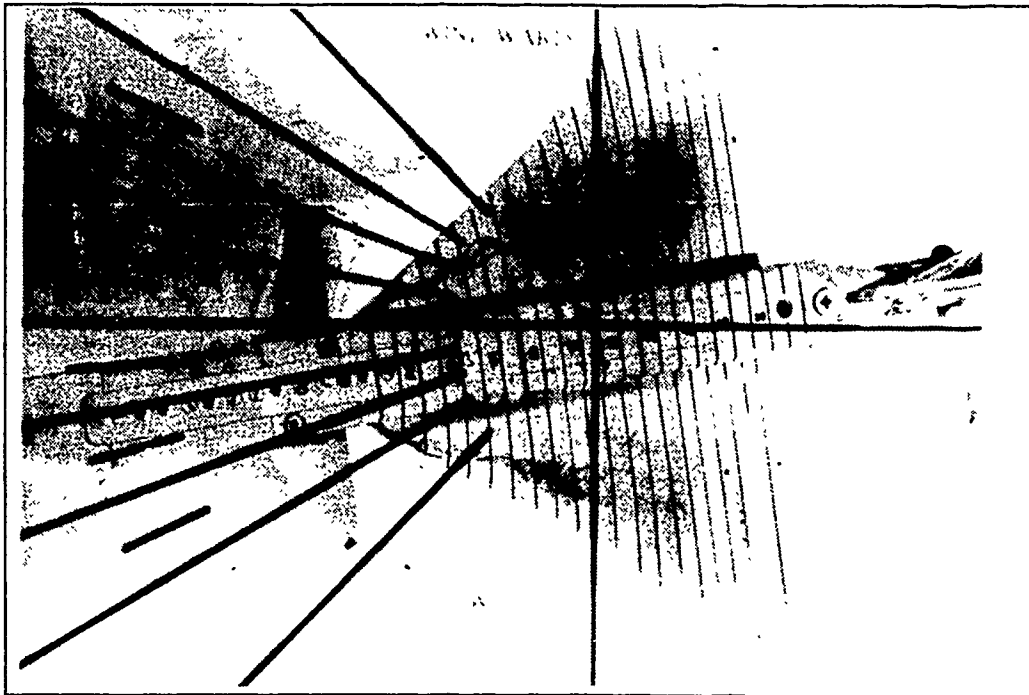


Figure 43. Wing Root Vortex Flow, Positive Sideslipping  
 ( $k=0.05$ ),  $\alpha=25^\circ$ ,  $\beta=10^\circ$

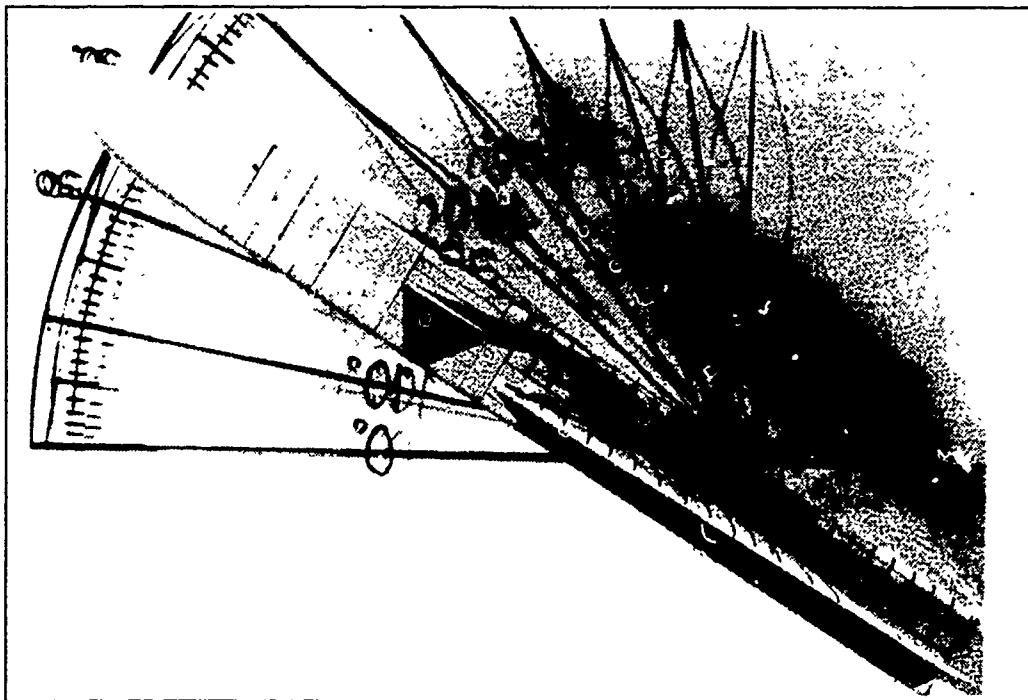
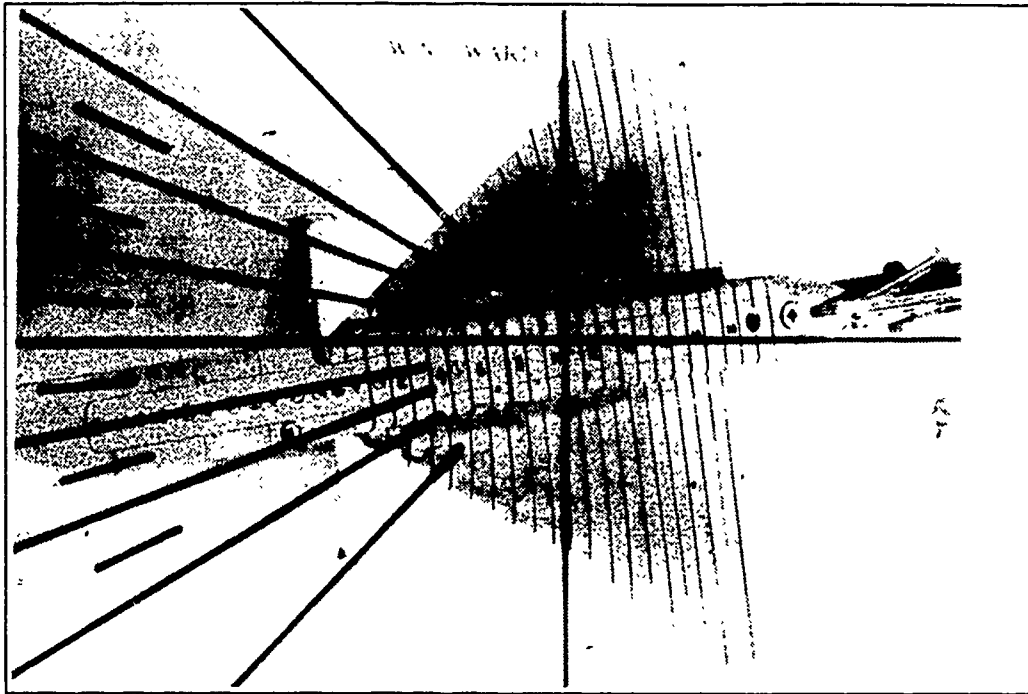


Figure 44. Wing Root Vortex Flow, Positive Sideslipping  
 ( $k=0.05$ ),  $\alpha=30^\circ$ ,  $\beta=10^\circ$



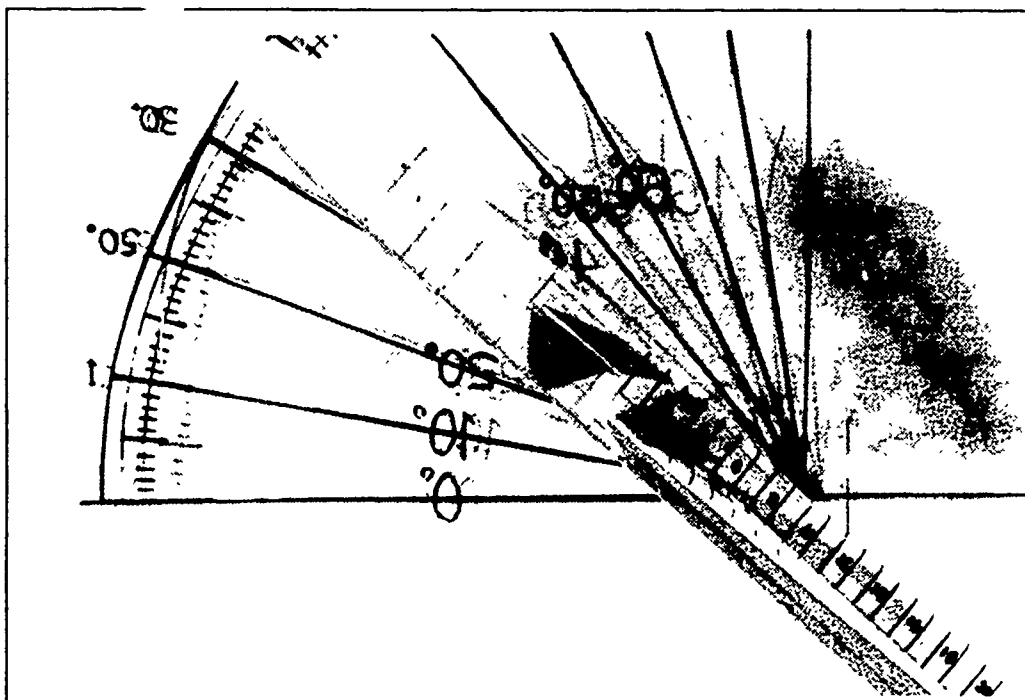
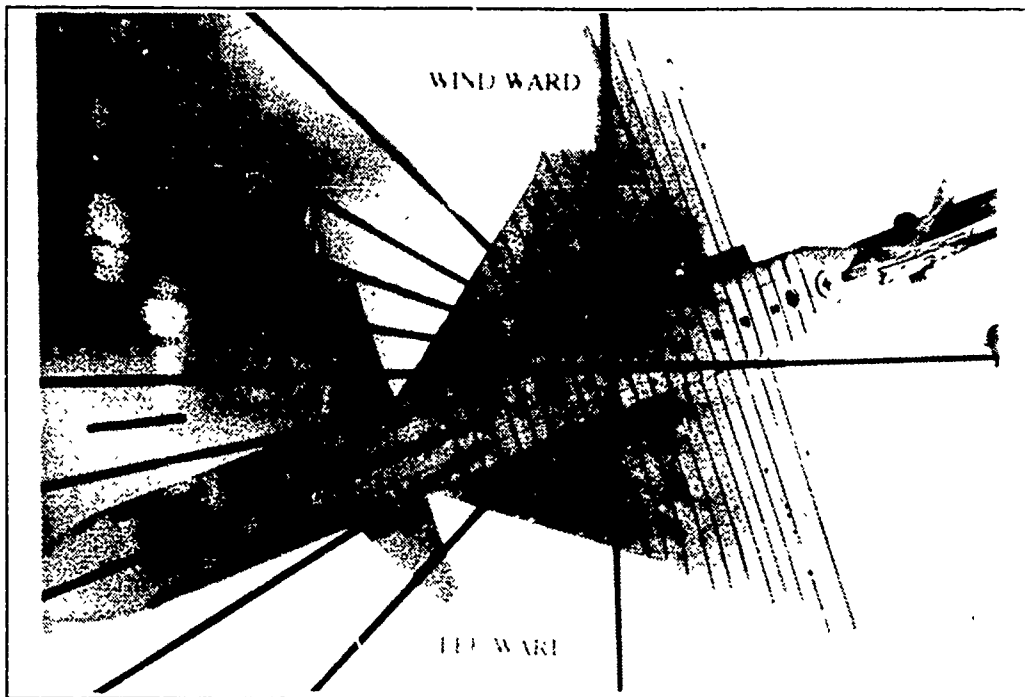


Figure 45. Wing Root Vortex Flow, Positive Sideslipping  
 $(k=0.05)$ ,  $\alpha=35^\circ$ ,  $\beta=20^\circ$

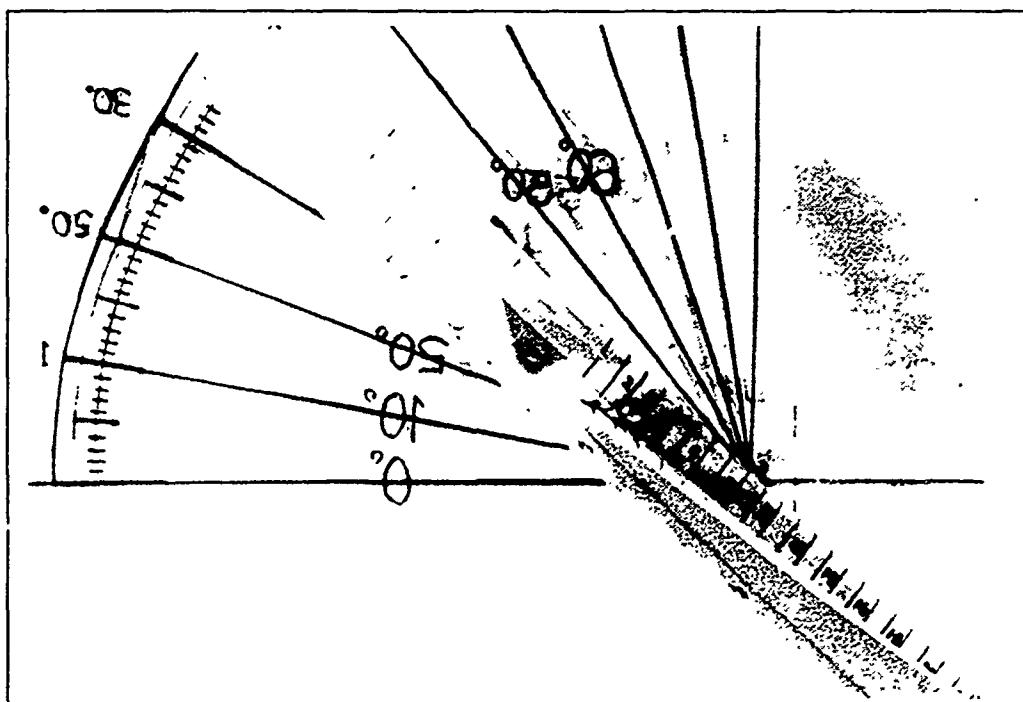
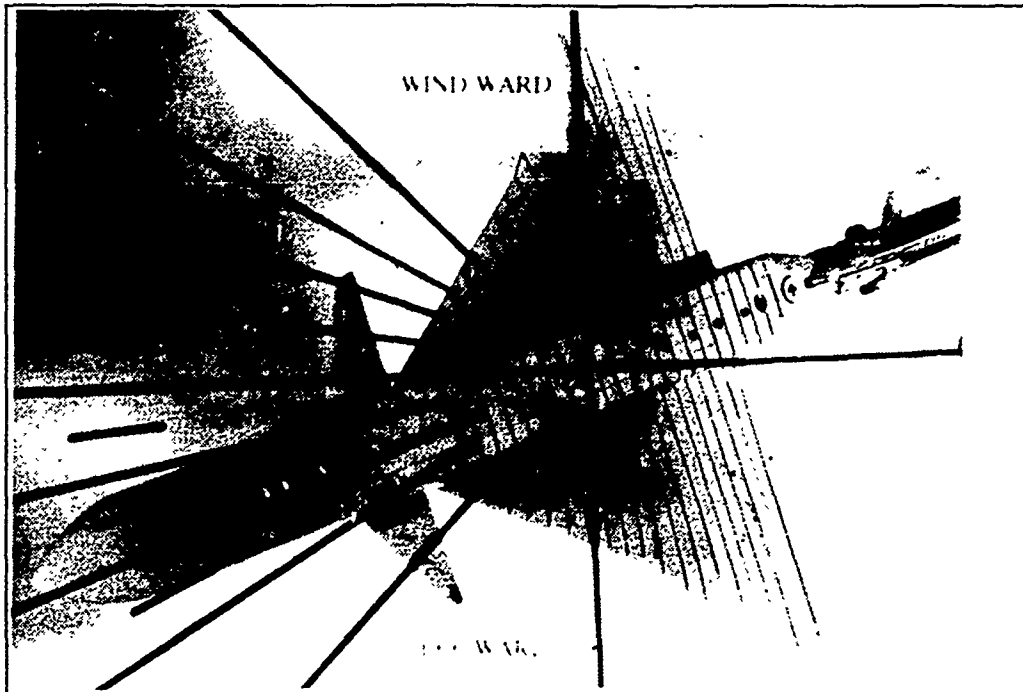


Figure 46. Wing Root Vortex Flow, Positive Sideslipping ( $k=0.05$ ),  $\alpha=40^\circ$ ,  $\beta=20^\circ$

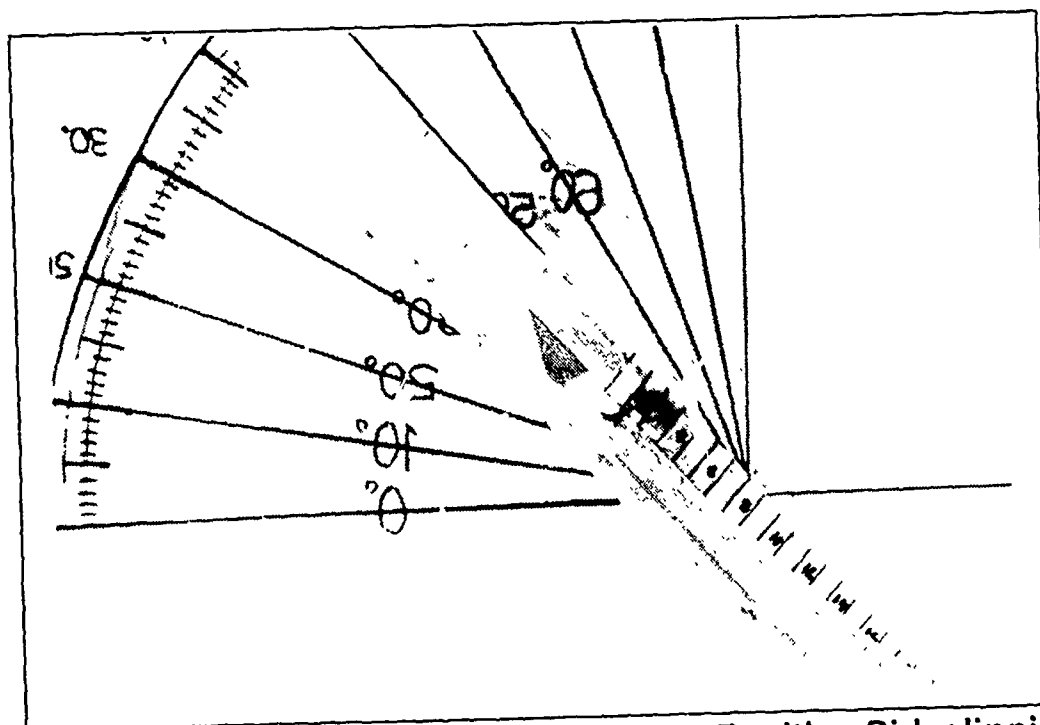
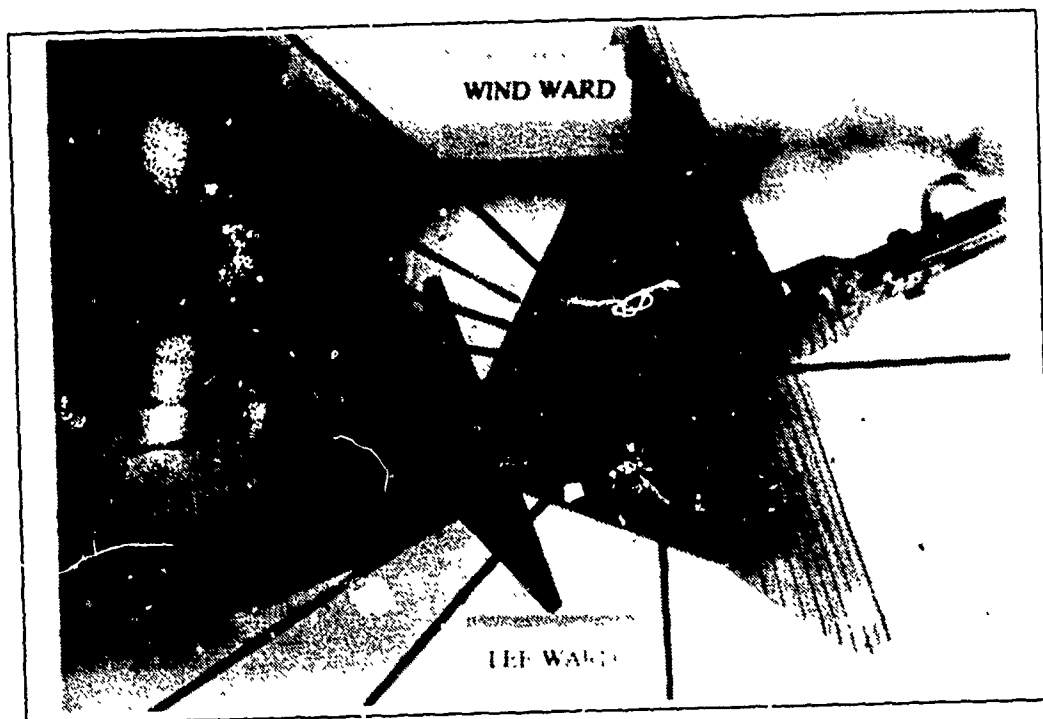


Figure 47. Wing Root Vortex Flow, Positive Sideslipping  
 $(k=0.05)$ ,  $\alpha=45^\circ$ ,  $\beta=20^\circ$

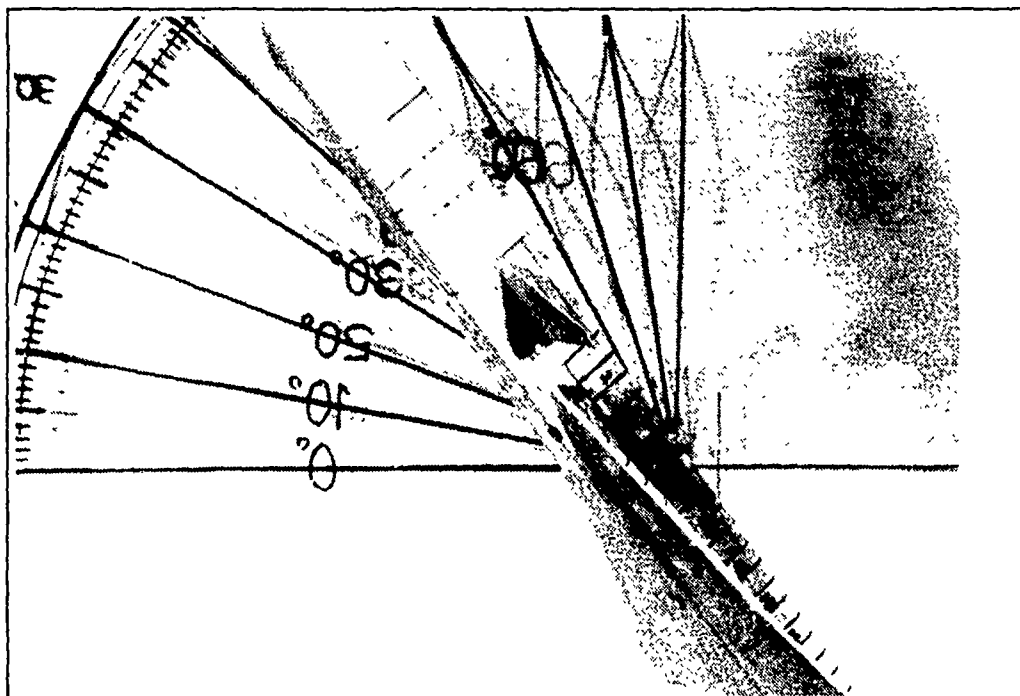
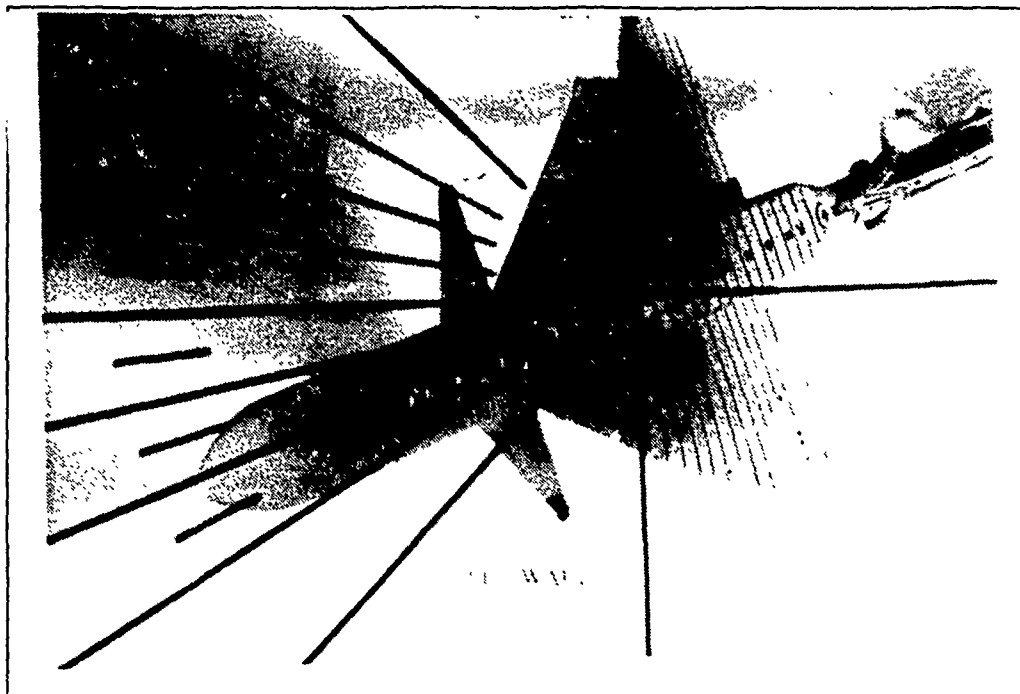


Figure 48. Wing Root Vortex Flow, Positive Sideslipping ( $k=0.05$ ),  $\alpha=50^\circ$ ,  $\beta=20^\circ$

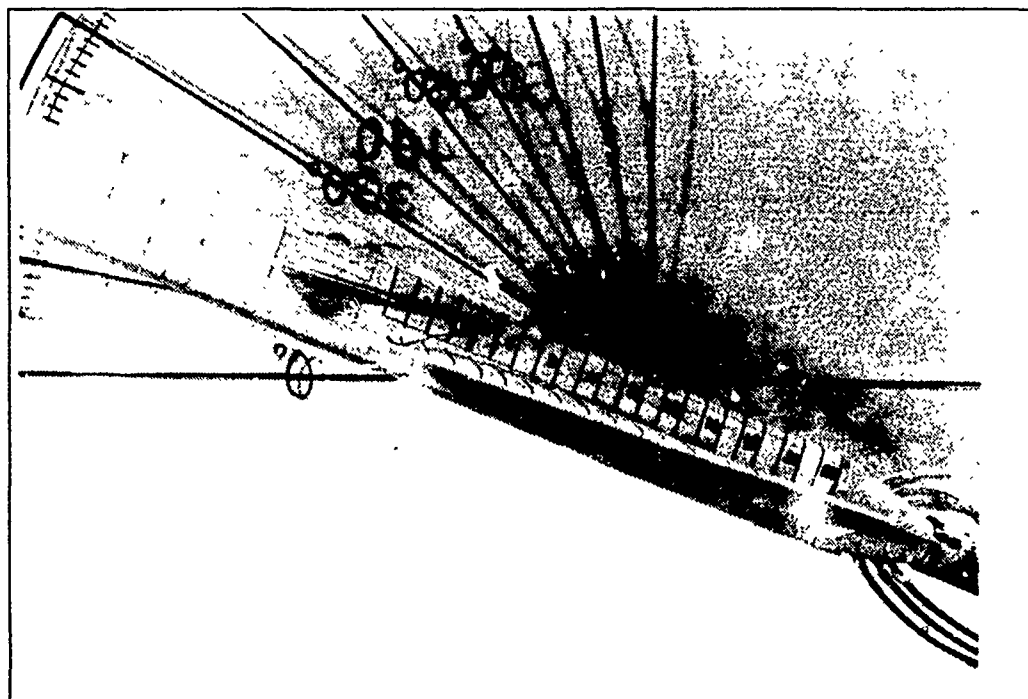
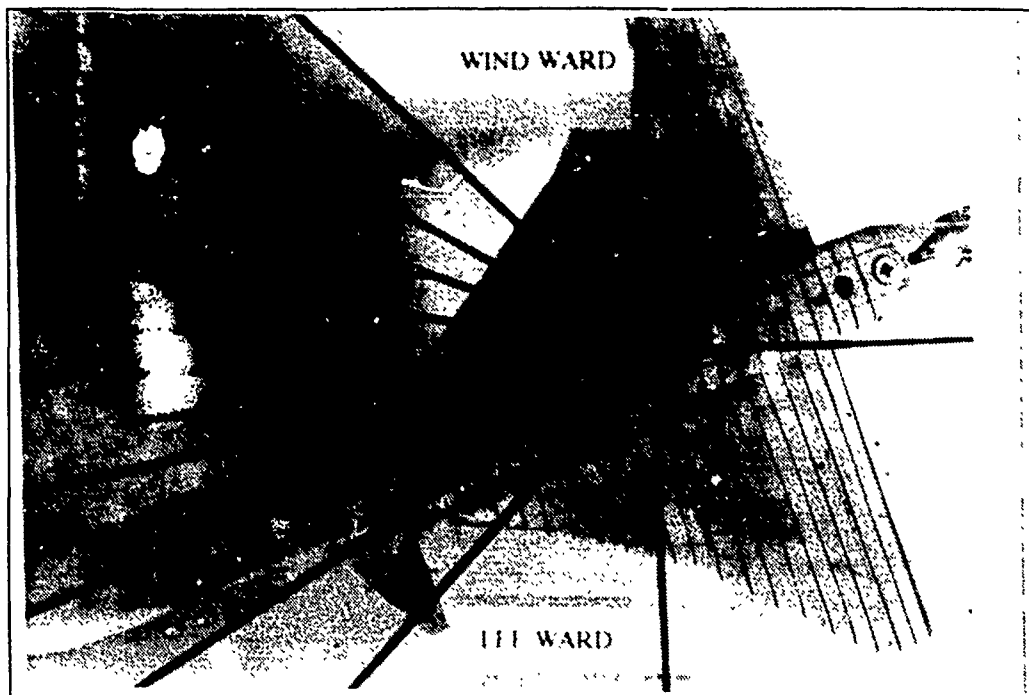


Figure 49. Wing Root Vortex Flow, Negative Sideslipping  
 $(k=-0.08)$ ,  $\alpha=20^\circ$ ,  $\beta=20^\circ$  (Same as Static Case Fig. 19)

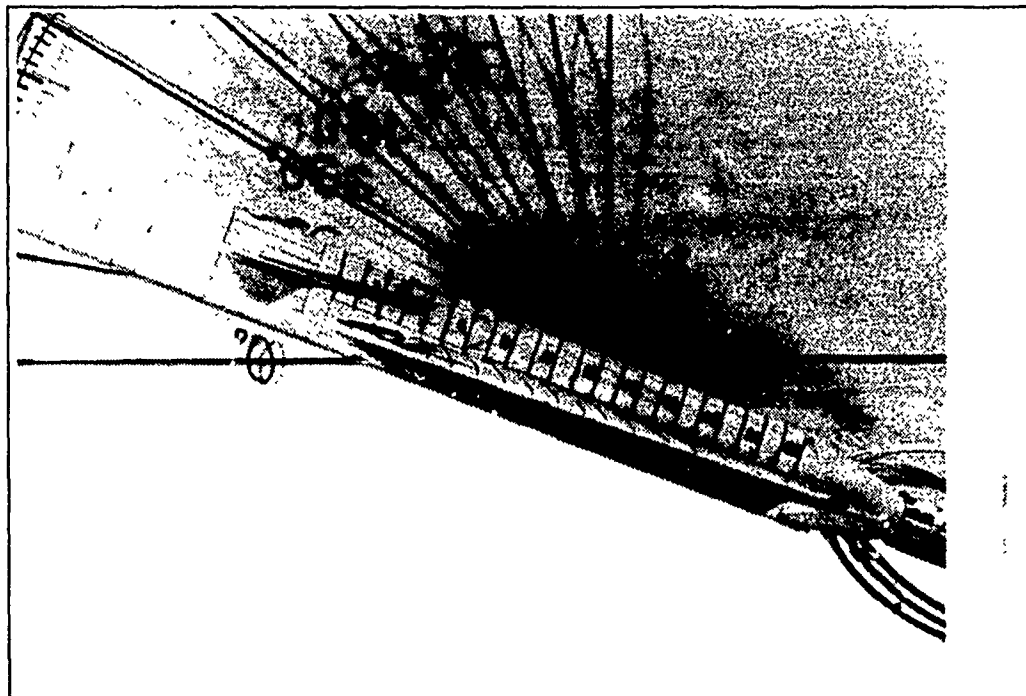
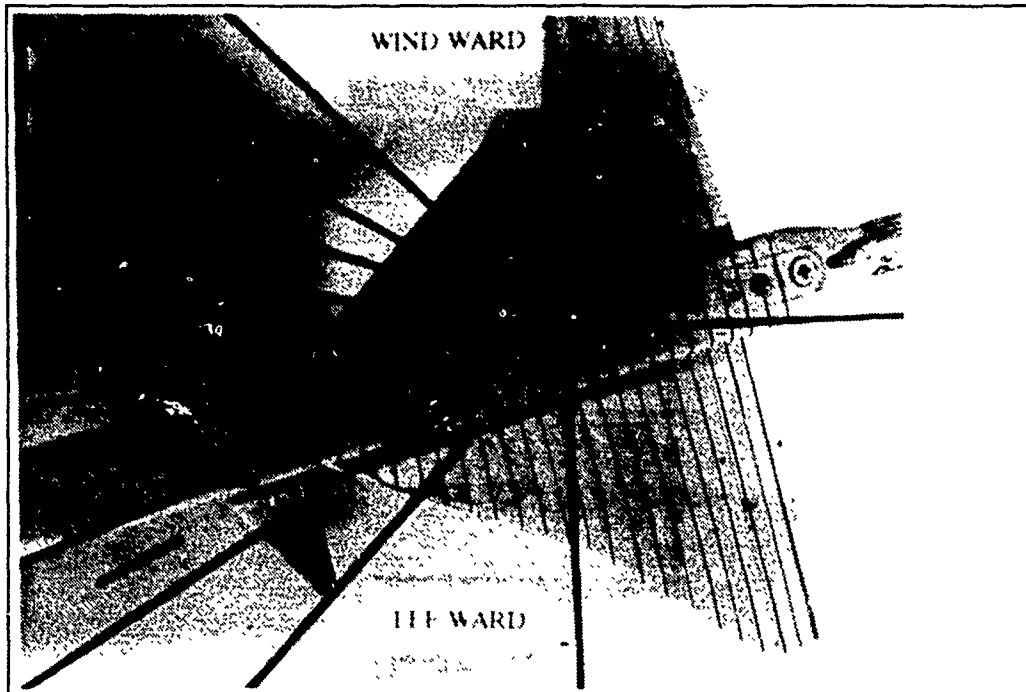


Figure 50. Wing Root Vortex Flow, Negative Sideslipping  
 $(k=-0.08)$ ,  $\alpha=20^\circ$ ,  $\beta=15^\circ$

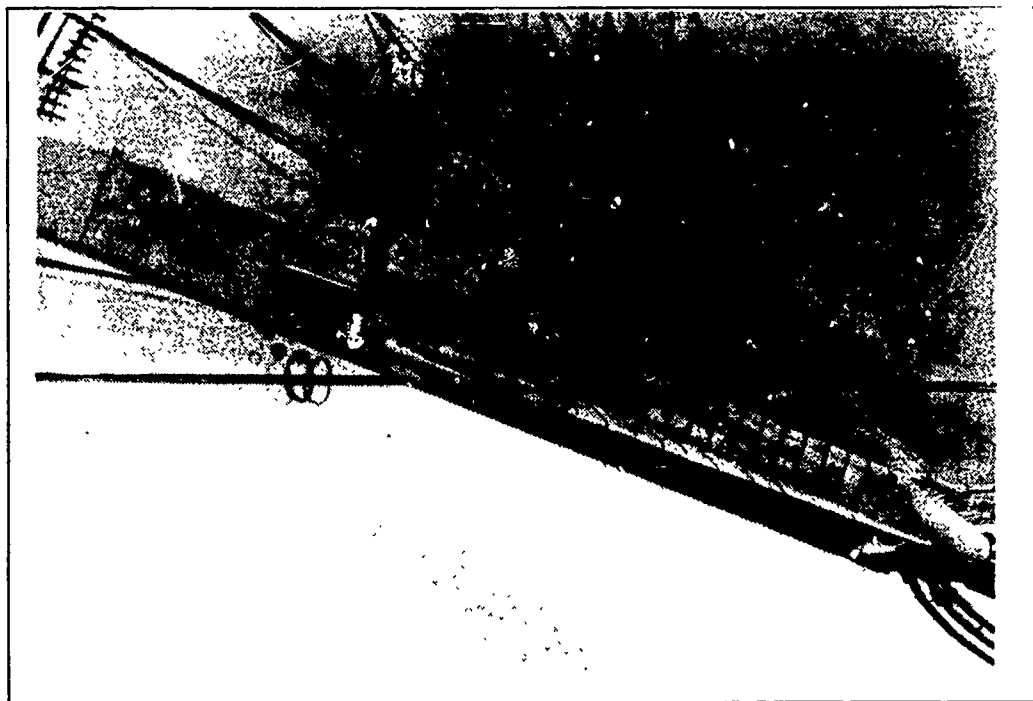
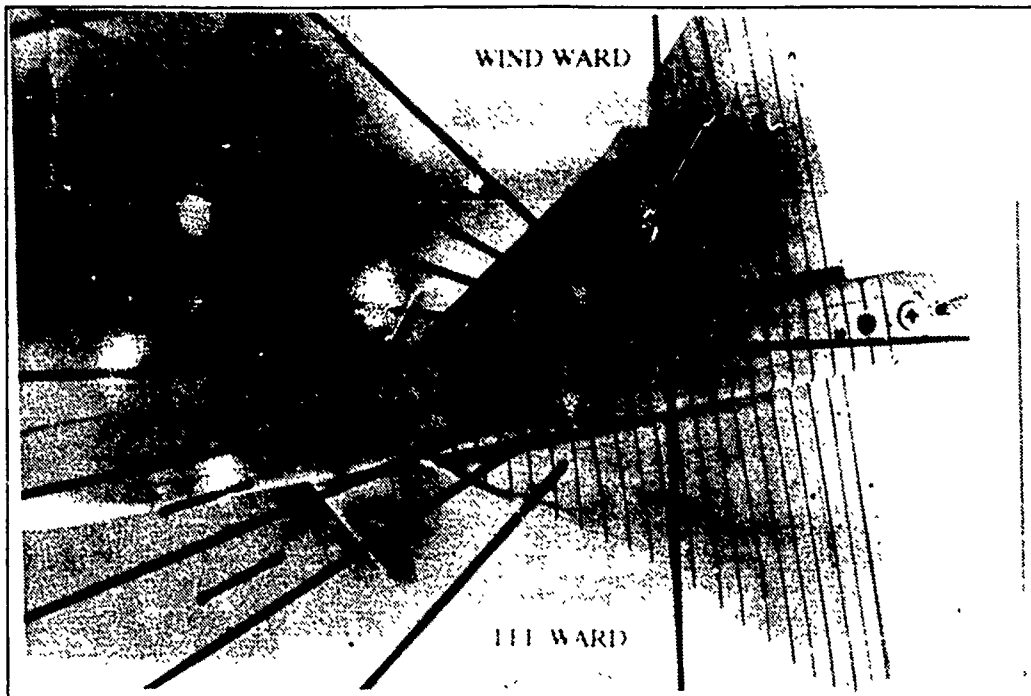


Figure 51. Wing Root Vortex Flow, Negative Sideslipping  
 ( $k=-0.08$ ),  $\alpha=20^\circ$ ,  $\beta=10^\circ$

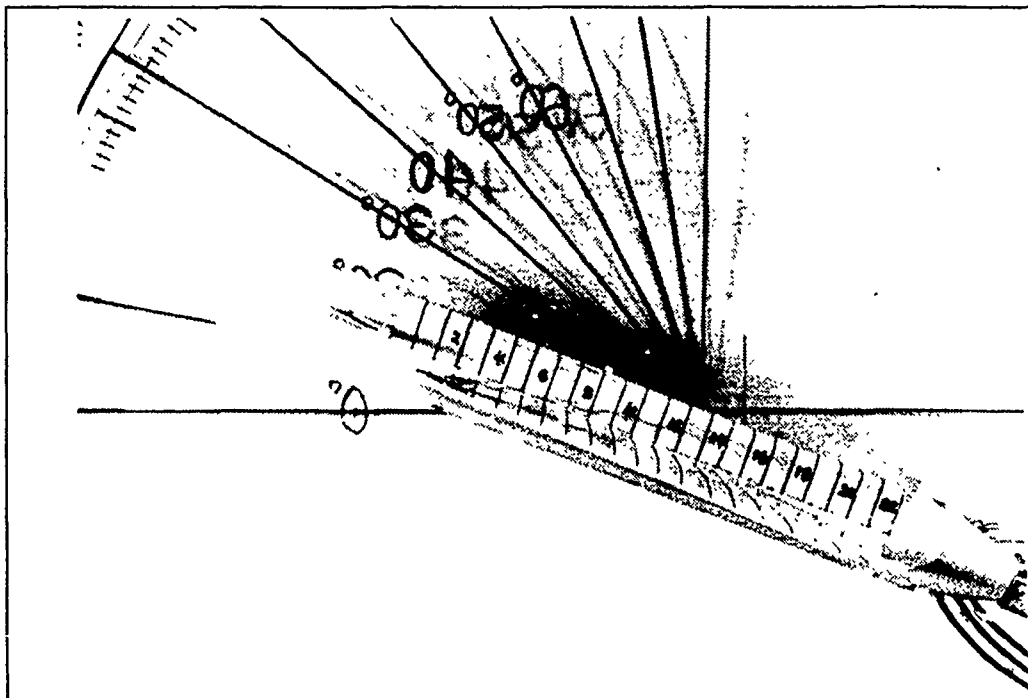
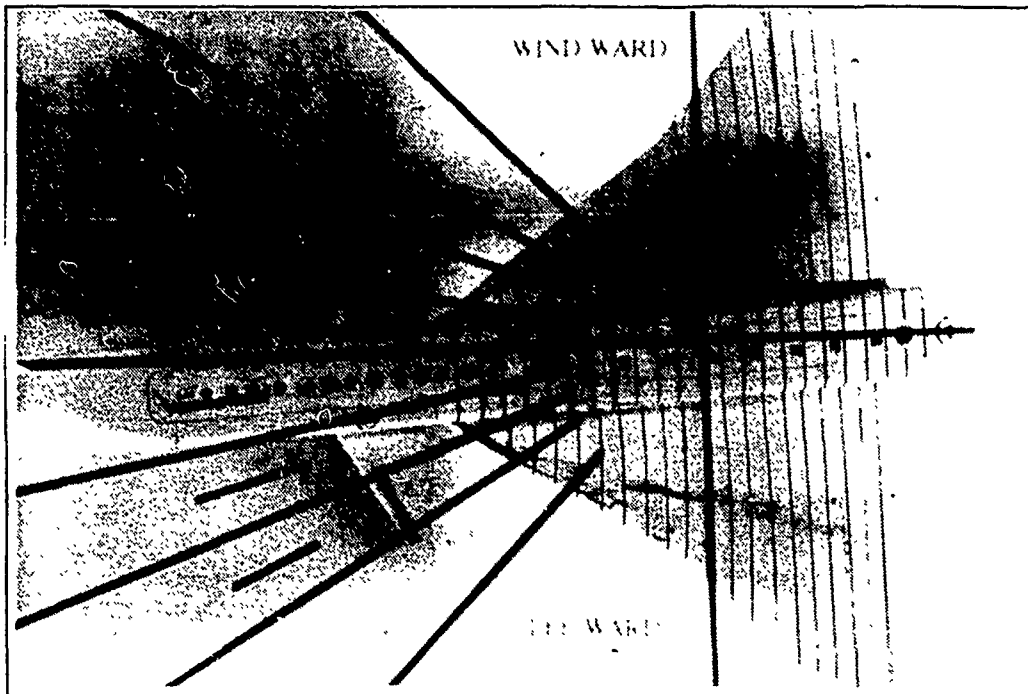


Figure 52. Wing Root Vortex Flow, Negative Sideslipping  
 $(k=-0.08)$ ,  $\alpha=20^\circ$ ,  $\beta=5^\circ$



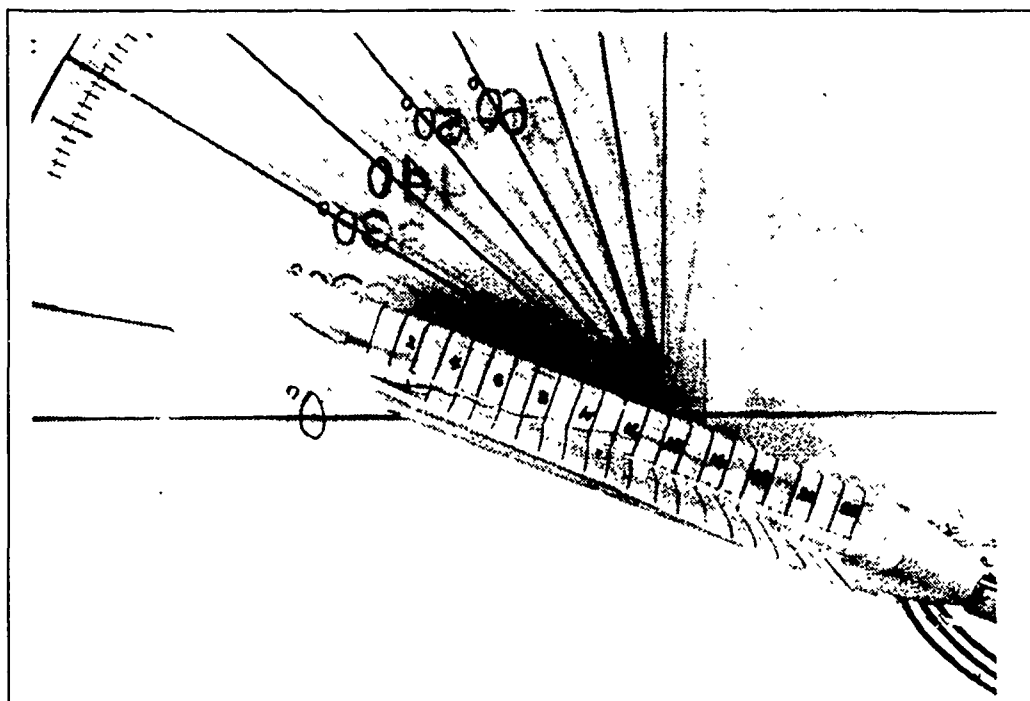
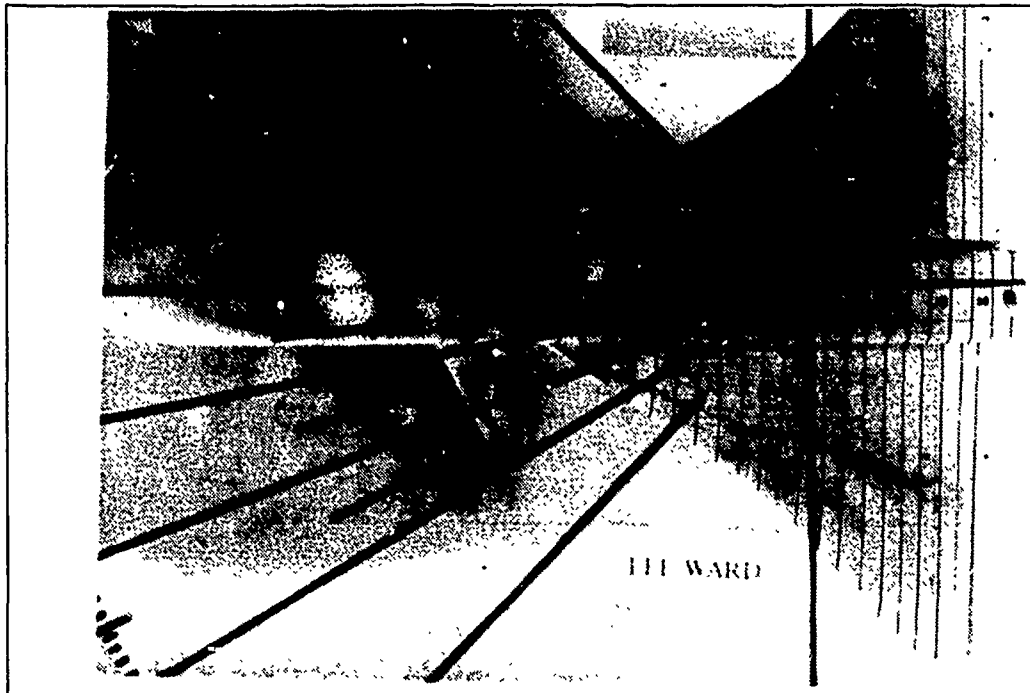


Figure 53. Wing Root Vortex Flow, Negative Sideslipping  
 $(k=-0,08)$ ,  $\alpha=20^\circ$ ,  $\beta=0^\circ$

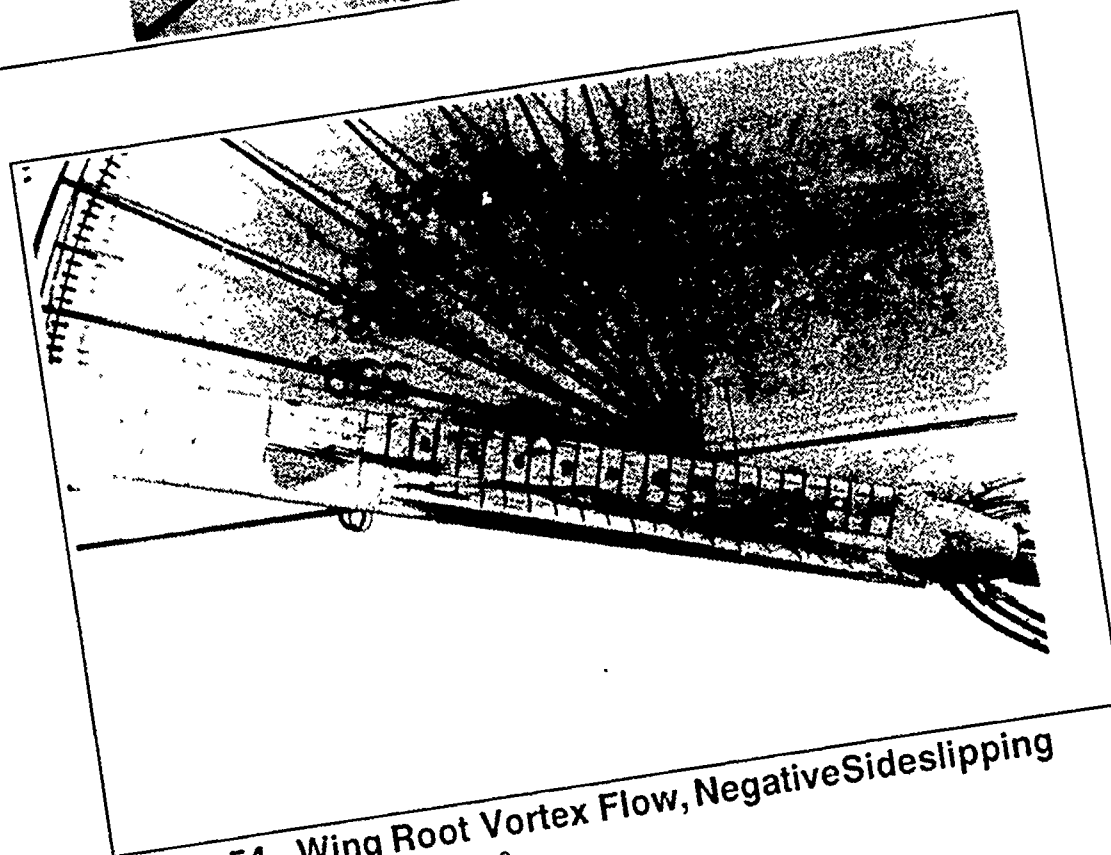


Figure 54. Wing Root Vortex Flow, Negative Sideslipping  
 ( $k = -0.08$ ),  $\alpha = 15^\circ$ ,  $\beta = 10^\circ$

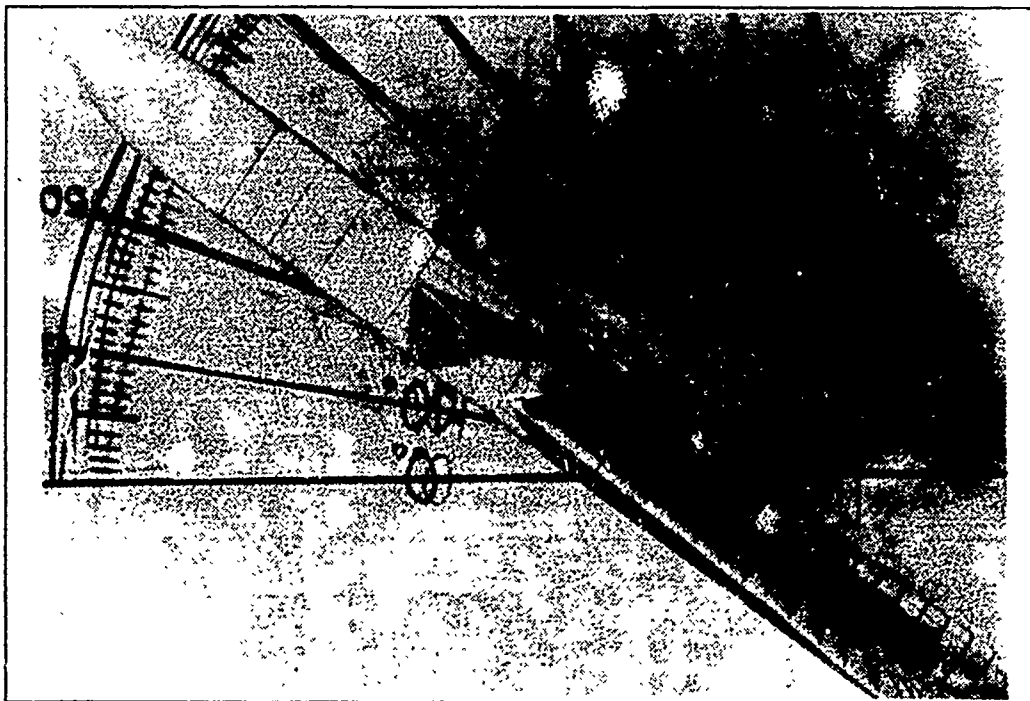
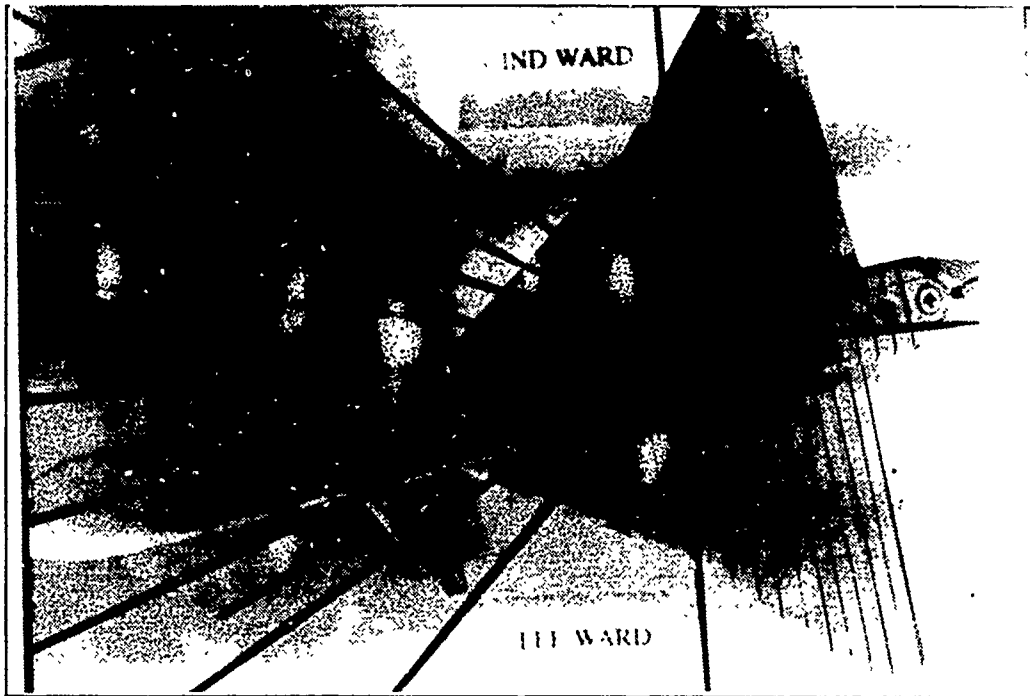


Figure 55. Wing Root Vortex Flow, Negative Sideslipping  
 $(k=-0.08)$ ,  $\alpha=25^\circ$ ,  $\beta=10^\circ$

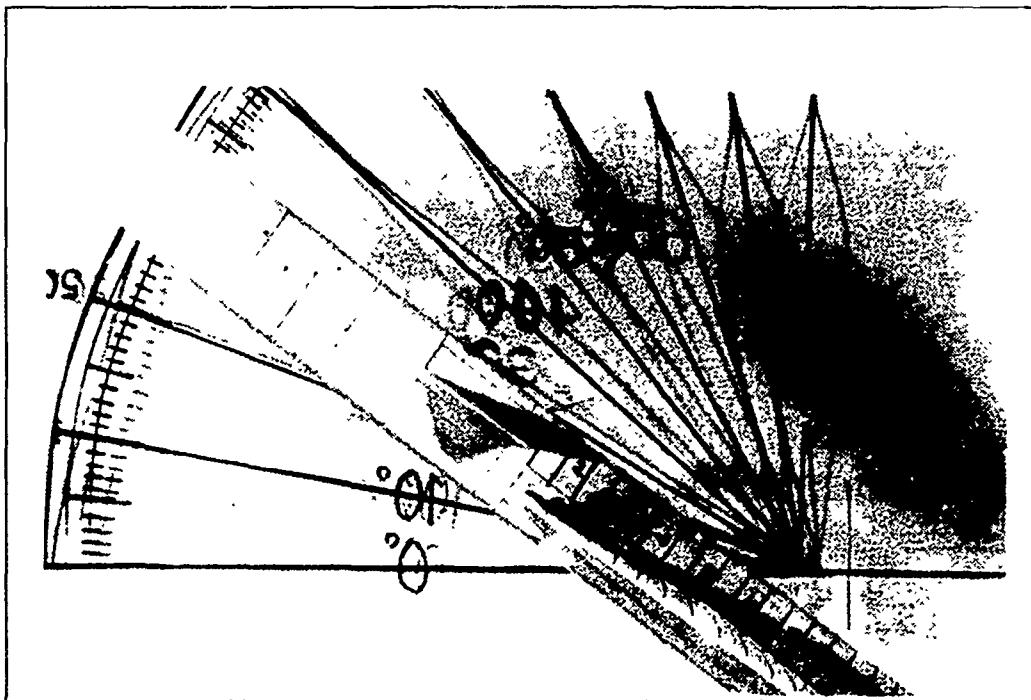
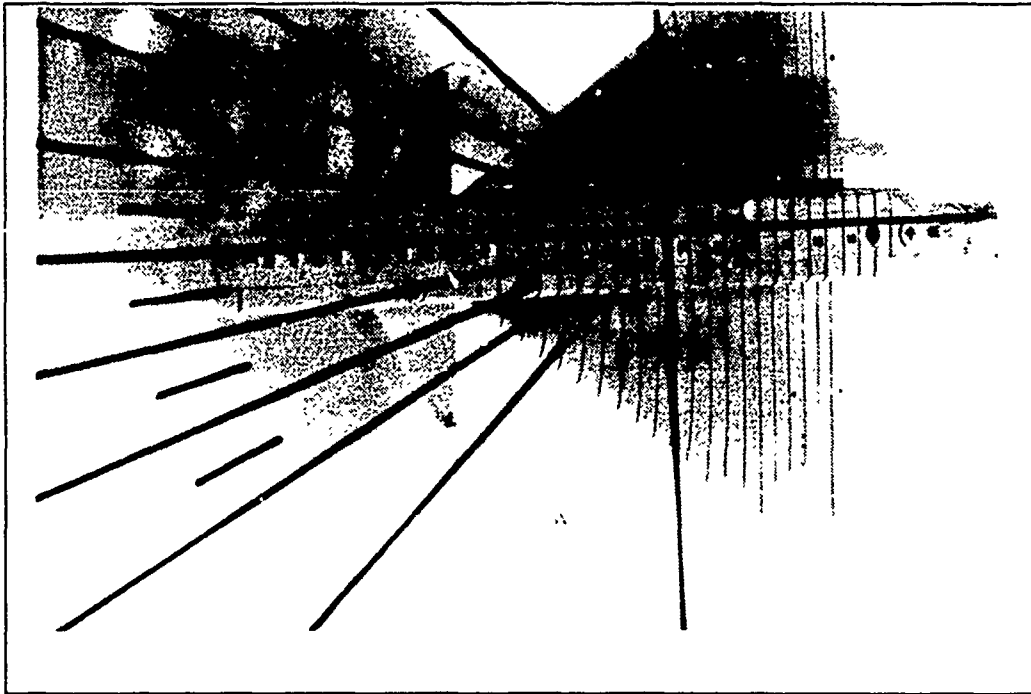


Figure 56. Wing Root Vortex Flow, Negative Sideslipping  
 $(k=-0.08)$ ,  $\alpha=35^\circ$ ,  $\beta=0^\circ$

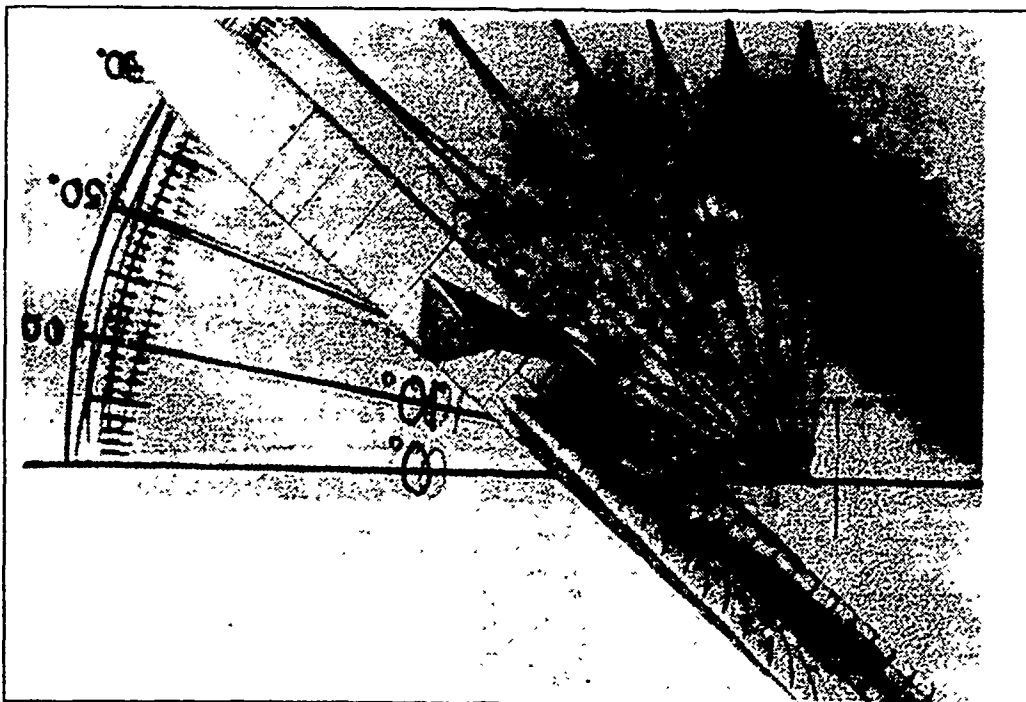
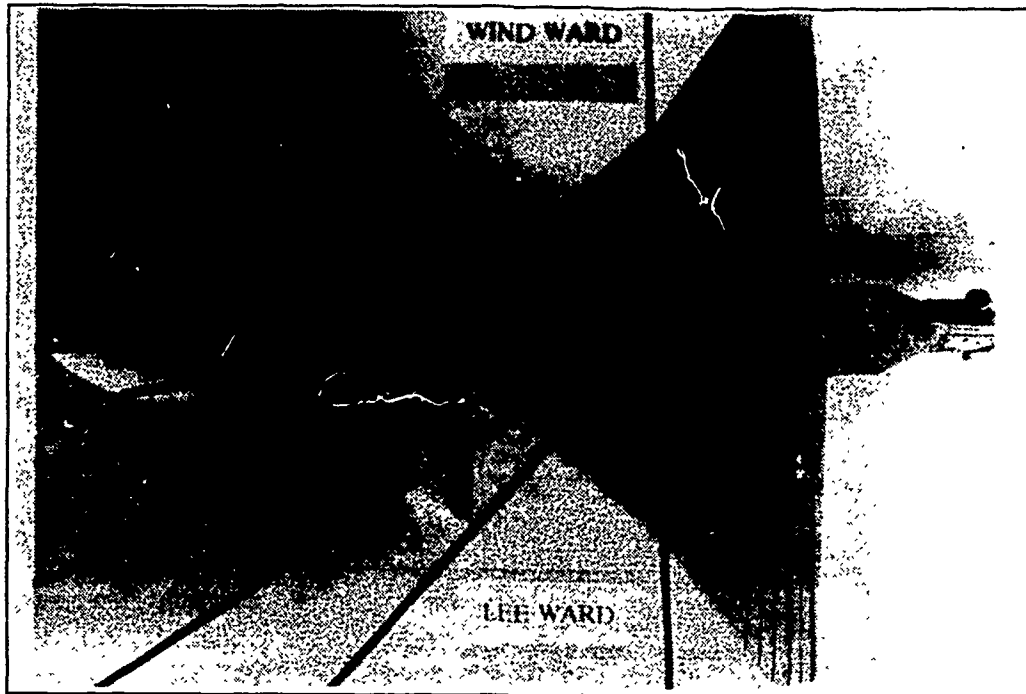


Figure 57. Wing Root Vortex Flow, Negative Sideslipping  
 ( $k=-0.08$ ),  $\alpha=40^\circ$ ,  $\beta=0^\circ$

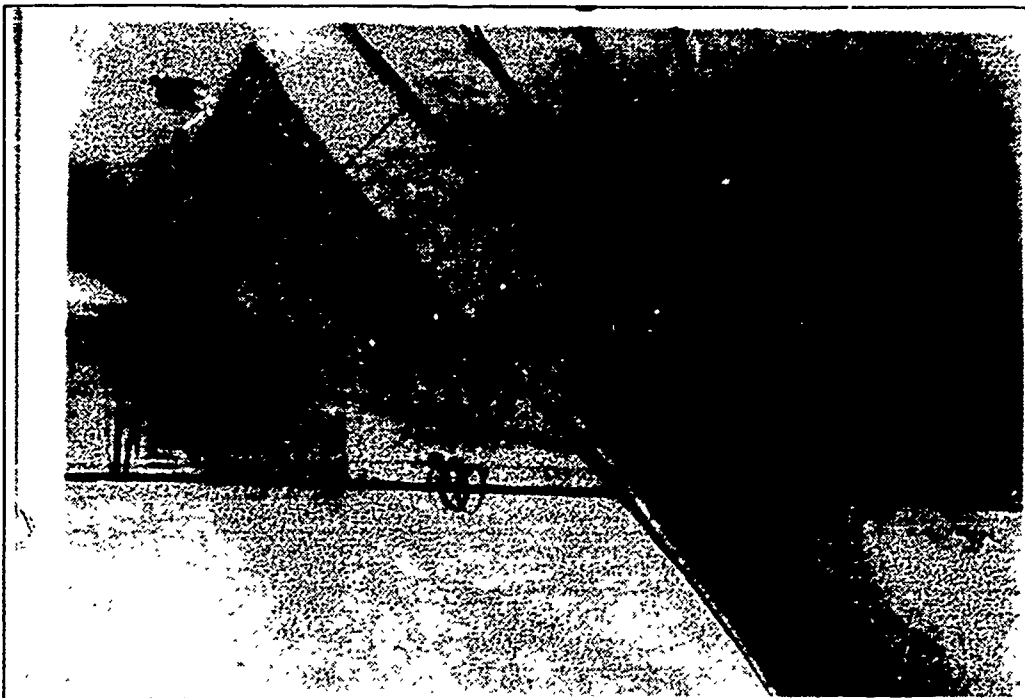
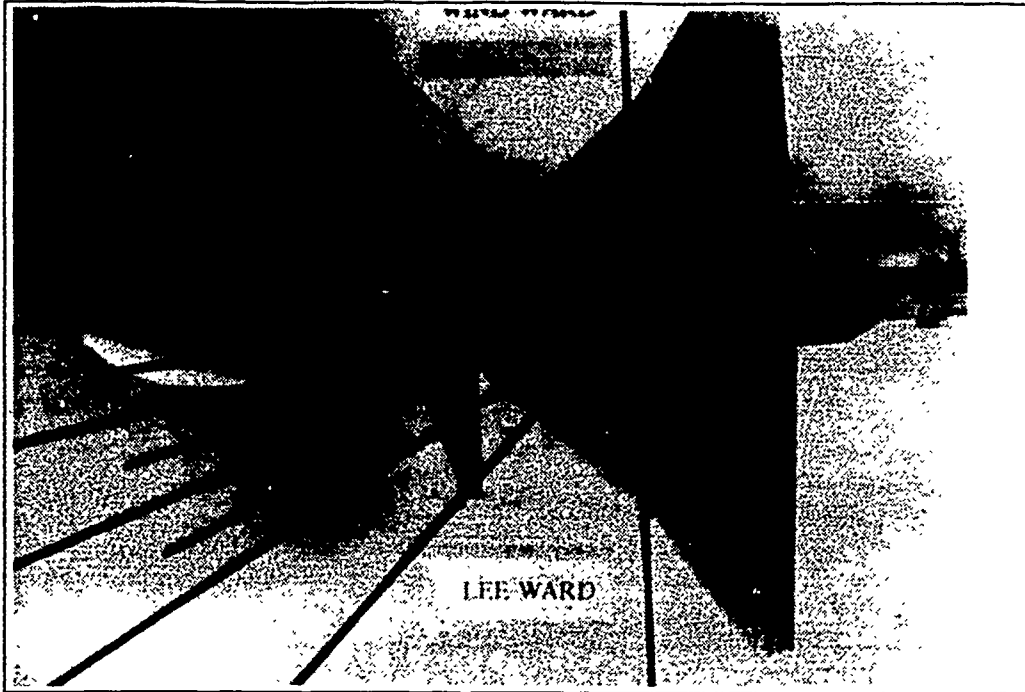


Figure 58. Wing Root Vortex Flow, Negative Sideslipping  
 $(k=-0.08)$ ,  $\alpha=45^\circ$ ,  $\beta=0^\circ$

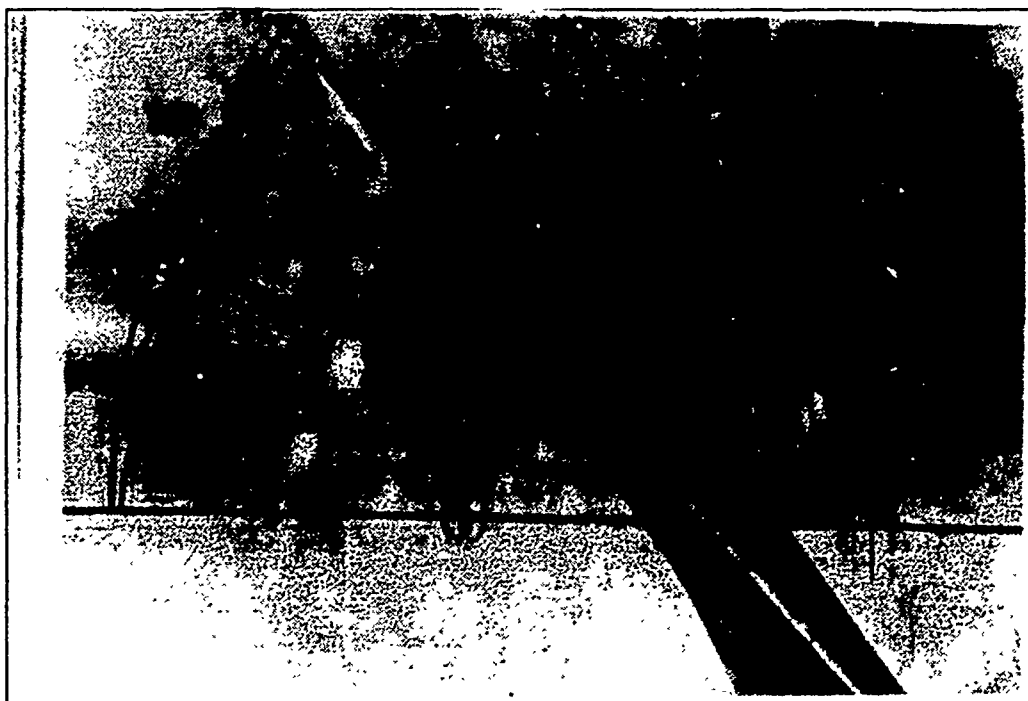
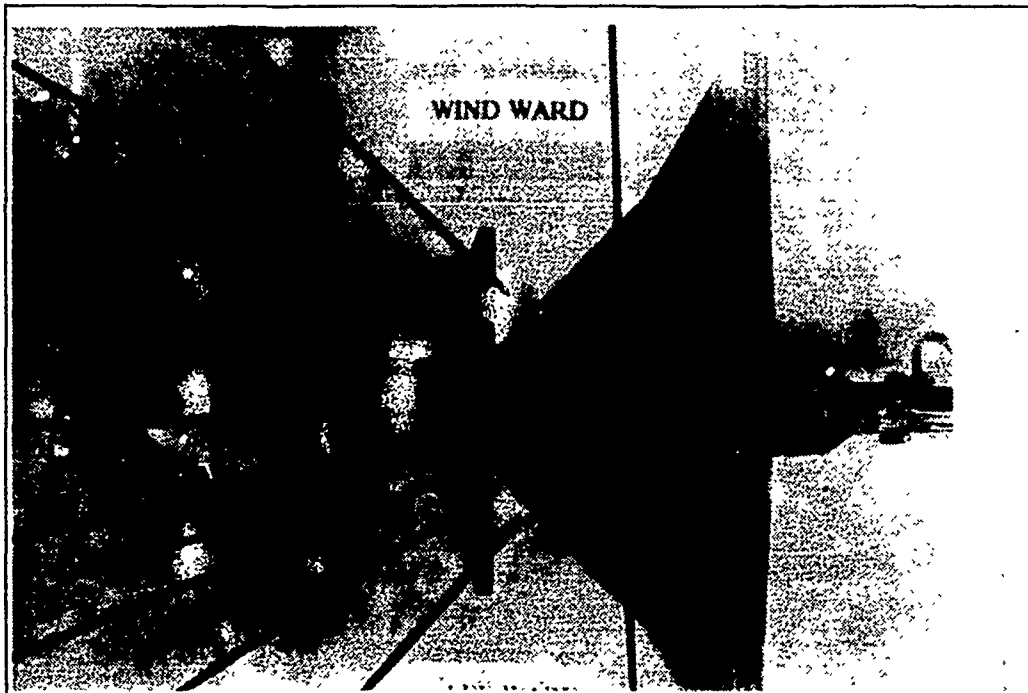


Figure 59. Wing Root Vortex Flow, Negative Sideslipping  
 $(k=-0.08)$ ,  $\alpha=50^\circ$ ,  $\beta=0^\circ$

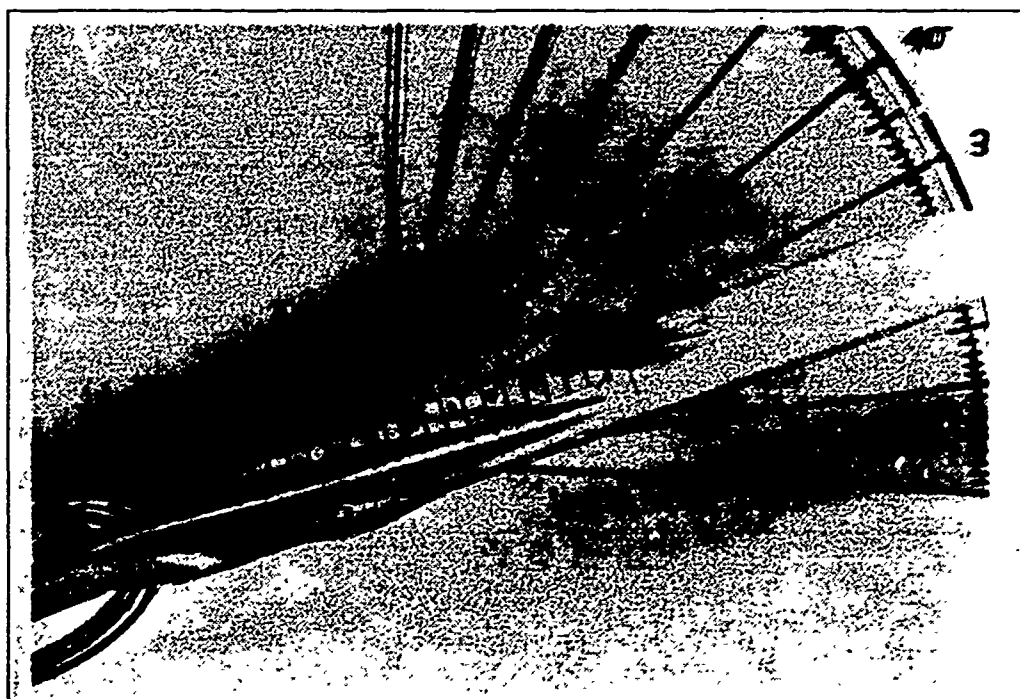
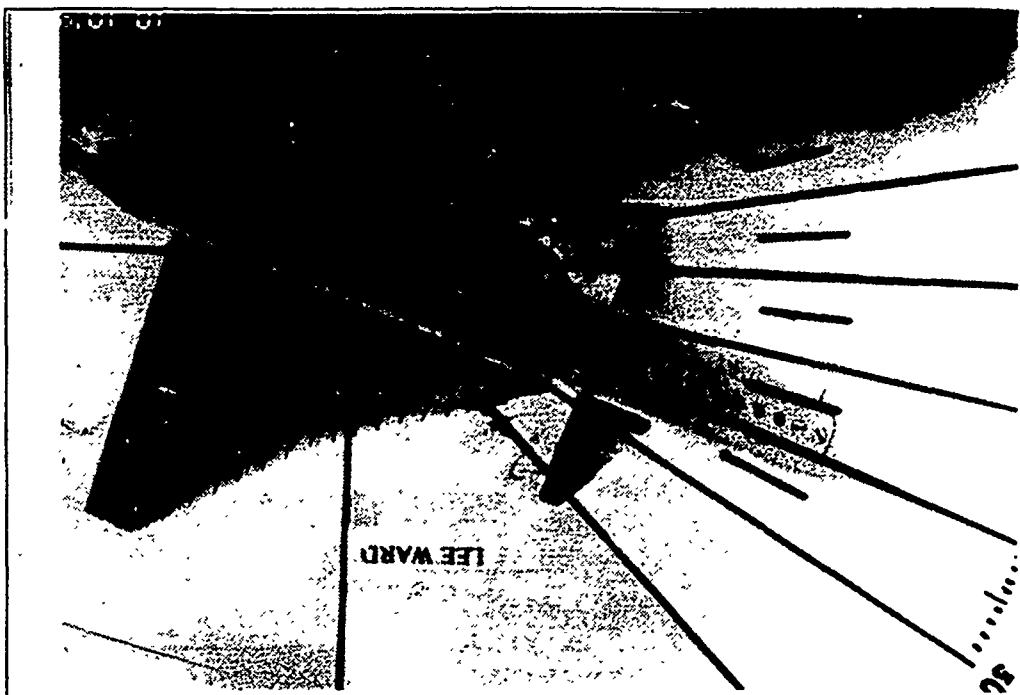


Figure 60. Wing Root Vortex Flow, Negative Sideslipping ( $k=-0.05$ ),  $\alpha=20^\circ$ ,  $\beta=20^\circ$  (Same as Static Case Fig. 19)



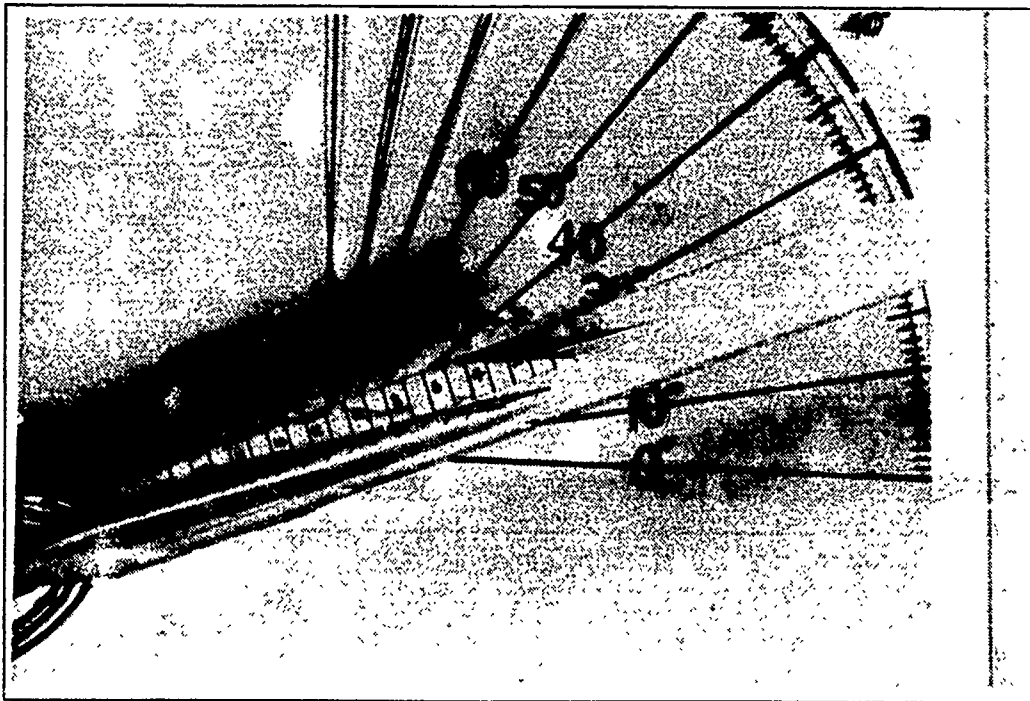
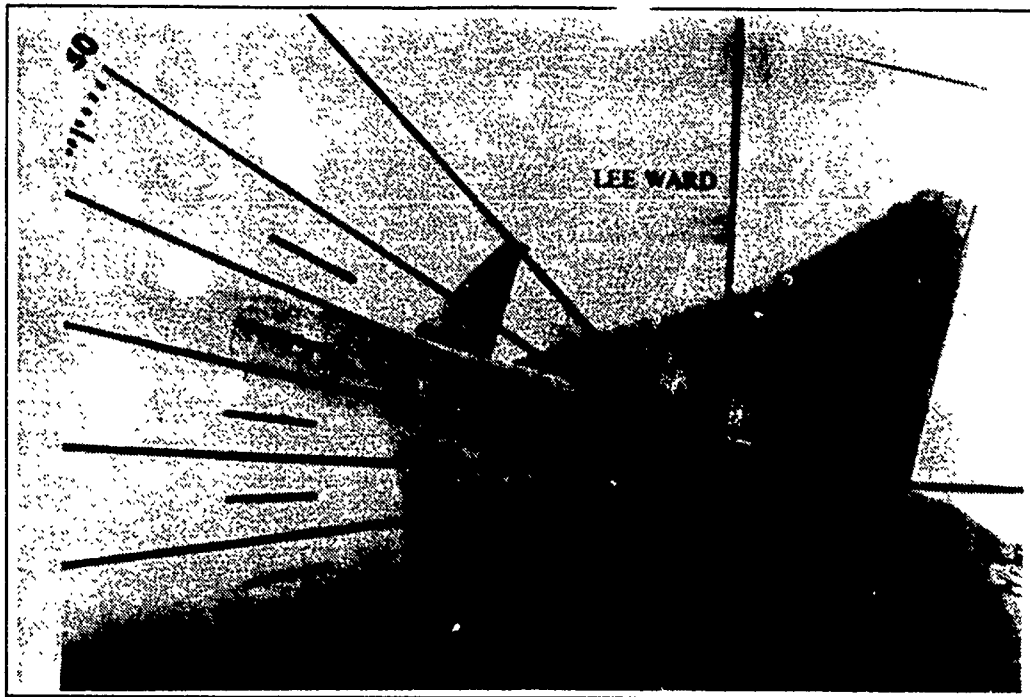


Figure 61. Wing Root Vortex Flow, Negative Sideslipping  
 ( $k=-0.05$ ),  $\alpha=20^\circ$ ,  $\beta=15^\circ$

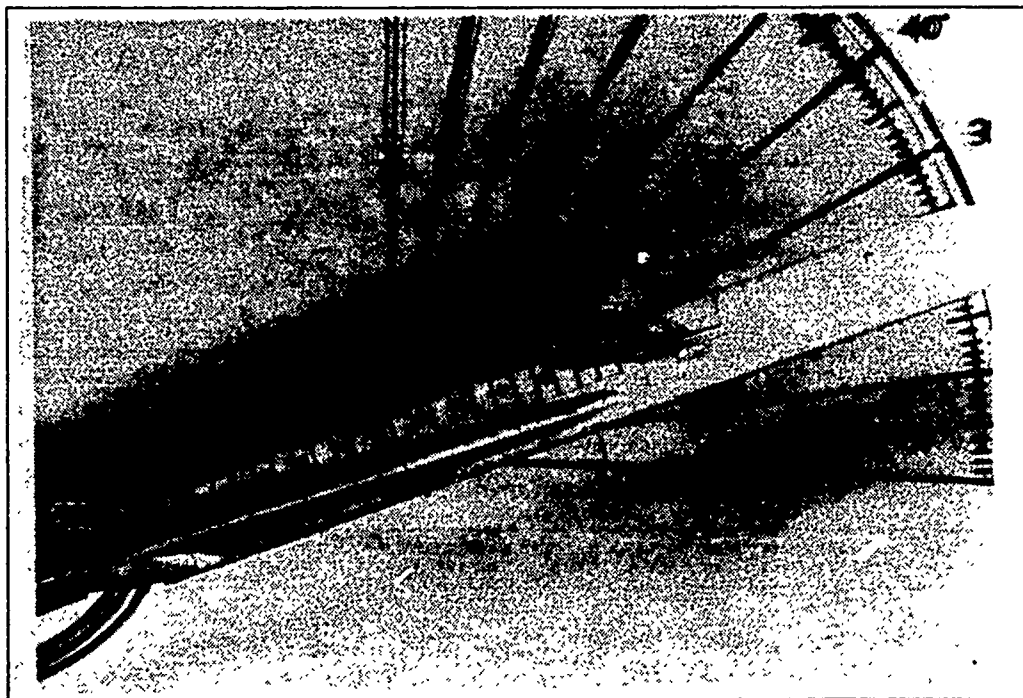
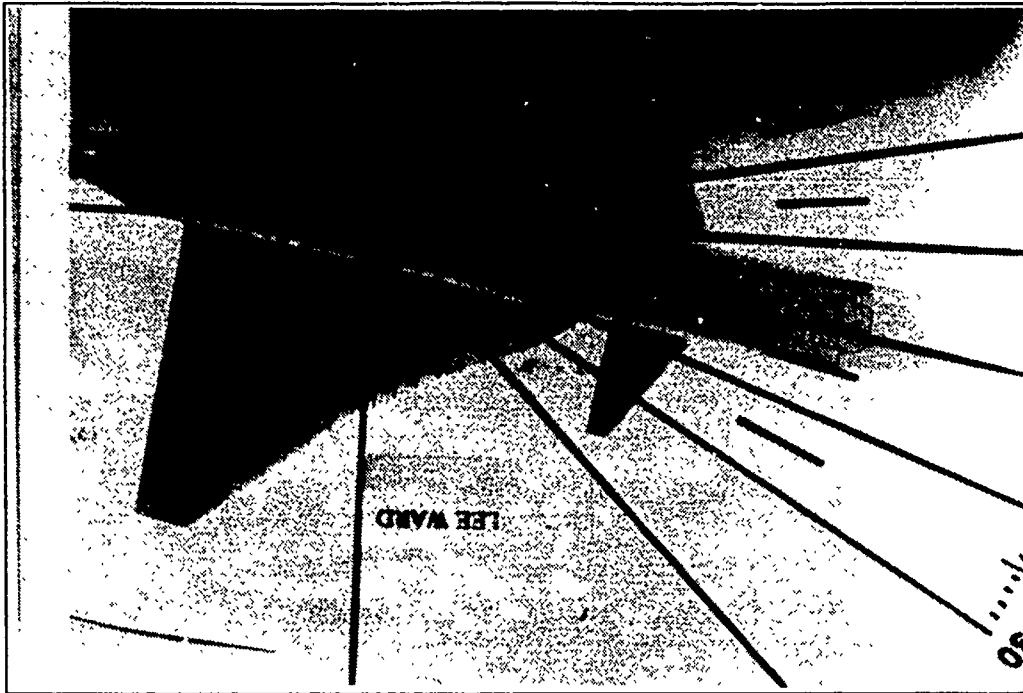


Figure 62. Wing Root Vortex Flow, Negative Sideslipping  
 $(k=-0.05)$ ,  $\alpha=20^\circ$ ,  $\beta=10^\circ$



Figure 63. Wing Root Vortex Flow, Negative Sideslipping  
 $(k=-0.05)$ ,  $\alpha=20^\circ$ ,  $\beta=5^\circ$

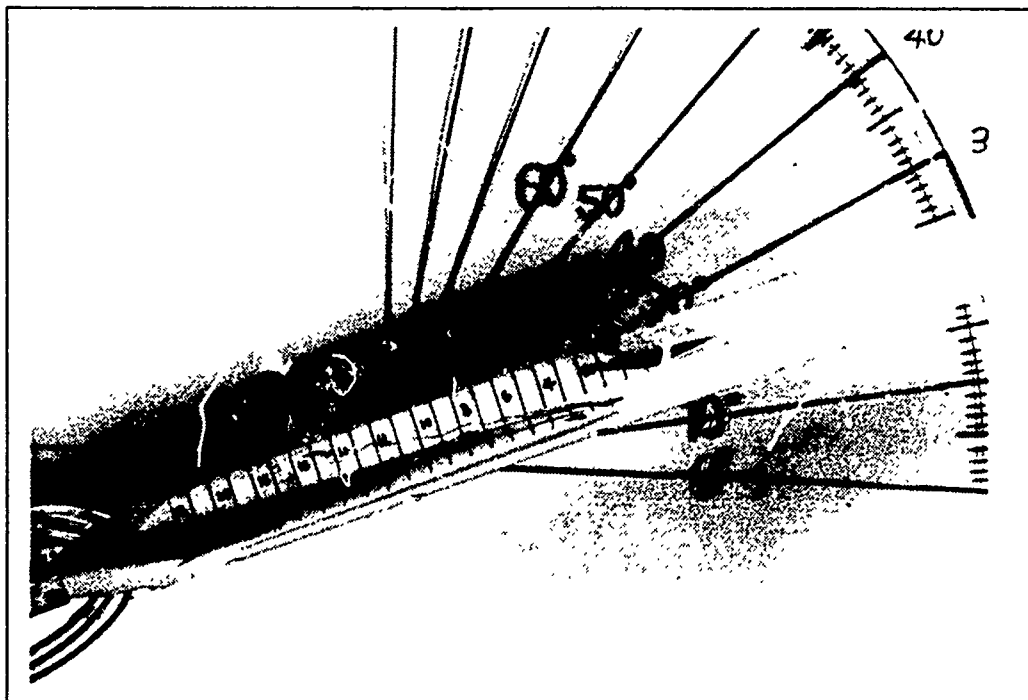
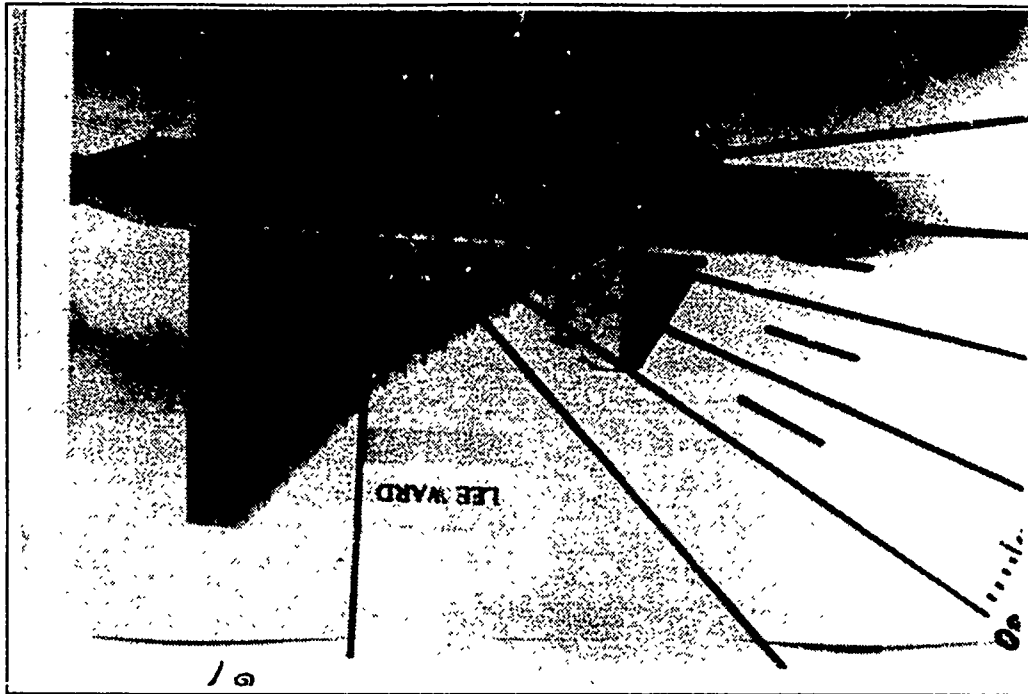


Figure 64. Wing Root Vortex Flow, Negative Sideslipping  
 ( $k=-0.05$ ),  $\alpha=20^\circ$ ,  $\beta=0^\circ$

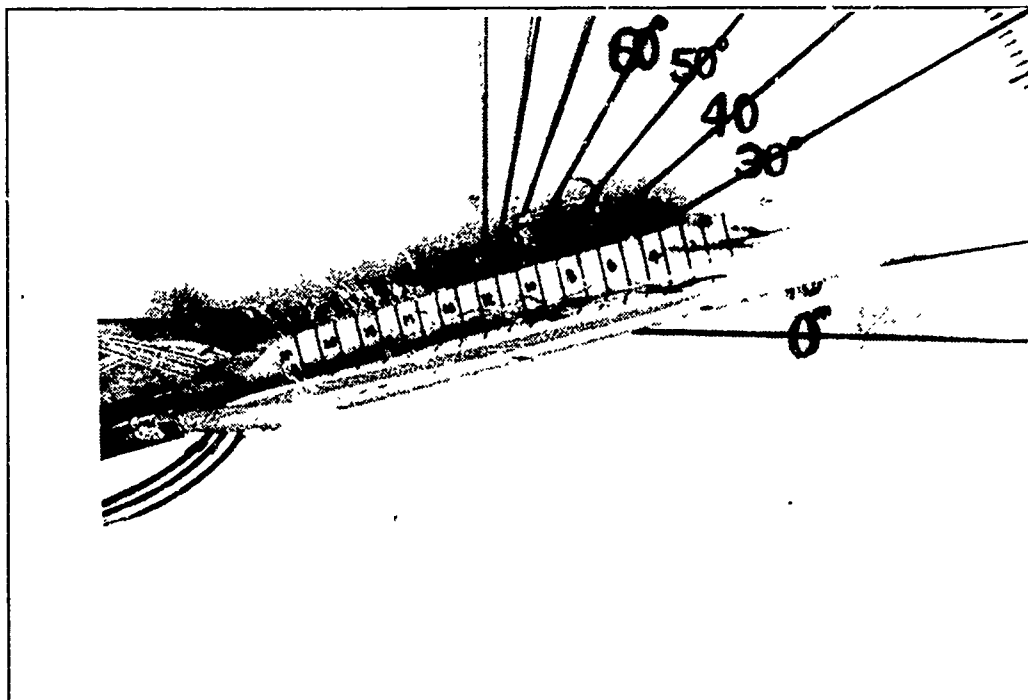
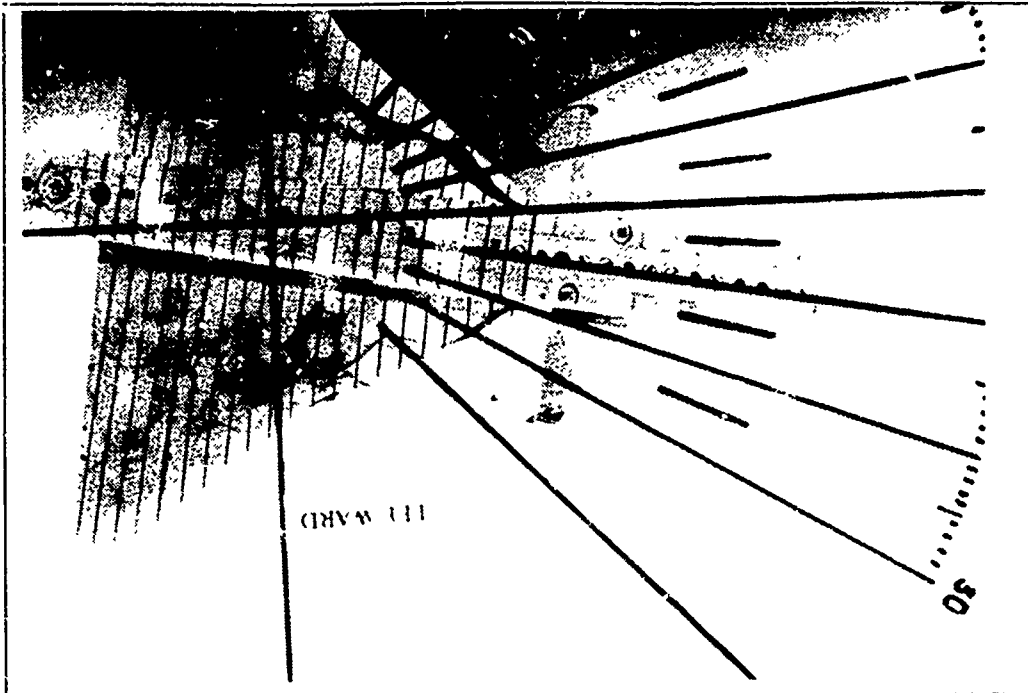


Figure 65. Wing Root Vortex Flow, Negative Sideslipping  
 $(k=-0.05)$ ,  $\alpha=15^\circ$ ,  $\beta=10^\circ$

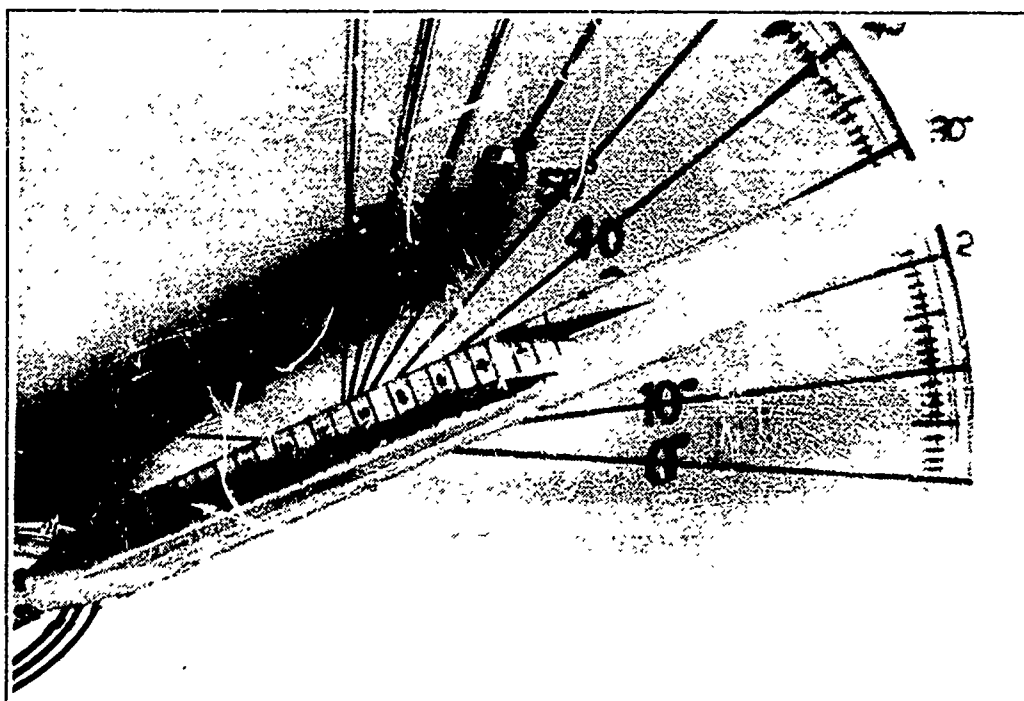
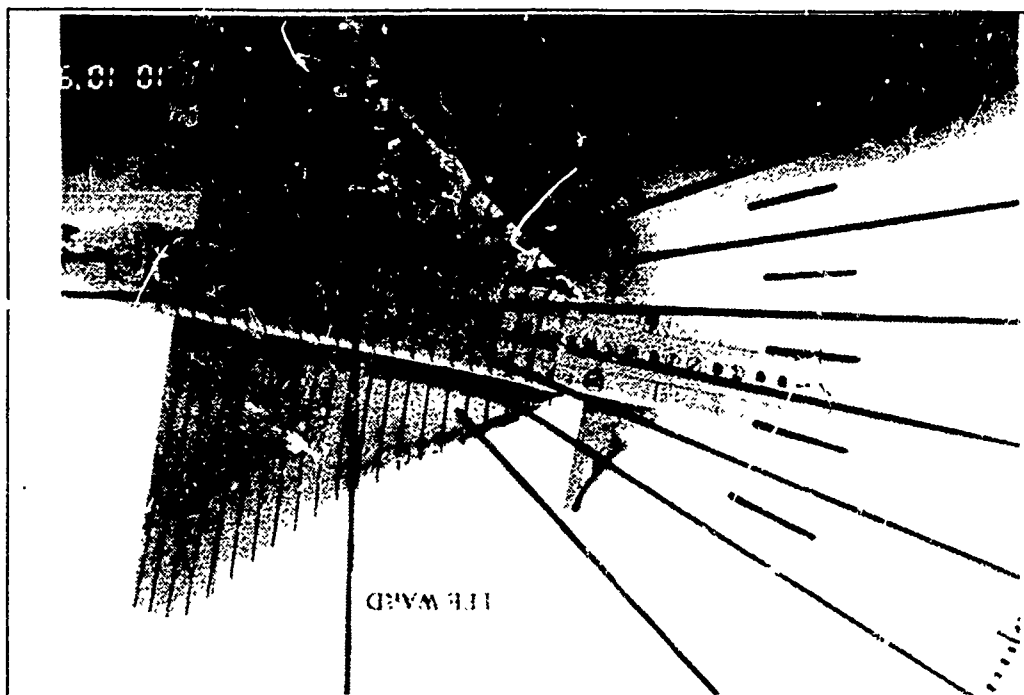


Figure 66. Wing Root Vortex Flow, Negative Sideslipping  
 ( $k=-0.05$ ),  $\alpha=25^\circ$ ,  $\beta=10^\circ$

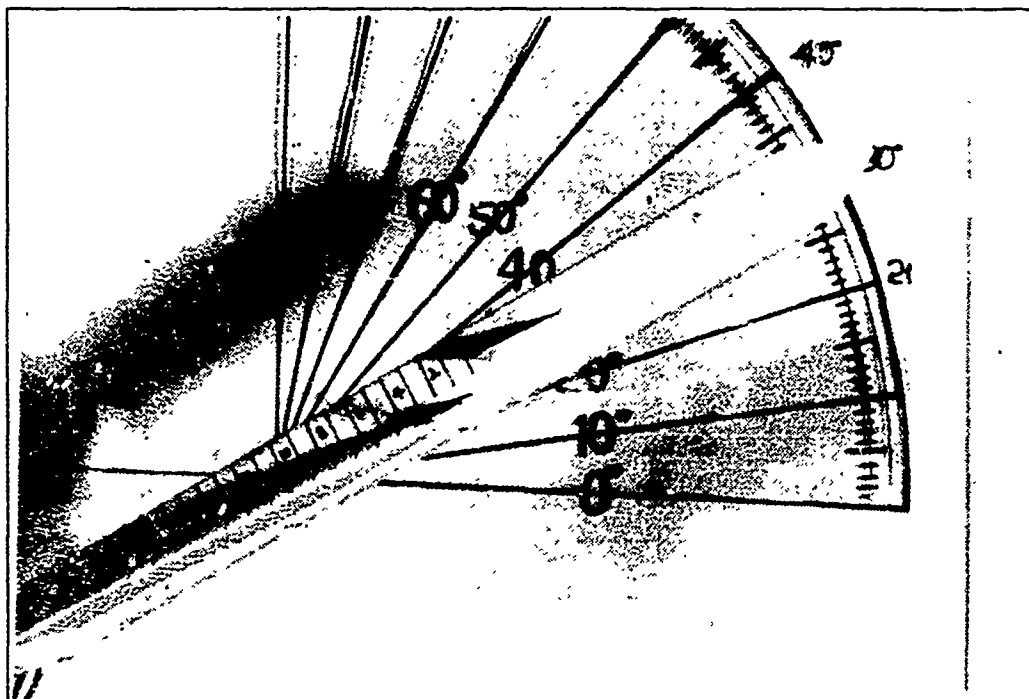
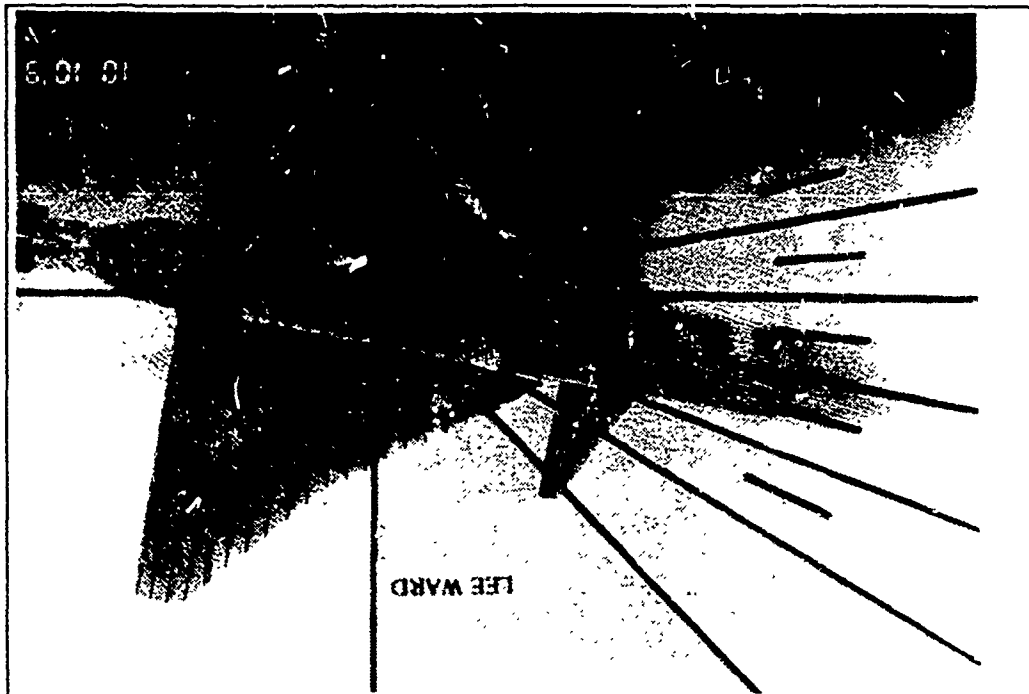


Figure 67. Wing Root Vortex Flow, Negative Sideslipping  
 ( $k=-0.05$ ),  $\alpha=30^\circ$ ,  $\beta=10^\circ$

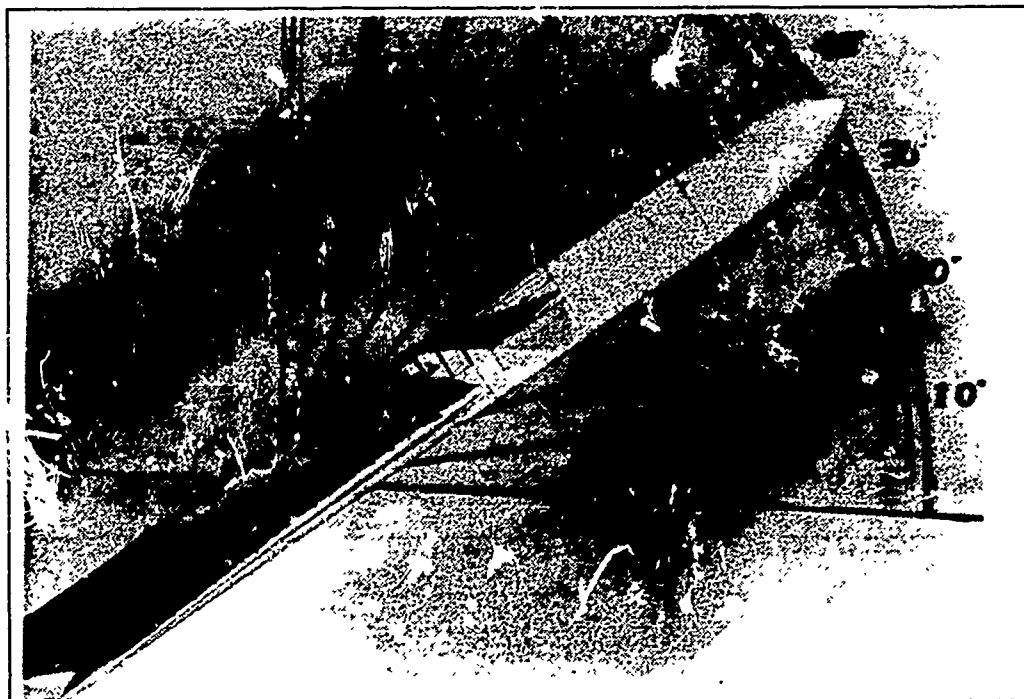
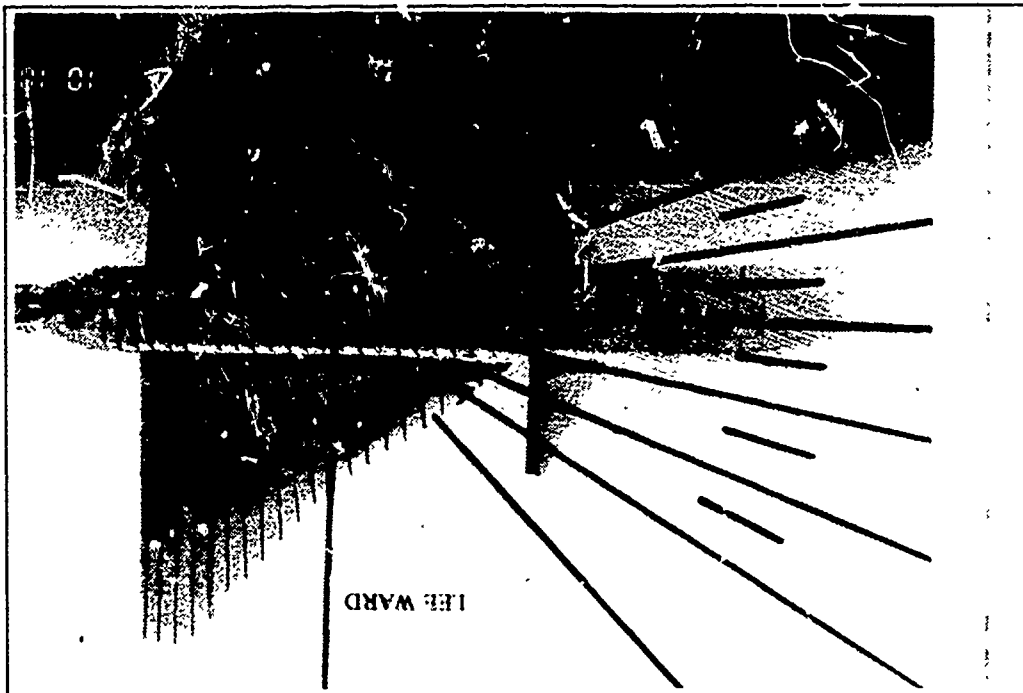


Figure 68. Wing Root Vortex Flow, Negative Sideslipping  
 ( $k=-0.05$ ),  $\alpha=35^\circ$ ,  $\beta=0^\circ$



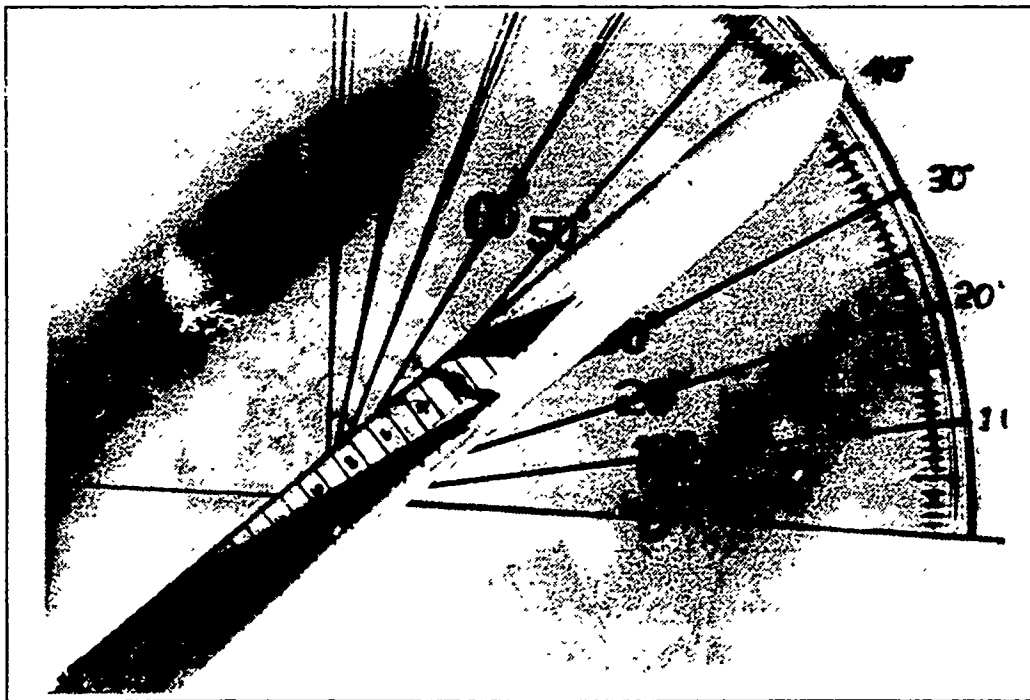
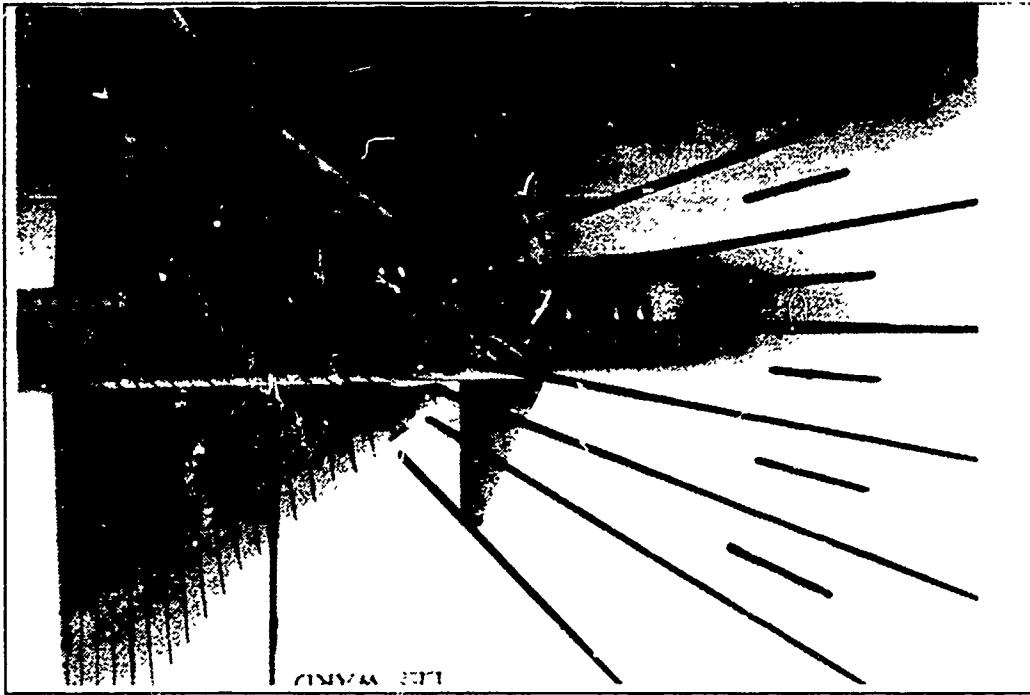


Figure 69. Wing Root Vortex Flow, Negative Sideslipping  
 $(k=-0.05)$ ,  $\alpha=40^\circ$ ,  $\beta=0^\circ$

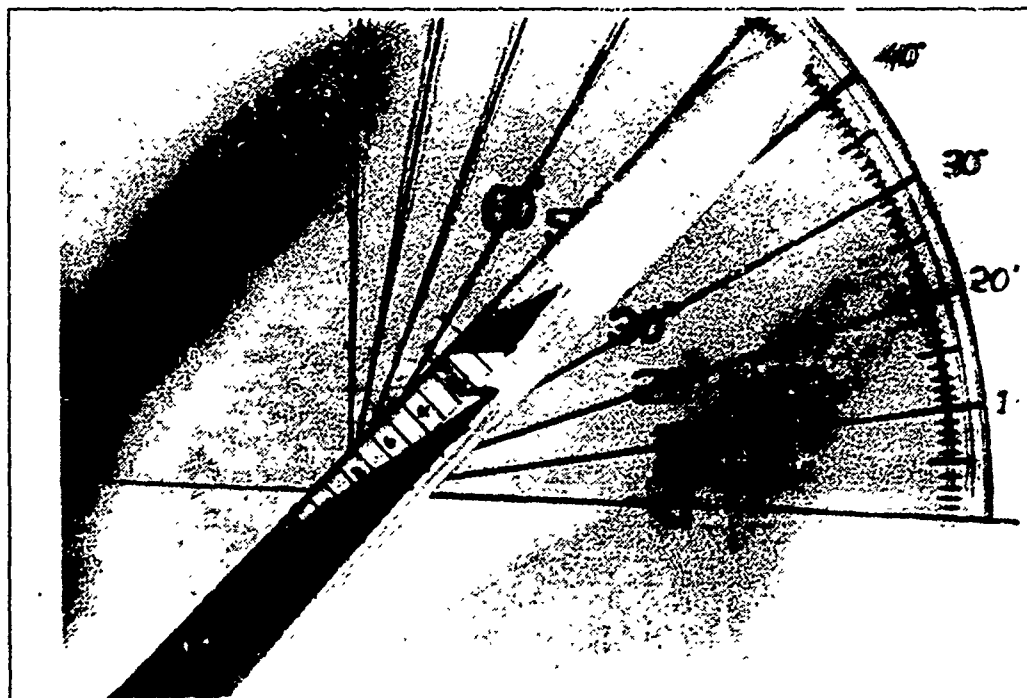
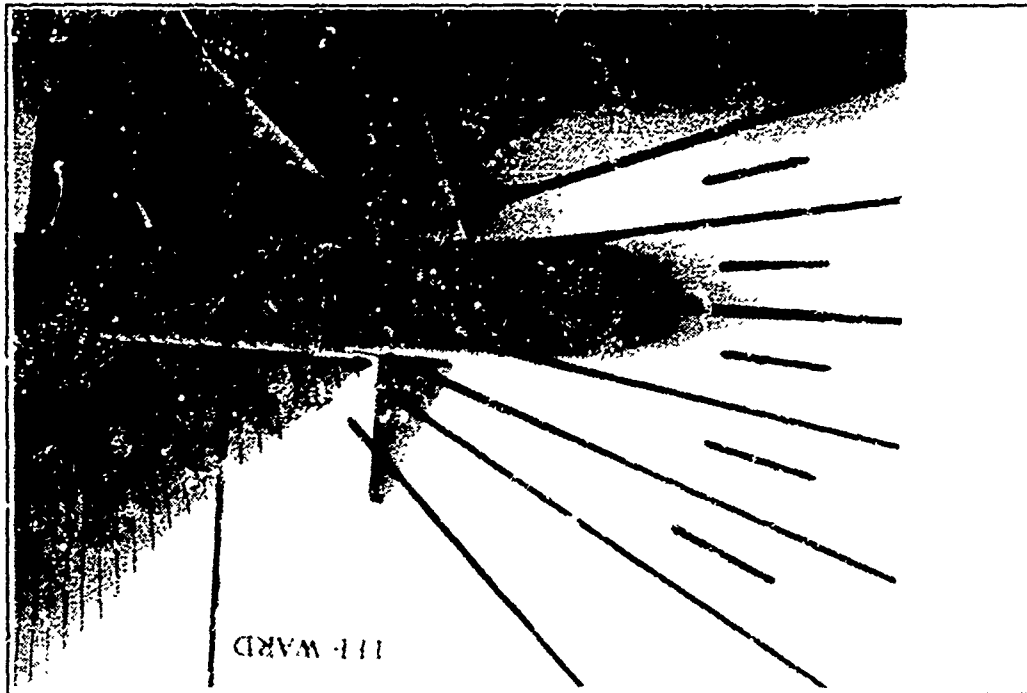


Figure 70. Wing Root Vortex Flow, Negative Sideslipping  
 ( $k=-0.05$ ),  $\alpha=45^\circ$ ,  $\beta=0^\circ$

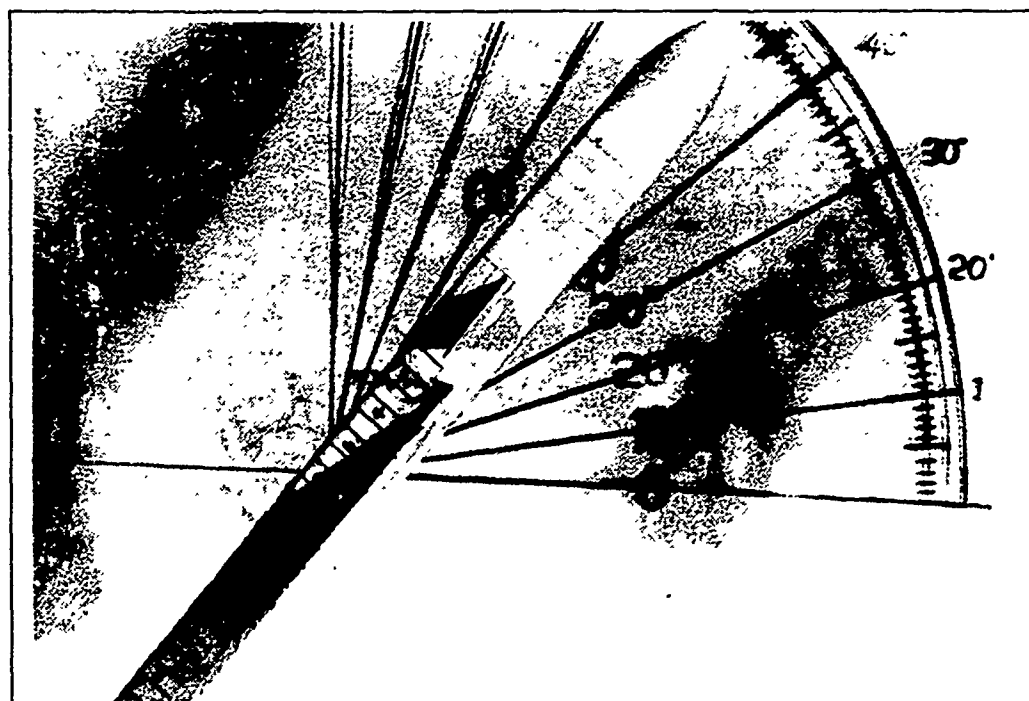
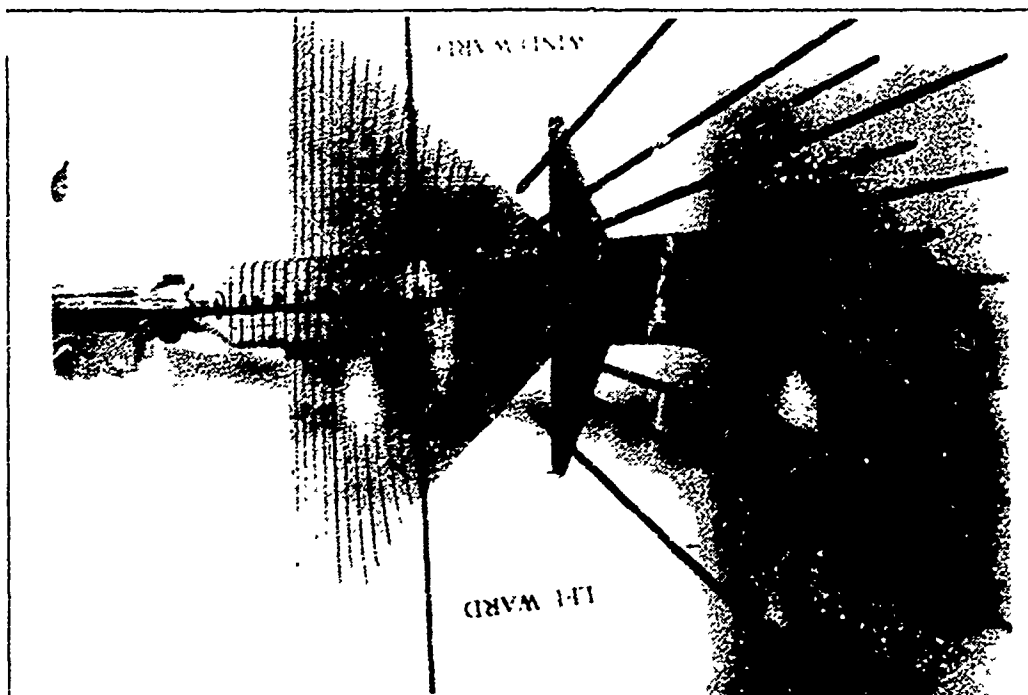
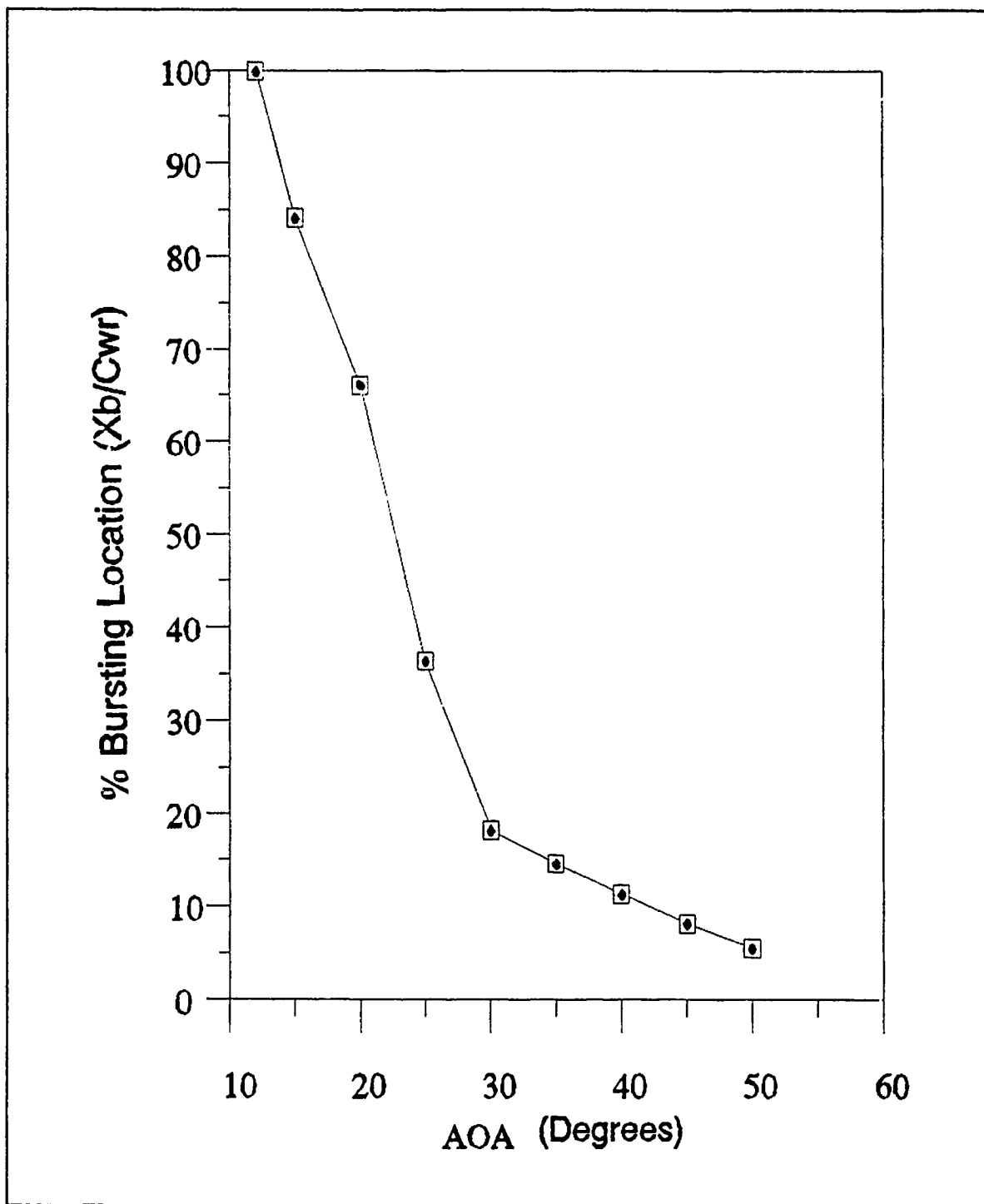


Figure 71. Wing Root Vortex Flow, Negative Sideslipping  
 ( $k=-0.05$ ),  $\alpha=50^\circ$ ,  $\beta=0^\circ$

## **APPENDIX B. EXPERIMENTAL RESULTS (GRAPHS)**

**FIGURES 72 THROUGH 78**



**Figure 72. Wing Root Vortex Burst Location as a Function of AOA for Static Case at Zero Sideslip Angle ( $\beta=0^\circ$ )**

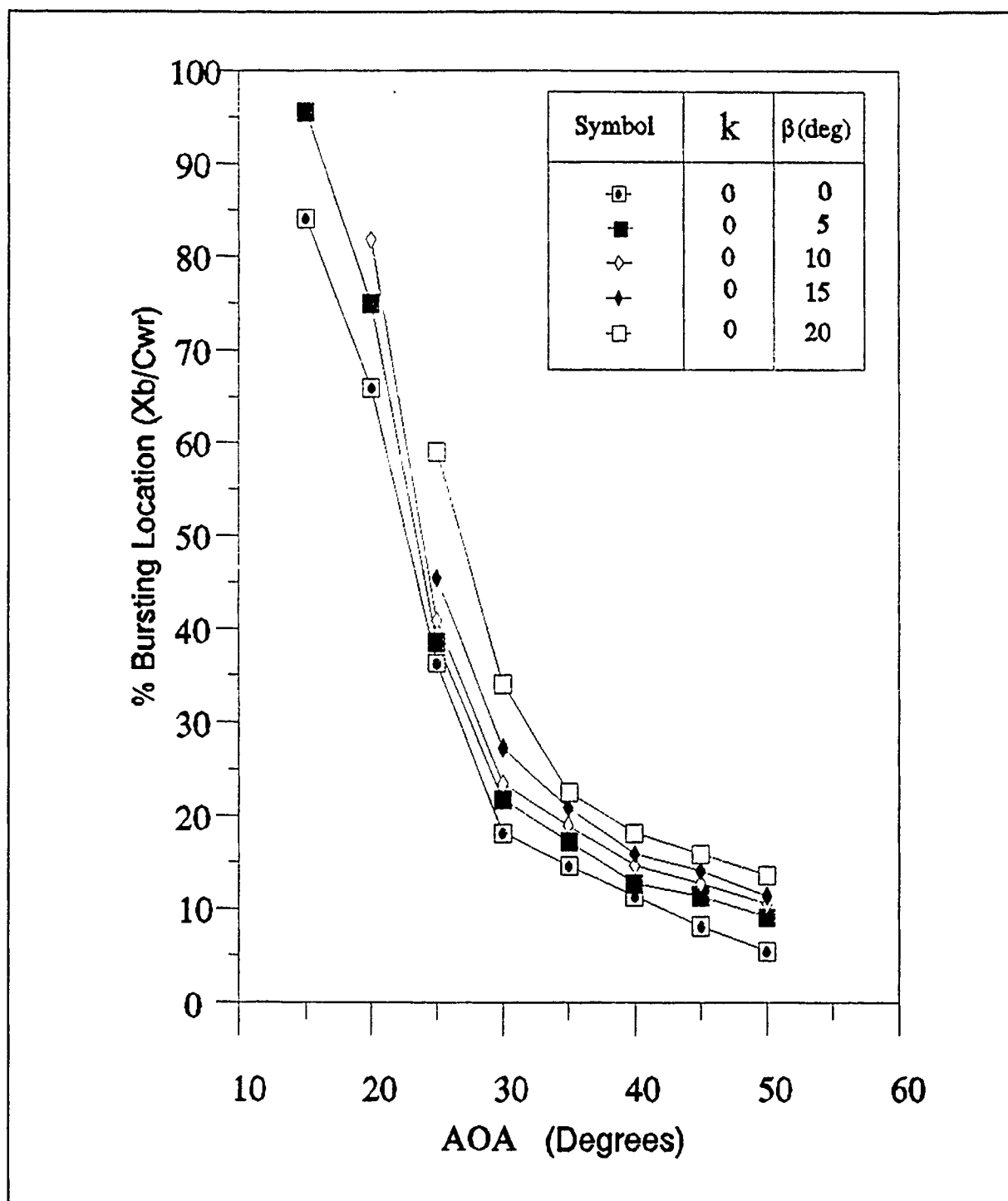


Figure 73. Wing Root Vortex Burst Location as a Function of AOA for Static Case at Different Sideslip Angles ( $\beta=0^\circ, 5^\circ, 10^\circ, 15^\circ, 20^\circ$ )

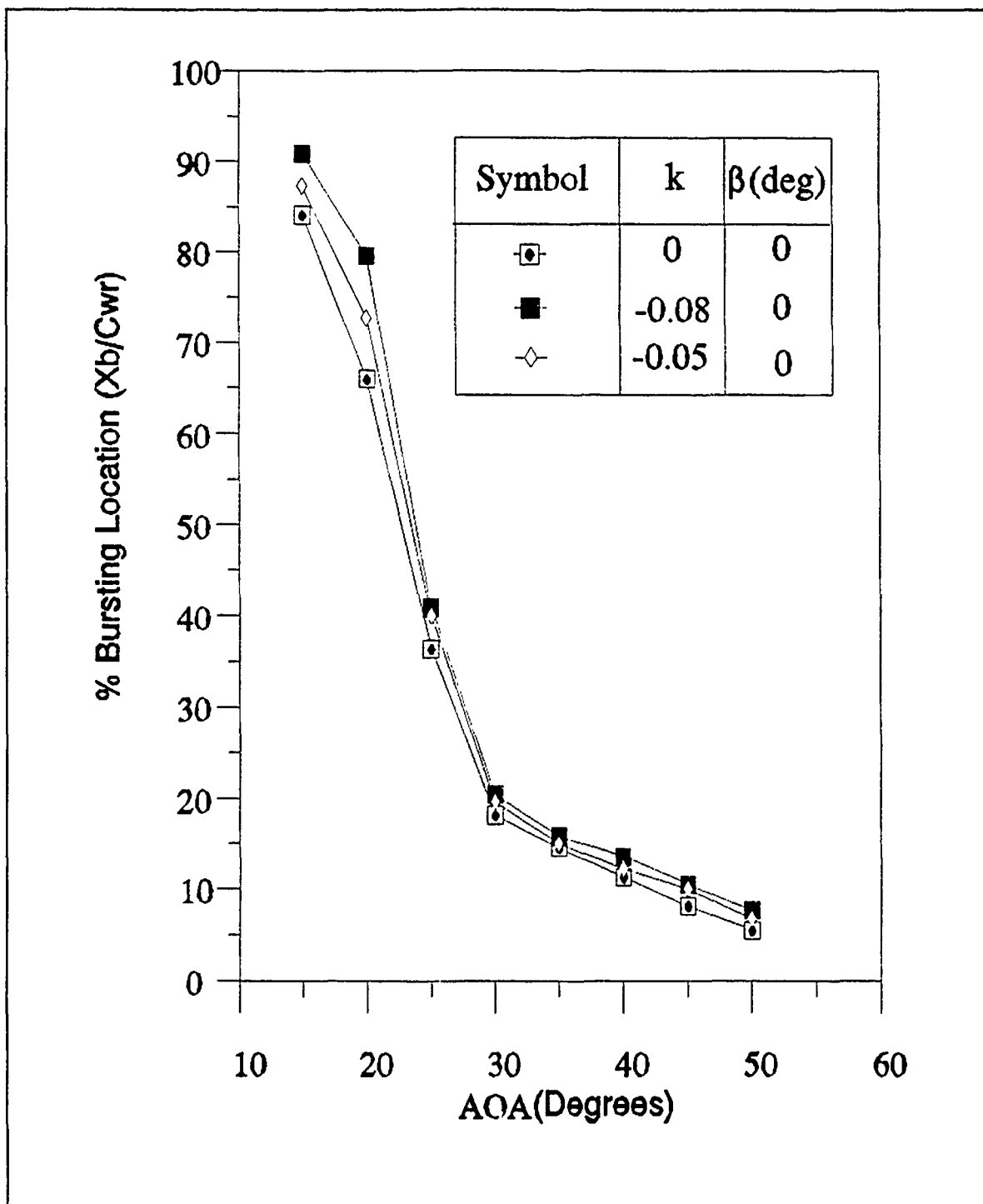


Figure 74. Wing Root Vortex Burst Location at  $0^\circ$  instantaneous Sideslip Angle During Sideslipping Motion, as a Function of AOA

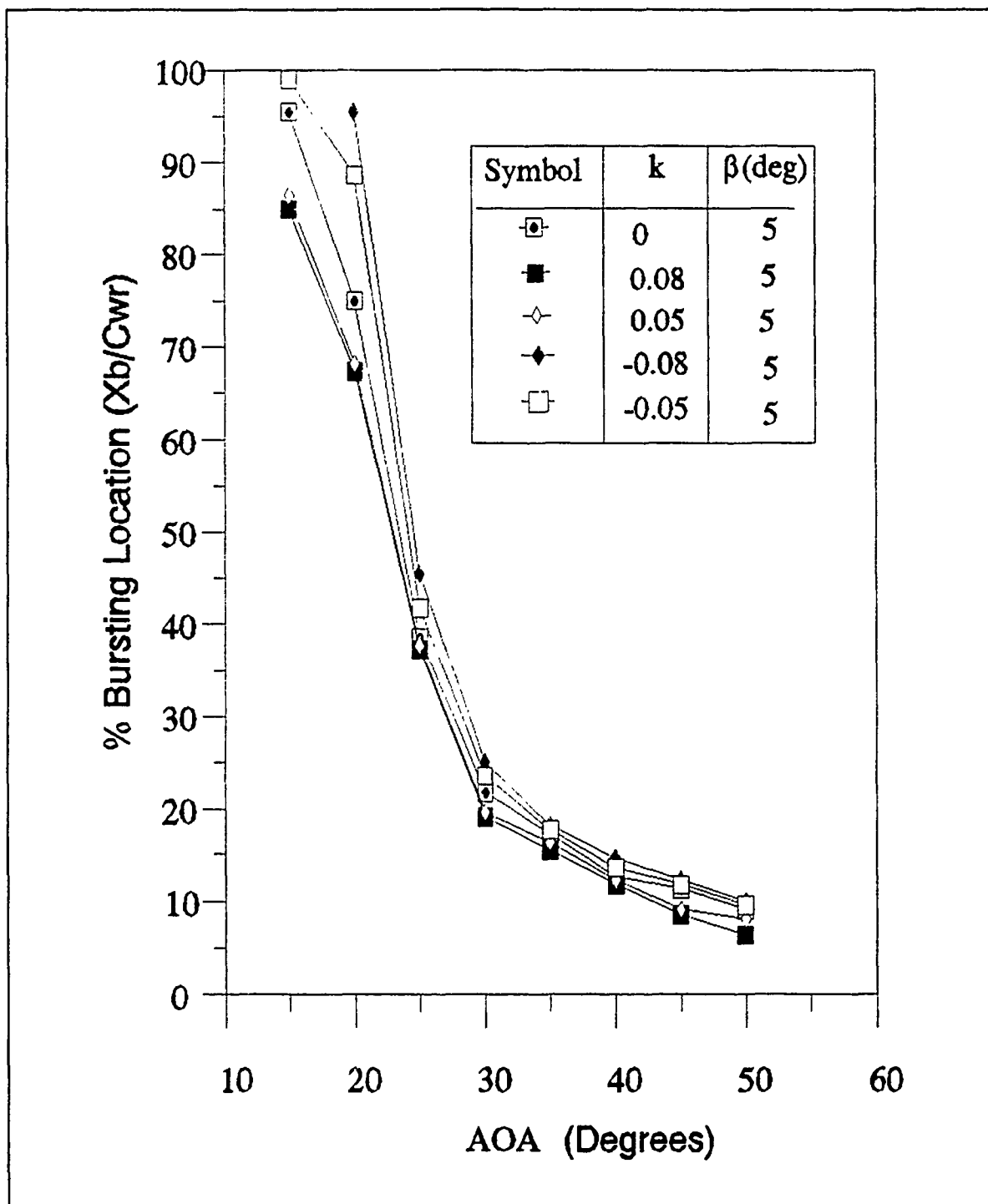
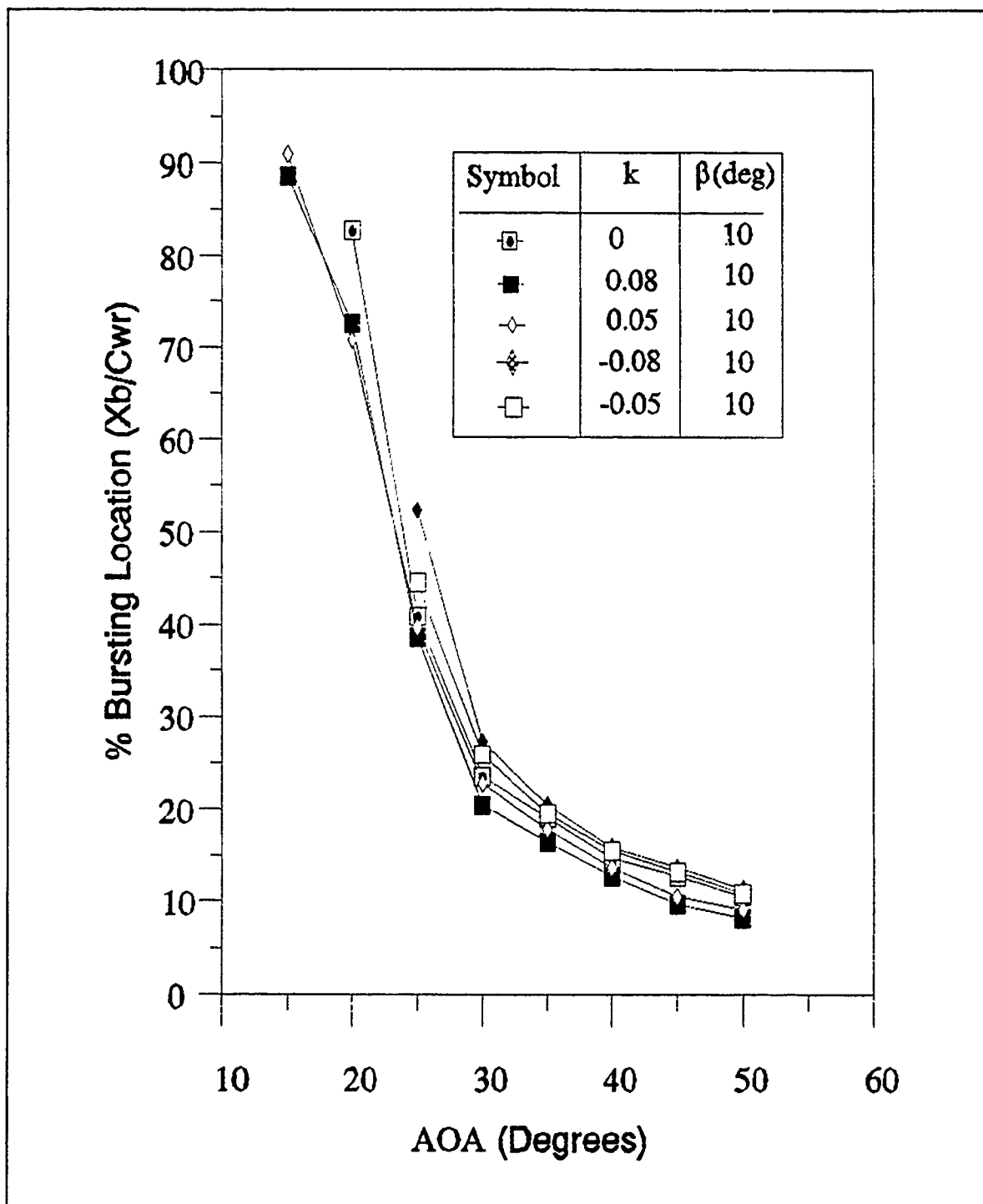


Figure 75. Wing Root Vortex Burst Location at 5° instantaneous Sideslip Angle During Sideslipping Motion, as a Function of AOA





**Figure 76. Wing Root Vortex Burst Location at  $10^\circ$  instantaneous Sideslip Angle During Sideslipping Motion, as a Function of AOA**

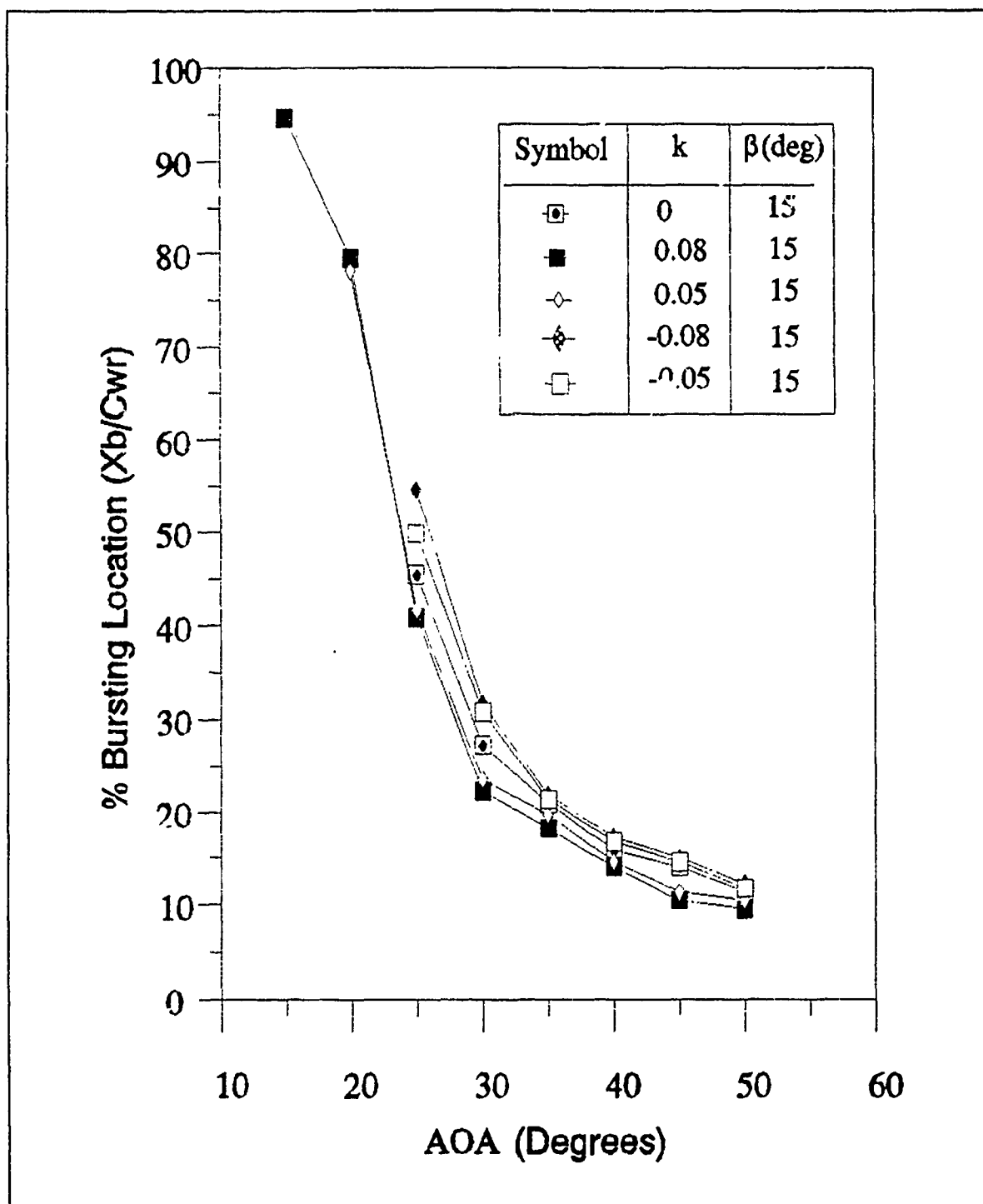
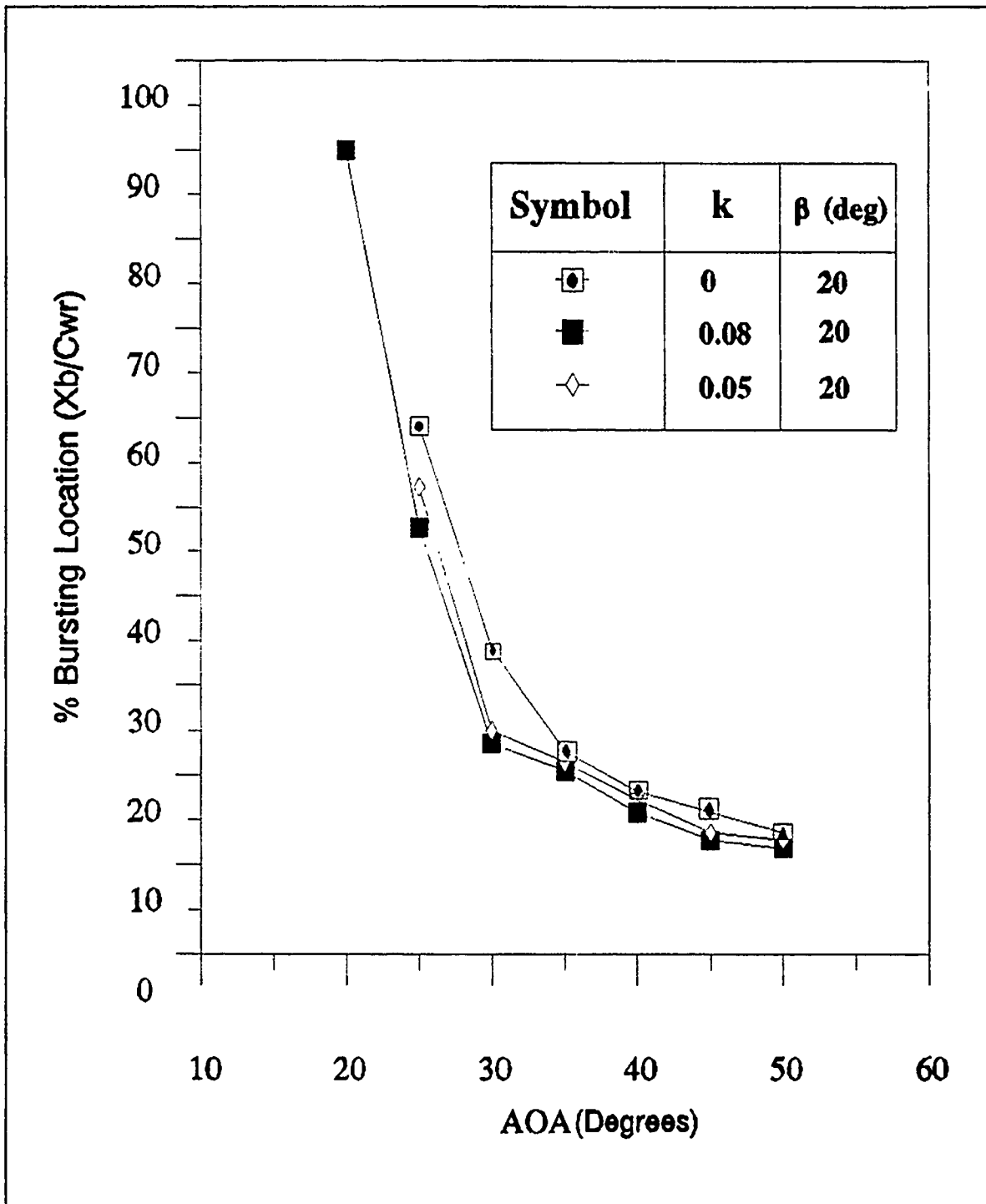


Figure 77. Wing Root Vortex Burst Location at 15° instantaneous Sideslip Angle During Sideslipping Motion, as a Function of AOA



**Figure 78. Wing Root Vortex Burst Location at 20° instantaneous Sideslip Angle During Sideslipping Motion, as a Function of AOA**

## APPENDIX C. EXPERIMENTAL RESULTS (TABLES)

TABLES 4 THROUGH 8

Table 4. % Non-Dimensional Vortex Core Length for Static Case ( $k=0$ )

$\alpha \backslash \beta$	0°	5°	10°	15°	20°
15°	84.1	21	N.W*	N.W	N.W
20°	66	75	81.8	N.W	N.W
25°	36.4	38.6	40.9	45.5	59.1
30°	18.2	21.8	23.6	27.3	34.1
35°	14.6	17.3	19.1	20.9	22.7
40°	11.4	12.7	14.6	15.9	18.2
45°	8.2	11.4	12.7	14.1	15.9
50°	5.5	9.1	10.5	11.4	13.6

N.W: No vortex bursting on the wing upper surface

Table 5. % Non-Dimensional Vortex Core Length for Positive Sideslipping Motion ( $k=0.08$ )

$\alpha \backslash \beta$	0°	5°	10°	15°	20°
15°	84.1	85	88.6	94.6	N.W
20°	66	67.3	72.7	79.6	90
25°	36.4	37.3	38.6	40.9	47.7
30°	18.2	19.1	20.5	22.3	23.6
35°	14.6	15.5	16.4	18.2	20.5
40°	11.4	11.8	12.7	14.1	15.9
45°	8.2	8.6	9.6	10.5	12.7
50°	5.5	6.4	8.2	9.6	11.8

N.W: No vortex bursting on the wing upper surface

Table 6. % Non-Dimensional Vortex Core Length for Positive Sideslipping Motion ( $k=0.05$ )

$\alpha \backslash \beta$	0°	5°	10°	15°	20°
15°	84.1	86.4	90.9	N.W	N.W
20°	14.5	68.2	72.7	78.2	N.W
25°	36.4	37.7	39.6	41.8	52.3
30°	18.2	19.6	21.8	23.6	25
35°	14.6	16.4	17.3	19.6	21.4
40°	11.4	12.3	13.6	14.6	17.3
45°	8.2	9.1	10.5	11.4	13.6
50°	5.5	8.2	9.1	10.5	12.7

N.W: No vortex bursting on the wing upper surface

Table 7. % Non-Dimensional Vortex Core Length for Negative Sideslipping Motion ( $k=-0.08$ )

$\alpha \backslash \beta$	0°	5°	10°	15°	20°
15°	90.9	N.W	N.W	N.W	N.W
20°	79.6	95.5	N.W	N.W	N.W
25°	40.9	45.5	52.3	54.6	59.1
30°	20.5	25	27.3	31.8	34.1
35°	15.9	18.2	20.5	21.8	22.7
40°	13.6	14.6	15.9	17.3	18.2
45°	10.5	12.3	13.6	15	15.7
50°	7.7	10	11.4	12.3	13.6

N.W: No vortex bursting on the wing upper surface

Table 8. % Non-Dimensional Vortex Core Length for Negative Sideslipping Motion ( $k=-0.05$ )

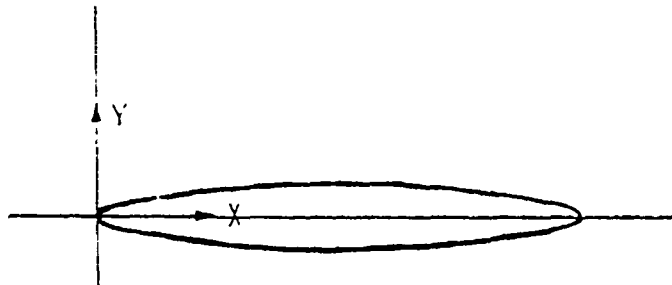
$\alpha \backslash \beta$	0°	5°	10°	15°	20°
15°	87.3	99	N.W	N.W	N.W
20°	72.7	88.6	N.W	N.W	N.W
25°	40	41.8	44.6	50	59.1
30°	19.6	23.6	25.9	30.9	34.1
35°	15	17.7	19.6	21.4	22.7
40°	12.3	13.6	15.5	16.8	18.2
45°	10	11.8	13.2	14.6	15.9
50°	6.8	9.6	10.9	11.8	13.6

N.W: No vortex bursting on the wing upper surface

## APPENDIX D. MISCELLANEOUS DATA



Table I. GEOMETRIC COORDINATES OF THE CANARD



ROOT SECTION		TIP SECTION	
X	Y	X	Y
0.000	$\pm 0.000$	0.000	$\pm 0.000$
0.012	$\pm 0.015$	0.023	$\pm 0.004$
0.100	$\pm 0.030$	0.025	$\pm 0.008$
0.200	$\pm 0.048$	0.050	$\pm 0.012$
0.300	$\pm 0.056$	0.075	$\pm 0.014$
0.400	$\pm 0.061$	0.100	$\pm 0.015$
0.500	$\pm 0.063$	0.125	$\pm 0.016$
0.600	$\pm 0.061$	0.150	$\pm 0.015$
0.700	$\pm 0.056$	0.175	$\pm 0.014$
0.800	$\pm 0.048$	0.200	$\pm 0.012$
0.900	$\pm 0.030$	0.225	$\pm 0.008$
0.988	$\pm 0.015$	0.247	$\pm 0.004$
1.000	$\pm 0.000$	0.250	$\pm 0.000$

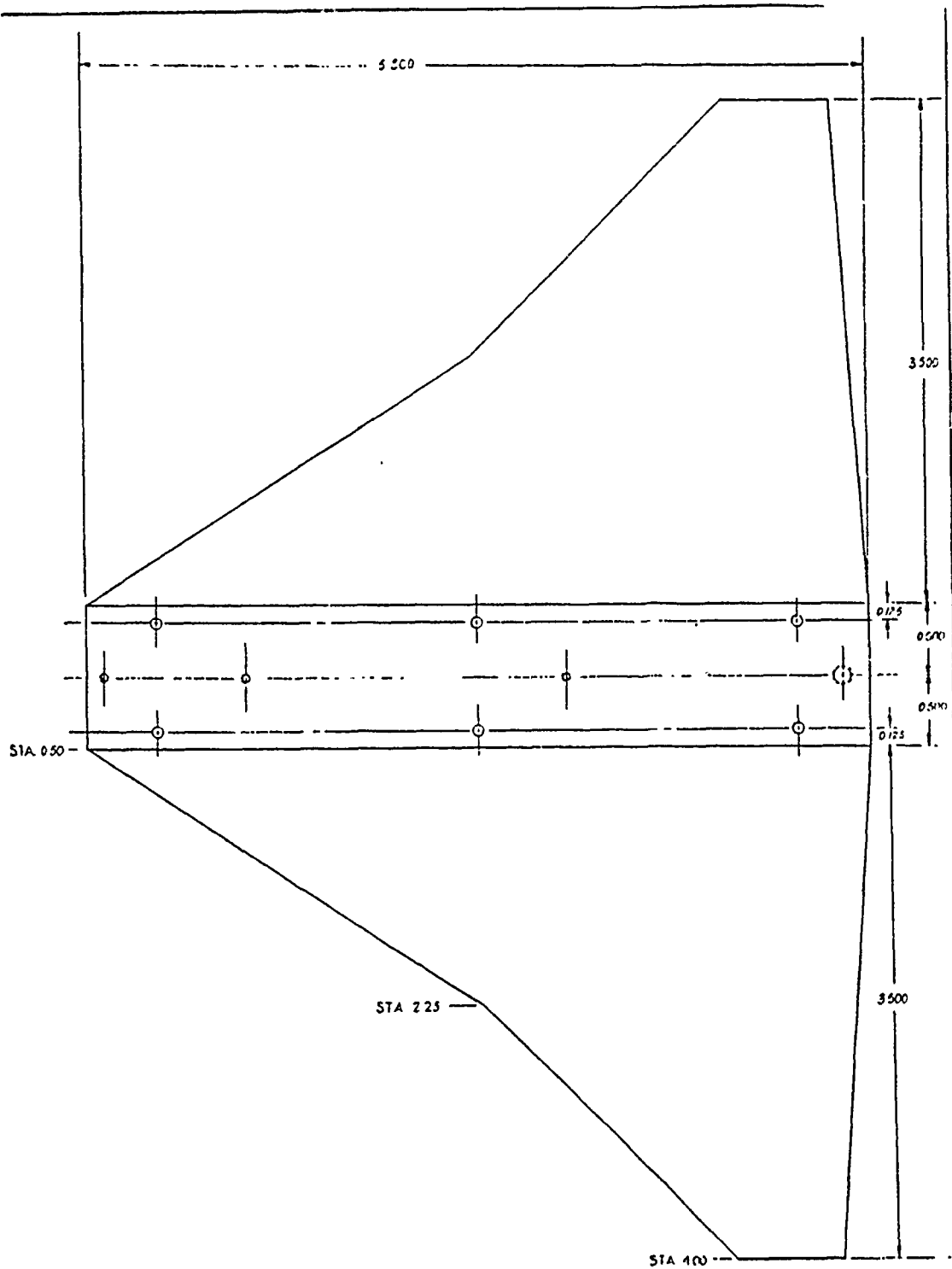
NOTE:

LEADING EDGE RADIUS AND  
TRAILING EDGE RADIUS ARE  
 $0.0156 \times \text{CHORD}$ .

Table I(continued). GEOMETRIC COORDINATES OF THE WING

AIRFOIL COORDINATES											
STATION 0.50				STATION 2.25				STATION 4.00			
X <sub>UPPER</sub>	Y <sub>UPPER</sub>	X <sub>LOWER</sub>	Y <sub>LOWER</sub>	X <sub>UPPER</sub>	Y <sub>UPPER</sub>	X <sub>LOWER</sub>	Y <sub>LOWER</sub>	X <sub>UPPER</sub>	Y <sub>UPPER</sub>	X <sub>LOWER</sub>	Y <sub>LOWER</sub>
0.0	0.0	0.0	0.0	0.0	0.0	0.0	0.0	0.0	0.0	0.0	0.0
0.025	0.028	0.020	-0.022	0.021	0.013	0.014	-0.011	0.023	0.004	0.004	-0.003
0.059	0.054	0.044	-0.027	0.019	0.016	0.021	-0.013	0.025	0.005	0.006	-0.004
0.066	0.044	0.071	-0.032	0.031	0.021	0.034	-0.015	0.009	0.006	0.010	-0.004
0.135	0.061	0.140	-0.040	0.064	0.029	0.067	-0.019	0.018	0.008	0.019	-0.005
0.272	0.086	0.278	-0.052	0.130	0.041	0.133	-0.025	0.037	0.012	0.038	-0.007
0.409	0.107	0.416	-0.060	0.195	0.051	0.198	-0.029	0.056	0.015	0.057	-0.008
0.547	0.125	0.553	-0.066	0.261	0.060	0.264	-0.032	0.075	0.017	0.075	-0.009
0.821	0.154	0.828	-0.079	0.392	0.073	0.395	-0.038	0.112	0.021	0.113	-0.011
1.097	0.176	1.105	-0.088	0.524	0.084	0.526	-0.042	0.150	0.024	0.150	-0.012
1.372	0.193	1.378	-0.095	0.655	0.092	0.657	-0.045	0.187	0.026	0.188	-0.013
1.648	0.206	1.652	-0.099	0.787	0.099	0.788	-0.048	0.225	0.028	0.225	-0.014
1.923	0.216	1.927	-0.103	0.918	0.103	0.920	-0.049	0.262	0.029	0.263	-0.014
2.199	0.222	2.201	-0.105	1.050	0.105	1.051	-0.050	0.300	0.030	0.300	-0.014
2.474	0.225	2.476	-0.105	1.181	0.107	1.182	-0.050	0.337	0.031	0.338	-0.014
2.750	0.225	2.750	-0.104	1.313	0.107	1.313	-0.049	0.375	0.031	0.375	-0.014
3.025	0.221	3.025	-0.101	1.444	0.106	1.444	-0.048	0.413	0.030	0.412	-0.014
3.301	0.214	3.299	-0.096	1.575	0.102	1.575	-0.046	0.450	0.029	0.450	-0.013
3.576	0.200	3.574	-0.087	1.707	0.096	1.706	-0.042	0.488	0.027	0.487	-0.012
3.852	0.181	3.848	-0.074	1.839	0.086	1.837	-0.035	0.525	0.025	0.525	-0.010
4.127	0.157	4.123	-0.058	1.970	0.075	1.968	-0.028	0.563	0.021	0.562	-0.008
4.402	0.129	4.398	-0.041	2.101	0.061	2.099	-0.020	0.600	0.018	0.600	-0.006
4.677	0.098	4.673	-0.024	2.232	0.047	2.230	-0.011	0.638	0.013	0.637	-0.003
4.957	0.065	4.949	-0.008	2.363	0.031	2.362	-0.004	0.675	0.009	0.675	-0.001
5.226	0.032	5.224	0.002	2.494	0.015	2.493	0.001	0.713	0.004	0.712	0.0

Table I(continued). PLANFORM DRAWING OF THE WING



## INITIAL DISTRIBUTION LIST

		No. Copies
1.	Defense Technical Information Center Cameron Station Alexandria, VA 22304-6145	2
2.	Library, Code 52 Naval Postgraduate School Monterey, CA 93943-5002	2
3.	Chairman, Code AA/Co Naval Postgraduate School Monterey, CA 93943-5000	1
4.	Professor S.K. Hebbar, Code AA/Hb Naval Postgraduate School Monterey, CA 93943-5000	2
5.	Professor M.F. Platzer, Code AA/Pl Naval Postgraduate School Monterey, CA 93943-5000	1
6.	Kim, Chang Ho Jai-Il Apt. 1/412 Sadang 4-Dong, Dongjag-Gu Seoul, Republic of Korea 156-094	2
7.	Ji, Yoon Gyu SMC 1508 Naval Postgraduate School Monterey, CA 93943	1
8.	Personal Management Office Air Force Headquarters Nonsan-Gun, Chungcheong Nam Do Republic of Korea	1
9.	Air Force Central Library Chongwon-Gun, Chungcheong Buk Do Republic of Korea	1
10.	Mr. Marvin Walters Naval Air Development Center Street Road Warminster, PA 18974-5000	1

11. Michael J. Harris  
Aircraft Division Code AIR-931  
Naval Air Systems Command  
Washington, D.C., 20361-9320

1